The Astrophysical Journal, 937:74 (48pp), 2022 October 1 https://doi.org/10.3847/1538-4357/ac61d9

The Physical Properties of Low-redshift FeLoBAL Quasars. I. Spectral-synthesis Analysis of the Broad Absorption-line (BAL) Outflows Using *SimBAL*

Hyunseop Choi (최현섭)[1], Karen M. Leighly[1], Donald M. Terndrup[1,2], Collin Dabbieri[3], Sarah C. Gallagher[4,5,6,7], and Gordon T. Richards[8]

[1] Homer L. Dodge Department of Physics and Astronomy, The University of Oklahoma, 440 W. Brooks Street, Norman, OK 73019, USA; hyunseop.choi@ou.edu
[2] Department of Astronomy, The Ohio State University, 140 W. 18th Avenue, Columbus, OH 43210, USA
[3] Department of Physics and Astronomy, Vanderbilt University, Nashville, TN 37235, USA
[4] Department of Physics & Astronomy, The University of Western Ontario, London, ON, N6A 3K7, Canada
[5] Canadian Space Agency, 6767 Route de l'Aéroport, Saint-Hubert, Quebec, J3Y BY9, Canada
[6] Institute for Earth and Space Exploration, The University of Western Ontario, London, ON, N6A 3K7, Canada
[7] The Rotman Institute of Philosophy, The University of Western Ontario, London, ON, N6A 3K7, Canada
[8] Department of Physics, Drexel University, 32 S. 32nd Street, Philadelphia, PA 19104, USA

Received 2021 December 30; revised 2022 March 8; accepted 2022 March 19; published 2022 September 29

Abstract

We present the first systematic study of 50 low-redshift ($0.66 < z < 1.63$) iron low-ionization broad absorption-line quasars (FeLoBALQs) using *SimBAL*, which represents a more than five-fold increase in the number of FeLoBALQs with detailed absorption line spectral analyses. We found the outflows have a wide range of ionization parameters, $-4 \lesssim \log U \lesssim 1.2$ and densities, $2.8 \lesssim \log n \lesssim 8$ [cm^{-3}]. The objects in our sample showed FeLoBAL gas located at a wide range of distances $0 \lesssim \log R \lesssim 4.4$ [pc], although we do not find any evidence for disk winds (with $R \ll 0.01$ pc) in our sample. The outflow strength primarily depends on the outflow velocity with faster outflows found in quasars that are luminous or that have flat or redder spectral energy distributions. We found that ~18% of the FeLoBALQs in the sample have the significantly powerful outflows needed for quasar feedback. Eight objects showed *overlapping troughs* in the spectra, and we identified eleven *loitering outflow* objects, a new class of FeLoBALQs that are characterized by low outflow velocities and high column density winds located $\log R \lesssim 1$ [pc] from the central engine. The FeLoBALs in loitering outflows objects do not show properties expected for radiatively driven winds, and these objects may represent a distinct population among FeLoBALQs. We discuss how the potential acceleration mechanisms and the origins of the FeLoBAL winds may differ for outflows at different locations in quasars.

Unified Astronomy Thesaurus concepts: Broad-absorption line quasar (183); Spectroscopy (1558); High-luminosity active galactic nuclei (2034); Active galactic nuclei (16); Galaxies (573); Quasars (1319)

Supporting material: figure set, machine-readable tables

1. Introduction

Iron low-ionization broad absorption-line quasars (FeLoBALQs) are arguably the most enigmatic of extragalactic objects. Their spectra present a tremendous range of phenomenology that has occasionally baffled experts.[9] Although rare and sometimes hard to find, their analysis may prove key to addressing several important questions involving galaxy evolution and quasar structure and demographics.

Broad absorption-line quasars (BALQs) are observed to comprise 10%–20% of optically selected quasars (Hewett & Foltz 2003; Reichard et al. 2003; Trump et al. 2006; Knigge et al. 2008; Gibson et al. 2009). BALQs are typically recognized by their C IV absorption, and accompanying transitions from ions with a single valence electron (Si IV, N V, O VI) as well as Lyα. If these are the only lines present, the object is known as a high-ionization BALQ (HiBALQ). A small fraction also have absorption from the lower-ionization ions, Mg II and Al III. These are known as low-ionization broad absorption-line quasars (LoBALQs). Even more rare are the FeLoBALQs that have absorption from Fe II and sometimes other iron-peak elements; observations of Mn II, Zn II, Ni II, Co II, and Cr II have been reported (e.g., de Kool et al. 2002a).

The precise fraction of quasars corresponding to the different types of BALQs is not well constrained, principally as a consequence of selection effects. Quasars can be identified by their typically blue colors; the classic example is the Palomar-Green survey (Green et al. 1986). While there exists relatively blue BAL quasars (Hewett & Foltz 2003), on average, BAL quasars are redder than unabsorbed quasars (e.g., Reichard et al. 2003; Gibson et al. 2009; Krawczyk et al. 2015). Thus while only ~15%–20% of optically selected quasars are BALQs, a larger fraction has been found among luminous quasars (Maiolino et al. 2004; Dai et al. 2008, 2012; Bruni et al. 2019) and red, infrared-selected, and radio-selected objects (Dai et al. 2008; Urrutia et al. 2009; Fynbo et al. 2013; Krogager et al. 2015, 2016; Morabito et al. 2019). Observations suggest that a larger fraction of LoBALQs and FeLoBALQs are missed in optical quasar surveys (Urrutia et al. 2009; Dai et al. 2012; Morabito et al. 2019). Part of the problem is that in addition to the heavily absorbed and reddened spectrum, they can lack strong emission lines, and their spectra can be confused with those of M-type stars and vice versa (e.g.,

---

[9] https://www.nytimes.com/1999/08/17/us/rarely-bested-astronomers-are-stumped-by-a-tiny-light.html?smid=url-share

SDSS J092853.51+570735.3; West et al. 2011; Pâris et al. 2018).

Traditionally, there are two explanations for these BAL classes. An equatorial accretion-disk wind may be present in every quasar, and the BAL type observed depends on the angle of the line of sight with respect to the accretion disk (e.g., Krolik & Voit 1998). Supporting this view is the fact that X-ray spectra from a sample of HiBAL quasars are absorbed but otherwise indistinguishable from normal quasars (e.g., Gallagher et al. 2002, 2006); they also have similar broadband spectral energy distributions (SEDs; Gallagher et al. 2007a). Alternatively, BALQs may represent a blow-out phase in the evolution of galaxies, occurring when a heavily shrouded ultraluminous, infrared galaxy-type (ULIRG) object shrugs off its cloak of dust and gas (e.g., Farrah et al. 2012). The fact that LoBALQs and FeLoBALQs are more common among optically red quasars supports this scenario (e.g., Urrutia et al. 2009). Red quasars are themselves very interesting objects. There is evidence that red quasars evolve differently than blue quasars (e.g., Glikman et al. 2018; Klindt et al. 2019), a result that suggests that dust-reddened quasars may be an intermediate phase between a merger-driven starburst in a completely obscured AGN, and a normal, unreddened quasar (e.g., Glikman 2017). These two origin stories are not mutually exclusive. In fact, it is plausible that the combination of both explanations may describe BALQ population.

Depending on the physical conditions, the Fe^{+} ion can contribute thousands of absorption lines to the near-UV spectrum. The wide range of critical densities and oscillator strengths probed by Fe II makes these features richly diagnostic of the physical state of the absorbing gas (e.g., Lucy et al. 2014). Specifically, the relative strength of the suite of lines shows a strong dependence on the density, ionization parameter, and column density within the outflow. What this means is that the physical conditions of the outflows in FeLoBALQs can be measured with a precision that is arguably unequaled among outflow phenomena in quasars.

However, a detailed understanding of FeLoBAL quasars and their origin has been hampered by the complexity of the spectra. The combination of the thousands of absorption lines and velocity dispersion in the outflows (i.e., the lines are broad) results in significant blending. Traditional methods of analysis that involve identification and measurement of individual lines are difficult to use on these complicated spectra. As a result, detailed analysis has been performed on only a handful of objects. Wampler et al. (1995) presented an qualitative analysis of a high-resolution spectrum of the FeLoBAL quasar Q0059−2735 that was discovered as part of the Large Bright Quasar Survey (Morris et al. 1991). The first FeLoBAL quasars subjected to detailed photoionization analyses were QSO 2359−1241 (Arav et al. 2001, 2008; Korista et al. 2008; Bautista et al. 2010) and three objects discovered in the Far-Infrared and Submillimetre Telescope (FIRST) survey (White et al. 2000): FIRST J104459.6+365605 (de Kool et al. 2001; Everett et al. 2002), FBQS 0840+3633 (de Kool et al. 2002a), FIRST J121442.3+280329 (de Kool et al. 2002b). These masterful and difficult analyses yielded the first well-constrained distances to the outflows (from 1 to 700 pc). The Sloan Digital Sky Survey (SDSS; Blanton et al. 2017) yielded many more FeLoBALQs (e.g., Hall et al. 2002), including some very unusual and interesting objects. Hall et al. (2003) discussed formation scenarios for the narrow Ca II observed in the overlapping-trough object SDSS J030000.56+004828.0. Other FeLoBALQs that have been analyzed in varying degree of detail include SDSS J0838+2955 (Moe et al. 2009), SDSS J0318−0600 (Dunn et al. 2010; Bautista et al. 2010), AKARI J1757+5907 (Aoki et al. 2011), SDSS J112526.12+002901.3 (Shi et al. 2016), and PG 1411+442 (Hamann et al. 2019b).

The analysis of complex spectra of BALQs has become possible with the introduction of the novel spectral-synthesis modeling software *SimBAL* (Leighly et al. 2018). Because *SimBAL* uses forward modeling, line blending can be accounted for. In addition, because *SimBAL* models the whole spectrum, it uses the information conveyed by the lines that are *not* present in the observed spectrum. The analysis of the $z = 2.26$ quasar SDSS J135246.37+423923.5 and the discovery of a remarkably powerful outflow in that object (Choi et al. 2020) demonstrated an effective application of the *SimBAL* methodology on an overlapping-trough FeLoBALQ.

This paper is the first in a series of four papers. In Paper II, Leighly et al. (2022), we discuss the rest-optical spectral properties of a subsample of $z < 1$ FeLoBALQs. Paper III, Choi et al. (2022), combines the FeLoBAL properties discussed in this paper and the emission-line analysis results from Paper II, Leighly et al. (2022). Finally, in Paper IV (K. M. Leighly et al. 2022, in preparation), we discuss broadband optical/IR properties of FeLoBALQs and the potential implication for the evolution scenarios for low-redshift FeLoBAL quasars.

In this paper, we present the analysis of the outflows in 50 low-redshift ($0.66 < z < 1.63$) FeLoBAL quasars. This work increases the number of FeLoBALQs with detailed analyses by a factor of five. In addition, the uniform analysis means that the properties of the objects can be easily compared. These objects were drawn from two samples (Section 2). The first sample includes low-redshift FeLoBALQs that were observed by Spitzer in order to constrain their far-infrared SEDs (Farrah et al. 2012). The second sample includes 30 objects with sufficiently low redshift and high-quality spectra so that the Hβ/[O III] region of the spectrum could be analyzed; the results are reported in the companion paper, Leighly et al. (2022). Section 3 gives a brief recap of the *SimBAL* software, and a description of our method for modeling the continuum using principal component analysis (PCA) eigenvectors extracted from SDSS spectra of unabsorbed quasars (also Appendix A). Section 4 details how we quantified the various physical and kinematic properties of the outflows using the results from the *SimBAL* model-fitting. Section 5 presents the *SimBAL* model-fitting results and discusses the distributions of the parameters measured directly by the model fitting including the ionization parameter, density, column density, velocity, and parameters extracted from the models including the location of the outflow and its kinetic luminosity. Section 6 describes the relationships among parameters, properties of the opacity profiles, and several special groups of objects. Section 7 discusses the implications of this large study for our understanding of the origins, formation, and acceleration of broad absorption-line outflows. Section 8 summarizes the results and presents planned future work.

2. Sample Selection and Data

Our total sample of 53, $0.66 < z < 1.63$ FeLoBALQs was chosen from two sources. The data and other parameters are listed in Table 1. We report the SDSS names of the objects in

Table 1
The Sample

SDSS Object Name	Sample[a]	Spectra[b]	m_i[c]	SDSS DR14Q Redshift	Redshift Used	Redshift Origin[d]
011117.36+142653.6	F	5131-55835-0054	17.73	1.154	1.1551 ± 0.0002	[O II]
015813.56–004635.5	O	7837-56987-0485	20.44	0.896	0.8959 ± 0.0002	narrow Hβ
024254.66–072205.6	F	0456-51910-0378	18.71	1.2166	1.2175 ± 0.0002	[O II]
025858.17–002827.0	O	4242-55476-0028 9372-58074-0974	19.00	0.875	$0.8758^{+0.0009}_{-0.0005}$	[O II]
030000.57+004828.0	F	0410-51877-0623	16.61	0.900	0.8907 ± 0.0002	[O II]
033810.84+005617.6[e]	F	0714-52201-0326	18.35	1.6295	1.6316 ± 0.0006	Hewett & Wild (2010)
080248.18+551328.8	O	7281-57007-0616	17.90	0.663	$0.6636^{+0.0001}_{-0.00008}$	[O II]
080957.39+181804.4	O	4493-55585-0632	17.44	0.970	0.970	SDSS DR14Q
081312.61+432640.1	F	0547-51959-0242 0546-52205-0449 0547-52207-0274	18.80	1.0865	1.0894 ± 0.0008	[O II]
083522.77+424258.3	F, O	8280-57061-0366	17.42	0.806	0.8066 ± 0.0002	[O II]
084044.41+363327.8	F	8858-57450-0056	16.25	1.235	1.2372 ± 0.0001	FeII
091658.43+453441.1	O	7517-56772-0266	19.81	0.915	0.9141 ± 0.0002	narrow Hβ
091854.48+583339.6	F	0484-51907-0598	19.19	1.315	1.3110 ± 0.0004	[NeV]
094404.25+500050.3	O	7292-56709-0400	19.31	0.965	0.9656 ± 0.0003	[O II]
100605.66+051349.0	F	0996-52641-0243	18.67	0.9704	0.9683 ± 0.0002	[O II]
101927.37+022521.4	F	0503-51999-0464	18.61	1.3643	1.3648 ± 0.0002	[O II]
102036.10+602339.0	F	7087-56637-0979	18.28	1.015	1.0145 ± 0.0004	[O II]
102226.70+354234.8	O	4564-55570-0360	19.46	0.818	0.8207 ± 0.0003	[O II]
102358.97+015255.8	F	0504-52316-0268	19.12	1.0761	1.07537 ± 0.00009	[O II]
103036.92+312028.8	O	6451-56358-0440 10465-58144-0458 11383-58485-0722	17.65	0.864	0.8605 ± 0.0002	[O II]
103903.03+395445.8	O	4633-55620-0278	19.66	0.864	0.8637 ± 0.0002	[O II]
104459.60+365605.1	O	8851-57460-0737	16.65	0.703	0.703	SDSS DR14Q
105748.63+610910.8[e]	F	0774-52286-0278	19.49	1.2757	1.2743 ± 0.0006	Hewett & Wild (2010)
112526.12+002901.3	F, O	3839-55575-0812	17.90	0.864	$0.8636^{+0.0003}_{-0.0002}$	[O II]
112828.31+011337.9	F, O	4730-55630-0172	18.38	0.893	0.8930 ± 0.0002	narrow Hβ
112901.71+050617.0	F	0837-52642-0400	19.42	1.2775	1.2814 ± 0.0008	Hewett & Wild (2010)
114556.25+110018.4	F	1226-52734-0375	18.81	0.9330	0.9350 ± 0.0006	[NeV]
115436.60+030006.3	F	4765-55674-0082	17.70		1.46968 ± 0.00007	FeII
115852.86–004301.9	F	0285-51930-0189	19.38	0.9833	0.9835 ± 0.0002	[O II]
120049.54+632211.8	F, O	7106-56663-0915	18.86	0.887	0.8862 ± 0.0001	narrow Hβ
120627.62+002335.4	F	0286-51999-0499	18.68	1.114	1.1369 ± 0.0008	Hewett & Wild (2010)
120815.03+624046.4	O	6974-56442-0404	19.72	0.799	$0.7982^{+0.00004}_{-0.00003}$	narrow Hβ
121231.47+251429.1	O	5975-56334-0556	19.32	0.842	0.8427 ± 0.0004	[O II]
121441.42–000137.8	F	0287-52023-0514	18.81	1.046	$1.04571^{+0.0002}_{-0.0001}$	[O II]
121442.30+280329.1	O	6476-56358-0374 2229-53823-0557	17.16	0.695	0.6945 ± 0.0002	[O II]
123549.95+013252.6	F	0520-52288-0001	19.16	1.2918	1.2902 ± 0.0002	[O II]
124014.04+444353.4	O	6617-56365-0631	20.10	0.964	$0.9634^{+0.0001}_{-0.0002}$	narrow Hβ
132117.24+561724.5	O	6828-56430-0710	19.53	0.794	0.7941 ± 0.0001	[O II]
132401.53+032020.5	F, O	4761-55633-0136	18.97	0.927	0.9254 ± 0.0001	[O II]
133632.45+083059.9	O	1801-54156-0530	18.23	0.805	0.7988 ± 0.0003	Fe II, broad Hβ
135525.24+575312.7	O	8199-57428-0180	20.59	0.855	0.8552 ± 0.0001	[O II]
135640.34+452727.2	O	6629-56365-0728	19.52	0.802	0.8025 ± 0.00009	[O II]
142703.62+270940.4	F	6018-56067-0412	18.13	1.165	1.1669 ± 0.0001	[O II]
144800.15+404311.7	O	5172-56071-0836 8498-57105-0724	16.80	0.805	0.805	SDSS DR14Q
151708.94+232857.5	O	3961-55654-0256	20.30	0.810	0.8093 ± 0.0001	[O II]
152737.17+591210.1	O	6799-56478-0458	18.33	0.930	0.930	SDSS DR14Q
153145.01+485257.2	O	6728-56426-0078	19.60	0.945	0.9445 ± 0.0002	[O II]
155633.77+351757.3	F	4965-55721-0548	18.04		1.501	Schulze et al. (2017)
164419.75+530750.4	O	8057-57190-0707	17.90	0.781	0.7813 ± 0.0002	[O II]
173753.97+553604.9[e]	F	0358-51818-0056	19.86	1.1017	1.1109 ± 0.0007	[NeV]
210712.77+005439.4	F	0985-52431-0522	20.42	0.9244	0.9266 ± 0.0002	[O II]
213537.44–032054.8	O	4385-55752-0286	18.59	0.815	$0.8127^{+0.0002}_{-0.0001}$	[O II]
230730.69+111908.5	O	6154-56237-0120	19.51	0.878	0.8770 ± 0.00009	narrow [O II]

Notes.

[a] F: objects drawn from Farrah et al. (2012); O: objects included in Leighly et al. (2022).

[b] Multiple spectra are listed when combined to increase signal-to-noise ratio in the optical band. The first spectrum listed set the wavelength sampling and flux level, and subsequent spectra were resampled and scaled to match.

[c] The magnitudes are taken from the point-source function magnitudes in the AB system from the SDSS DR16, uncorrected for Galactic extinction.

[d] The origin of the redshift in column 5. An emission line signals measurement directly from the spectrum.

[e] Objects excluded from the analysis (Section 3.3.1).

(This table is available in machine-readable form.)

column 1, and throughout the paper we use the shortened four by four naming scheme (e.g., SDSS JHHMM+DDMM). Part of the sample was drawn from the 31 objects presented in Farrah et al. (2012), and we analyzed data from 28 of these. For this paper, we rejected objects that did not have sufficient signal-to-noise ratio spectra, clear detection of Fe II absorption features, and any evidence of strong resonance-scattering emission from the BAL wind. Specifically, we excluded three objects from the sample analyzed in Farrah et al. (2012). SDSS J0911+4446 was excluded due to a low signal-to-noise spectrum, which shows unusually strong Fe II emission features potentially coming from resonance scattering from the BAL outflows (e.g., Wang et al. 2016). The spectrum for SDSS J2215−0045 showed BAL features only from Fe III instead of Fe II. Finally, SDSS J2336−0107 was shown to be a double quasar by Foreman et al. (2009), and we could not obtain an adequate spectrum from the SDSS archive for the *SimBAL* analysis.

Additionally we included 25 FeLoBALQs from Leighly et al. (2022). All of these objects have $z < 1$ and sufficiently good signal-to-noise ratios so that the Hβ/[O III] region of the spectrum could be analyzed. The *SimBAL* analysis of the FeLoBALs in the objects included in Leighly et al. (2022) are discussed in this paper; however, we refer to that publication for analysis of the Hβ/[O III] region and the discussion of the relationships between the FeLoBAL properties and the quasar optical emission-line properties. Column 2 of Table 1 gives the sample origin of the objects.

In some cases, the object was observed by SDSS and then by Baryon Oscillation Spectroscopic Survey (BOSS; Dawson et al. 2013, 2016). The highest-signal-to-noise-ratio spectrum available from the SDSS (Blanton et al. 2017) archive was chosen for analysis. Multiple spectra are listed when they were averaged for rest-frame optical band analysis when no spectral variability was observed (Leighly et al. 2022). The *i*-band SDSS magnitudes are listed in Table 1 (column 4).

As an accurate redshift is essential to analyzing the outflow properties, we remeasured the SDSS catalog redshifts where possible. In order of preference and as available, redshifts were measured using (1) the low-ionization narrow emission-lines of [O II] or narrow Hβ, (2) the narrow high-ionization [Ne V] line, or (3) the Fe II pseudo-continuum template. Failing those methods, the Hewett & Wild (2010) catalog redshifts were used. Best-fitting redshifts and the emission line used for their measurements are listed in Table 1 (columns 6 and 7).

3. Spectral Modeling with *SimBAL*

3.1. *The Spectral-synthesis Software* SimBAL

The traditional method for analyzing BALQ spectra involves line identification of individual BALs and measurement of the ionic column densities for each identified line in order to constrain the physical properties of the absorbing gas (e.g., Bautista et al. 2010; Dunn et al. 2010; Arav et al. 2013; Lucy et al. 2014). This process becomes extremely challenging and ambiguous when the lines are broad, and severe line blending causes the BALs to overlap and create wide troughs in the spectrum. Some FeLoBALQs show thousands of line transitions from Fe II. The spectral-synthesis code *SimBAL* was introduced by Leighly et al. (2018) and further developed by Leighly et al. (2019) and Choi et al. (2020). We describe the basic properties here but refer to those publications for details.

SimBAL uses a forward-modeling technique that allows for the analysis of heavily absorbed and blended BALQ spectra. Six physical parameters are required to create an individual synthetic BAL. The parameters are as follows: the dimensionless ionization parameter $\log U$, the gas density $\log n$ [cm^{-3}], a column density parameter $\log N_H - \log U$ [cm^{-2}] that represents the thickness of the gas column with respect to the hydrogen ionization front, the velocity offset $v_{\rm off}$ (km s^{-1}), the width of the absorption lines $v_{\rm width}$ (km s^{-1}), and a dimensionless-covering-fraction parameter $\log a$ where larger $\log a$ represents lower partial-covering of the emission source. *SimBAL* uses the Markov Chain Monte Carlo (MCMC) method, `emcee`[10] (Foreman-Mackey et al. 2013), to compare the synthetic spectrum with the observed spectrum. From the converged chain of parameter values, we construct posterior probability distributions for the fit parameters. The best-fitting model, the parameters, and their uncertainties are extracted from the posterior probability distributions.

Leighly et al. (2018) demonstrated the use of the “tophat accordion model” to model the opacity profile of broad absorption lines. Gaussian opacity profiles often fail to accurately model the heavily saturated BAL troughs or fit the small scale structures found within the wide troughs. The tophat accordion model uses a group of velocity-adjacent rectangular bins to divide the opacity profile into smaller-velocity segments. Each tophat bin may be allowed to have independent physical properties, or they may be constrained to have a common value. Therefore, not only do we obtain a better fit to the complex velocity structures of the BAL outflows, but we can also measure the physical properties of the outflowing gas as a function of velocity. Leighly et al. (2019) introduced a two-covering factor model where the absorption lines can have different partial-covering parameter $\log a$ values for the continuum and the emission lines.

Choi et al. (2020) discussed the updated atomic data and the grid of column densities created using *Cloudy* version c17.01 (Ferland et al. 2017). The main focus of the update was to incorporate more excited-state transitions and more iron-peak elements. However the line transitions from those excited-state ions or rare metal ions do not contribute to the spectrum for low-ionization and low-density BAL outflows. To save computation time, some of the objects were modeled using the column density grid from the older version of *SimBAL*, which used the c13.03 version of *Cloudy* (Ferland et al. 2013).

3.2. *Updates to* SimBAL

SimBAL has been updated to include three substantial enhancements that improve the accuracy of outflow parameters: (1) use of spectral eigenvectors for continuum fitting, (2) addition of anomalous reddening (Choi et al. 2020) as an option, and (3) incorporation of wavelength-dependent instrument resolution into the synthetic spectrum generation. The current version of *SimBAL* uses spectral eigenvectors from spectral PCA to model the emission lines. These eigenvectors enable *SimBAL* to employ only a small number of parameters for the emission-line model. A detailed discussion of the construction of the eigenvectors used in this paper is found in Appendix A.

We used a power law for the continuum, and the SMC reddening curve (Prevot et al. 1984) or a general reddening

---

[10] https://emcee.readthedocs.io/en/stable/

curve (Choi et al. 2020) to reproduce the reddening in the spectra depending on whether the object showed a typical continuum shape or anomalous reddening with a break.

Another update to *SimBAL* involves incorporating the instrument resolution into synthetic spectrum (MacInnis 2018). The spectrum data file from the SDSS provides information about wavelength dispersion at each pixel. *SimBAL* uses this information to create a resolution matrix and performs a convolution with synthetic spectrum with the matrix. The process is precisely analogous to the "Response Matrix Function" matrix used for forward modeling in X-ray spectral fitting. The shapes of the absorption lines change with the convolution; the principal effect is that the absorption lines with intrinsically narrow widths become noticeably shallower and wider in the spectra once the instrument resolution has been taken into account (MacInnis 2018). The other effect is aesthetic; the steps in the step-function opacity (from the tophat accordion model) appear smoothed out. Without the resolution convolution, *SimBAL* would modify the fit parameters to mimic the effect of the instrument resolution, finding a larger value for the partial-covering parameter $\log a$, corresponding to a lower covering fraction, and a larger BAL width. This added step not only helps *SimBAL* to create a more realistic spectrum that more closely matches the data but also provides more accurate properties of the outflowing gas when the lines are very narrow.

3.3. SimBAL *Analysis of FeLoBALQ Spectra*

SimBAL can model FeLoBALQ spectra with various spectral morphologies using the updates made to *SimBAL* (Section 3.2), and the software allows the use of user-defined models that are based on various physical models of BAL outflows. For example, in some objects (13 out of 53), we found evidence for more than one BAL outflow absorber in the spectrum, and we included more than one outflow component in their *SimBAL* models (Section 6.2). Each component was modeled using a set of accordion tophat bins or a Gaussian profile, each with their own independent set of physical parameters. The multiple-outflow components in a given object were found to have overlapping velocity structures, or they were observed to be completely separated by velocity (Figures 10; 11). These multiple BALs were treated as independent outflows so that the separate outflows were analyzed independently, and all figures include the points for these outflows. These outflows are identified with a letter of the alphabet following the name of the object (Appendix B). For some objects, strong narrow emission lines such as [O II]$\lambda\lambda$3726, 3729 were removed from the spectrum before model fitting.

When using the tophat accordion model for the absorption features, a fixed number of bins needs to be specified before the fitting process, and a user can decide if they want to allow each bin to have their own independent physical parameters, or a single set can be given to the entire ensemble of bins. We started by fitting the spectra with one ionization parameter ($\log U$) and density ($\log n$) for all bins. After we retrieved the preliminary model fits, we then tried to fit the objects with more flexible models where we would let the ionization parameter and/or density vary between bins. The number of bins for the tophat accordion models was determined based on the total width of the trough as well as whether the trough shows fine velocity structures. The tophat accordion models for some of the objects with narrow BALs used 3 bins, and the objects with the widest troughs used 12 bins. Considering the spectral resolution of the data ($\sim$70 km s^{-1}), the minimum bin width was $\sim$200 km s^{-1}. The choice of the total number of bins does not affect the *SimBAL* analysis, unless too few or too many bins are used (Leighly et al. 2018).

The default partial-covering model in *SimBAL*, the power-law partial-covering parameterized using $\log a$ (Leighly et al. 2018, 2019), provided robust model fits to the majority of our FeLoBALQs. Moreover, a *SimBAL* model can have two sets of partial-covering parameters each applied to the continuum emission and the emission lines separately to reproduce the difference between the partial-covering observed in continuum emission and in emission lines. However, six objects required a modified partial-covering scheme to obtain robust model fits (Section 5.1.1). The spectra of these six objects were initially fit with a pair of $\log a$ parameters in order to separately model the partial-covering of the line emission and the continuum emission. If the results of that fit argued that the line emission is not absorbed by the BAL components, then we proceeded with the modified partial-covering model where the BAL components are not allowed to absorb the line emission. We performed statistical tests (e.g., χ^2, *F*-test) to confirm our model selection.

Notes on the *SimBAL* model fits and specifications (e.g., number of tophat bins) for individual objects are given in Appendix C.

3.3.1. Objects and BALs Excluded from the Analysis

Based on preliminary analysis with *SimBAL*, we excluded three more objects from the initial sample of 53 objects: (1) the absorption features observed in the spectra showed properties more consistent with them being an intervening absorber than a quasar-driven outflow, (2) no clear FeLoBAL feature, with observable Fe II absorption lines, was detected in the spectra. Following the same reasoning, we also excluded several outflow components that were identified with using multi-component outflow models.

Some of the objects had very narrow features and only ground-state transitions that were more consistent with metal lines from intervening absorbers. They could be distinguished from intervening absorbers by partial-covering and kinematic properties (e.g., Hamann et al. 2011); see discussion in Appendix D. Additionally, the physical properties of a couple of BAL components could not be constrained reliably because only Mg II (and Al III in some cases) absorption lines were present in the spectra. For these reasons, we rejected two objects: SDSS J1057+6109 and in SDSS J0338+0056. The absorption lines that we found in SDSS J1057+6109 has an extreme offset velocity and the very narrow width of the absorption lines that suggested an intervening absorber. The best-fitting model for SDSS J0338+0056 identified an extreme LoBAL in this object with Mg II trough located at $\sim$2500 Å and spanning from $-43{,}300$ to $-26{,}400$ km s^{-1}, but no absorption from Fe II. Also, the assumed Mg II trough sits on top of the Fe II emission lines, which makes this BAL identification uncertain. No other absorption lines besides the Mg II trough were observed, and we could not constrain the physical properties of the BAL gas with any certainty. Therefore we excluded these two object from the analysis.

We excluded one of the two BALs found in SDSS J1214−0001 from further analysis. We identified two BAL systems in SDSS J1214−0001 (Pitchford et al. 2019); they were modeled with a Gaussian profile component for a narrow absorption component and a set of tophat bins for the broad trough feature. However, we could not get a reliable continuum emission model due to the broad tophat component with $v_{\rm width} \sim 10{,}800\ {\rm km\ s^{-1}}$ and $v_{\rm off} \sim -12{,}600\ {\rm km\ s^{-1}}$ covering the entire Fe II emission-line region (∼2200–2750 Å) with low apparent opacity. Furthermore, we found the constrained physical properties for this broad BAL component from the model fit to be unreliable. We kept the narrow BAL component from this object in the BAL sample because it was not affected by the uncertainty in the continuum emission placement. In addition, we did not find any absorption features in SDSS J1737+5536. This object was included in the Farrah et al. (2012) sample, but the best-fitting model did not yield any absorption lines. These three objects were excluded from further discussion, leaving 50 objects in our final sample.

In SDSS J1324+0320 and SDSS J1531+4852, we were able to clearly identify absorption features from metal lines from an intervening absorber. They were found at extreme offset velocities from the quasar rest frame ($v_{\rm off} \lesssim -20{,}000\ {\rm km\ s^{-1}}$) and had narrow absorption line width ($v_{\rm width} \lesssim 50\ {\rm km\ s^{-1}}$) that strongly suggested that these absorption lines did not originate in a quasar-driven wind. These absorption features were nonetheless modeled with *SimBAL* and included in the best-fitting model plots but are not included in the discussion.

The best-fitting model for SDSS J1644+5307 has two absorption components. The main Fe II trough and the most of the BAL features were fit using a six-bin tophat component, but an additional Gaussian component at lower velocity was needed to fit the deep Mg II trough. However, the lower-velocity component only appeared in Mg II, and therefore we could not reliably constrain its physical properties. Therefore this component was excluded from further discussion. Similarly, the best-fitting models for SDSS J0916+4534 and SDSS J1531+4852 have extra Gaussian components included to fit the low opacity absorption features ($I/I_0 > 0.9$) from the Mg II transitions located near the main BAL component. These components are essentially LoBAL absorbers. They improved the overall model fit, but we did not include them in the discussion because the opacity that they contributed was insignificant, and their physical properties could not be well constrained.

4. Calculation of Critical Parameters

4.1. Bolometric Luminosity Estimates and Spectral Index $\alpha_{\rm ui}$

The bolometric luminosities ($L_{\rm Bol}$) of the quasars used throughout the paper were calculated using the bolometric correction factor at 3 μm (BC = 8.59) from Gallagher et al. (2007b). The flux at rest-frame 3 μm was estimated from fitting the quasar composite SED by Richards et al. (2006) to the Wide-field Infrared Survey Explorer photometry data and interpolating the flux at 3 μm from the composite SED. The bolometric luminosity estimates are listed in Table 3 (column 8).

We defined α_{ui} to be the point-to-point spectral slope between rest-frame 2000 Å and 3 μm flux densities:

$$\alpha_{ui} = \frac{\log f_{3\mu{\rm m}} - \log f_{2000\text{Å}}}{\log \lambda_{3\mu{\rm m}} - \log \lambda_{2000\text{Å}}}.$$

We used the continuum emission model extracted from the best-fitting *SimBAL* model to estimate the observed flux density at rest-frame 2000 Å. The value of α_{ui} can depend on three quasar properties: reddening, the intrinsic shape of quasar SED, and the strength of the torus emission. For instance, a quasar that has either a flat or reddened SED, or has strong hot dust emission will have a flatter, i.e., larger value of $\alpha_{ui} \sim 0$. For reference, the Richards et al. (2006) composite quasar SED has $\alpha_{ui} \sim -1.23$. The values of α_{ui} for the sample are listed in Table 3 (column 9).

4.2. Derived-physical Properties and Kinematic Properties of the Outflows

Using the MCMC chains from the best-fitting *SimBAL* models, we computed the physical and kinematic properties of the outflows and the associated uncertainties. Throughout the paper, we report and plot median values and 2σ (95.45%) confidence intervals calculated from the posterior distributions as our uncertainty measurements. Some of the physical properties can be directly extracted from the *SimBAL* physical parameters: dimensionless ionization parameter ($\log U$, definition below), gas density ($\log n$ in [cm^{-3}]), column density (parameterized as $\log N_H - \log U$ in [cm^{-2}]), and dimensionless-covering-fraction parameter $\log a$ for the inhomogenous partial-covering ($\tau = \tau_{\max} x^a,\ x \in (0, 1)$; Arav et al. 2005; Sabra & Hamann 2005). We calculated the offset velocities and widths of the BALs, the distance of the BAL gas from the central supermassive black hole (SMBH) $\log R$, the mass outflow rate $\dot{M}$, and the kinetic luminosity $L_{\rm KE}$. The covering-fraction-corrected column density of the outflow was calculated by summing $\log U$ and $\log N_H - \log U$ and then correcting the values according to the $\log a$ to account for the power-law partial-covering ($\log N_H = (\log N_H - \log U) + \log U - \log(1 + 10^{\log a})$; Arav et al. 2005; Leighly et al. 2018, 2019; Choi et al. 2020).

The radius of the outflow (or the distance of the outflow from the central engine) can be calculated from $\log U$ and $\log n$ from the *SimBAL* results using the definition of the ionization parameter

$$U = \frac{\phi}{nc} = \frac{Q}{4\pi R^2 nc},$$

where ϕ is the photoionizing flux in the units of photons s^{-1} cm^{-2}, and Q is the number of photoionizing photons per second emitted from the central engine. We estimated Q from the SED fits of the photometry data for each object.

The mass outflow rate was calculated using

$$\dot{M} = 8\pi\mu m_p \Omega R N_H v,$$

where the mean molecular weight (μ) is assumed to be 1.4, the global covering fraction is given by Ω, and R, N_H, and v are calculated from the best-fitting parameters from *SimBAL*. This equation can be derived from taking the time derivative of $M = 4\pi\mu m_p \Omega R^2 N_H$, then substituting $dR/dt = v$ (assuming $dN_H/dt = 0$; Dunn et al. 2010). The value of the global covering fraction for FeLoBAL outflows is uncertain. The commonly used value $\Omega = 0.2$ (e.g., Hewett & Foltz 2003) was derived from a fraction of HiBALQs observed in the optically selected sample of quasars; the fraction can be as large as ∼0.4 for the luminous infrared-selected quasars (Dai et al. 2008). FeLoBALQs are a rarer kind of BALQs; the observed fraction can be as small as ∼1% in a given quasar sample (e.g., Trump et al. 2006;

Dai et al. 2012), but it is not clear whether their rarity reflects a small covering fraction, a short lifetime, or a selection bias that makes them difficult to detect. Detailed discussion on how to best explore the different values of the global covering fraction of FeLoBAL outflows can be found in Choi et al. (2020) where we also performed a multiple global fraction scenario with the idea that a BAL outflowing gas can be seen as different types of BALs depending on the viewing angle. In this work, we adopt a single global covering fraction $\Omega = 0.2$ that yields the mass outflow rate estimates for FeLoBALs that are slightly larger (∼0.5 dex) than the multiple global fraction scenario calculations (Choi et al. 2020). The strength of the outflow can be quantified by calculating the kinetic luminosity ($L_{\rm KE}$) of the outflows with the equation $\dot{E}_k = \dot{M}v^2/2$. The outflow column density, mass outflow rate, and kinetic luminosity for BALs modeled using tophat accordion models were calculated from the sum of the values calculated for each tophat bin.

In order to generate summary statistics for the widths ($v_{\rm width}$) and the offset velocities ($v_{\rm off}$) of the BAL outflows in a consistent manner, we adopted a method similar to calculating the balnicity index (Weymann et al. 1991). Continuum emission normalized spectra (I/I_0) for a single line transition were generated from the best-fitting *SimBAL* models, and the absorption features were defined as regions where the normalized flux I fell below 0.9. We used the Mg IIλ2796 line transition that has a higher transition probability ($f_{ik} = 0.609$) in the Mg II$\lambda\lambda$2796, 2803 doublet to generate the I/I_0 for all identified BAL outflows. We estimated the width of the outflow by identifying the start ($v_{\rm max}$) and the end ($v_{\rm min}$) of the absorption features. The summary offset velocity for each BAL component was estimated by calculating the opacity (column density) weighted velocities. We used

$$v_{\rm off} = \frac{\int v \times N_H(v) dv}{\int N_H(v) dv}$$

where N_H represents the covering-fraction-corrected hydrogen column density. The tophat accordion model produces physical parameters of the outflow as a function of velocity with which we calculated the summary offset velocity for an ensemble of tophat bins for a given BAL component. For Gaussian profiles, this calculation simply yields the velocity at the center of the profile. By calculating the velocity offsets this way, we avoid overestimating or underestimating the velocities compared to other metrics (e.g., $v_{\rm max}$), especially when the trough has extended low opacity features in one or both velocity directions. In this paper, we retain the signs for the offset velocities as calculated from the quasar rest frame: the outflows have negative offset velocities, and the inflows have positive velocities. For the objects that were modeled with more than a single BAL component, the outflow width and the velocity offset were measured for each component.

4.3. *Opacity Profiles and BAL Strengths of Select Transitions*

We extracted the opacity profiles of several absorption line transitions seen in FeLoBALs from the best-fitting *SimBAL* models in addition to the Mg IIλ2796 used to calculate the kinematic properties (Section 4.2). The transitions that we used are the ground-state Fe IIλ 2383 with $f_{ik} = 0.343$ and the excited-state (0.99 eV above ground) Fe II$^*\lambda$ 2757 with $f_{ik} = 0.307$. These are among the stronger transitions from Fe II multiplet in the near-UV band. We generated I/I_0 models for all BAL components with *SimBAL* from the MCMC chains of the best-fitting spectral models. The wavelength dispersion at each pixel was also taken into account in generating the profiles (Section 3.2). From the models, we visually inspected the shapes of the profiles and measured the kinematic information for each line transition. The widths for each transition were measured using the same method described in Section 4.2: we used the normalized flux at 0.9 as the boundary of absorption. In addition, we measured the velocity at the location of the minimum normalized flux for each transition. We emphasize that $v_{\rm off}$, opacity-weighted velocity (Section 4.2), is used throughout the paper as the representative outflow velocity; the velocities at the minima are just used to compare the kinematic properties of the three transitions (Section 6.3).

We extracted Ca II K, He I$^*\lambda$ 3889, and Hα information from the *SimBAL* models for each BAL component. We used the absorption strength (A) defined by Capellupo et al. (2011) to measure the BAL strengths. The absorption strength is defined as the fraction of the normalized flux removed by absorption. This empirical parameter may not accurately reflect the physical properties of the outflowing gas, but it can be used as summary statistics for the apparent BAL strength. For each BAL component, a single absorption strength value was reported from the averaged model flux within the absorption interval where $I/I_0 < 0.9$. To represent the strengths of Ca II doublet and Balmer series, we chose the transitions with the greatest transition probability, which are Ca II K and Hα, respectively. Depending on the redshift of the FeLoBALQs, the three line transitions of interest for some of the objects are located outside the bandpass of the SDSS/BOSS spectra used in this work. Moreover, we only modeled the spectra to ∼4700 Å, which means that the strongest Balmer transition observed in the given wavelength range was Hγ.

5. Results

5.1. *Best-fitting* SimBAL *Models*

We present *SimBAL* model fits of the FeLoBALQs. Figure 1 shows the best-fitting models of all 50 objects from the sample. From these results, we derived the physical properties and calculated the outflow properties, with associated uncertainties (Appendix B). We identified 60 BAL features, and 55 of them were classified as outflows with negative offset velocities. Eleven objects in the sample were modeled with more than one outflow component where either multiple sets of tophats bins or a combination of tophat bins and Gaussian profiles were used.

Analysis of SDSS J1352+4239 (Choi et al. 2020) showed that the outflow consisted of three components that were distinguished by their distinct physical properties as well as the kinematic properties. The majority of the multiple-outflow objects that we discovered in this sample were found using similar rigorous *SimBAL* modeling. We found that majority of the objects with the accordion tophat models were well fit with a single set of tophat bins with a single ionization parameter and density. Nonetheless, *SimBAL* model fits of some objects revealed a subset of bins that showed significantly different physical properties (e.g., ionization

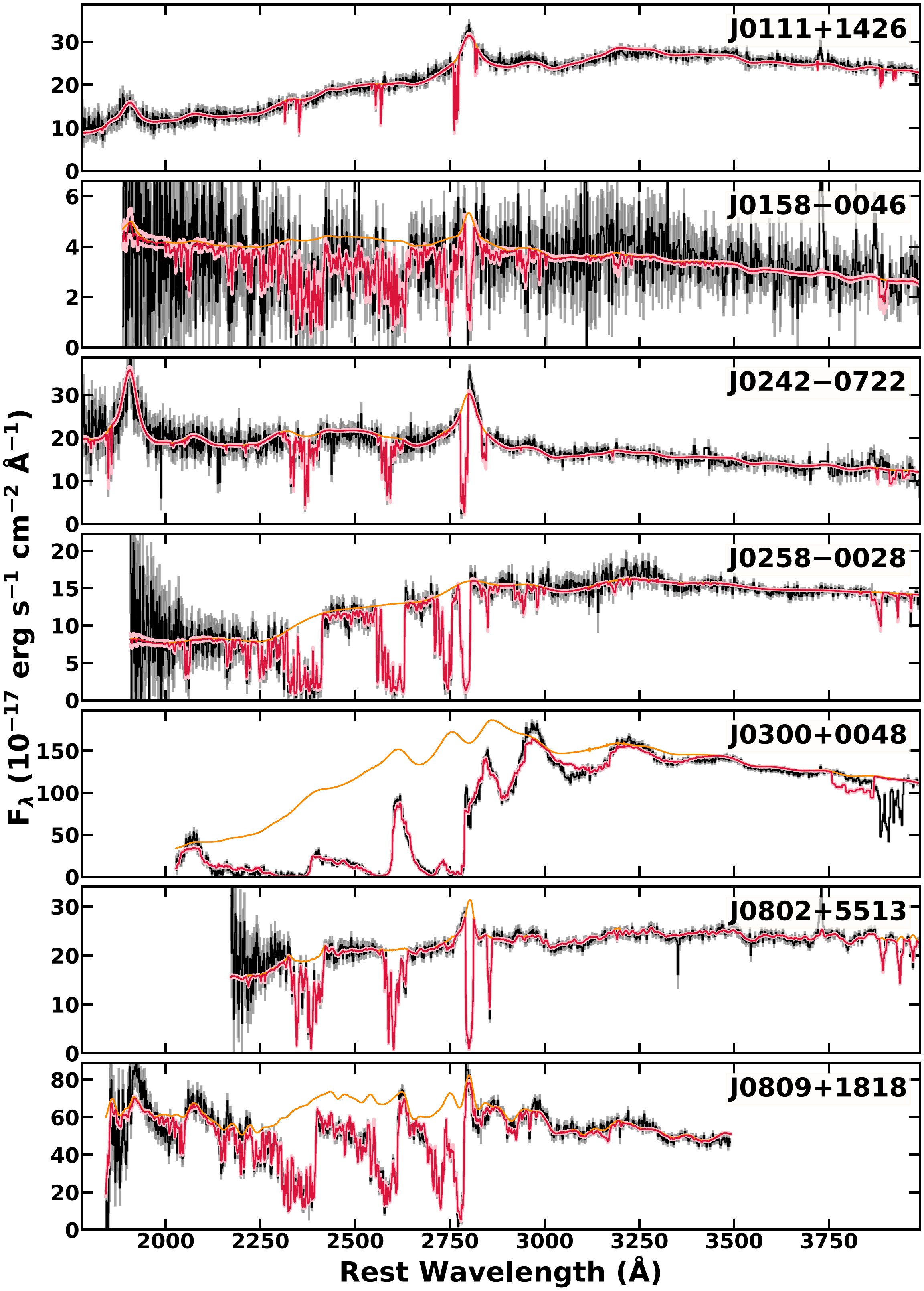

Figure 1. The best-fitting *SimBAL* models are plotted in red, along with the 2σ (95.45%) confidence models and unabsorbed continuum models in pink and orange, respectively. The binned data and the associated uncertainties are plotted in black and gray, respectively.

parameter and density). For those objects, we divided the tophat bins into two or three groups with a single ionization parameter and density for all bins in each group. In some objects a Gaussian profile was used for the lower-velocity components: SDSS J0258−0028, SDSS J1125+0029, and SDSS J1448+4043 (Figure 11).

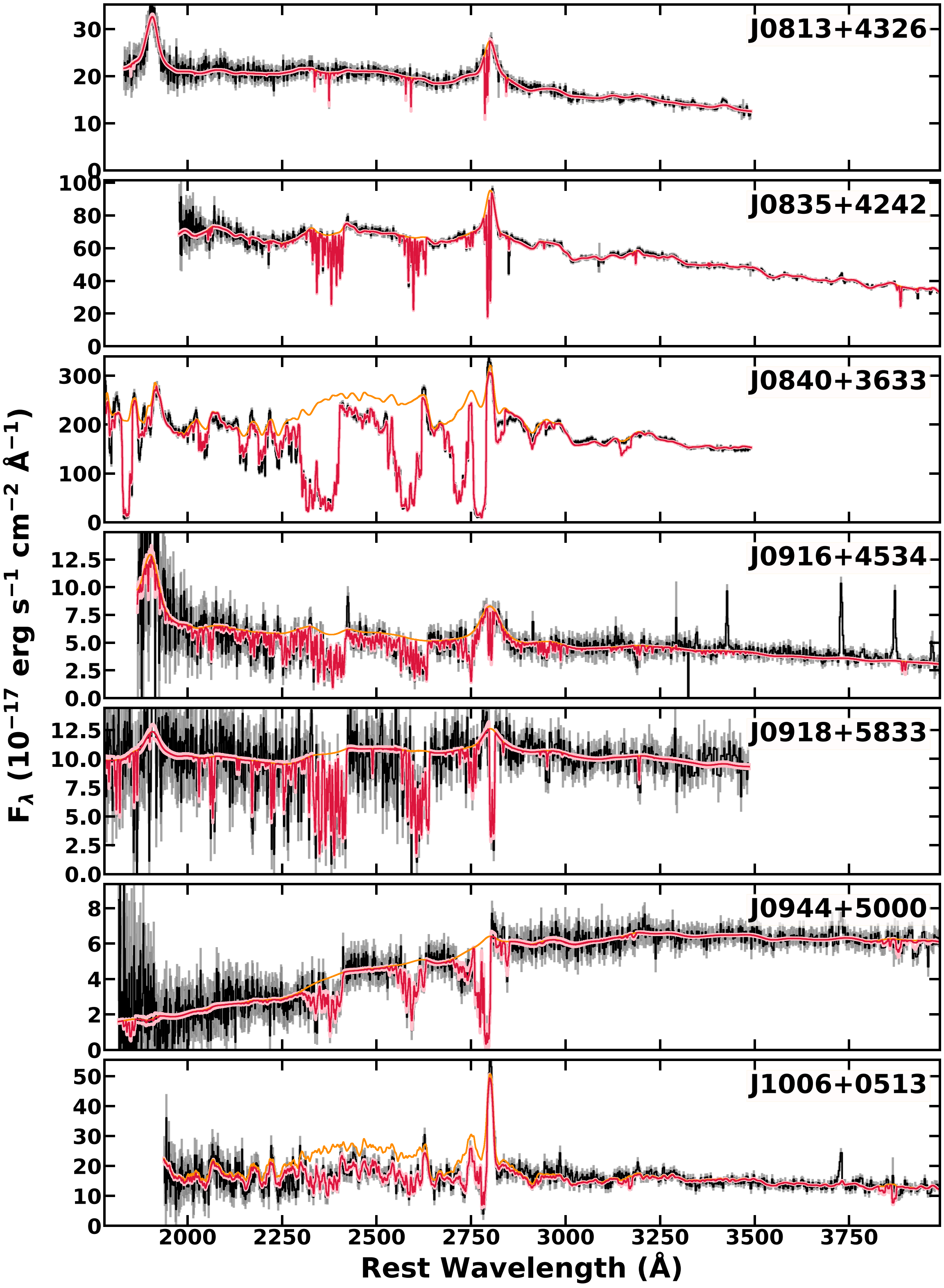

Figure 1. (Continued.)

5.1.1. SimBAL *Models with Modified Partial-covering*

Six objects in the sample required *SimBAL* models with the modified partial-covering scheme. The best-fitting models for SDSS J1128+0113, SDSS J1145+1100, and SDSS J1321+5617 included unabsorbed emission-line components and SDSS J1019+0225, SDSS J1125+0029, and SDSS J1644+5307 required a fraction of continuum emission to be unabsorbed by BALs (Figure 2). Five out of six objects are further classified as “loitering outflow objects” (Sections 5.1.3; 6.5).

In the extreme cases of nonzero flux at the bottoms of the troughs in the spectra of SDSS J1019+0225, SDSS J1125+0029,

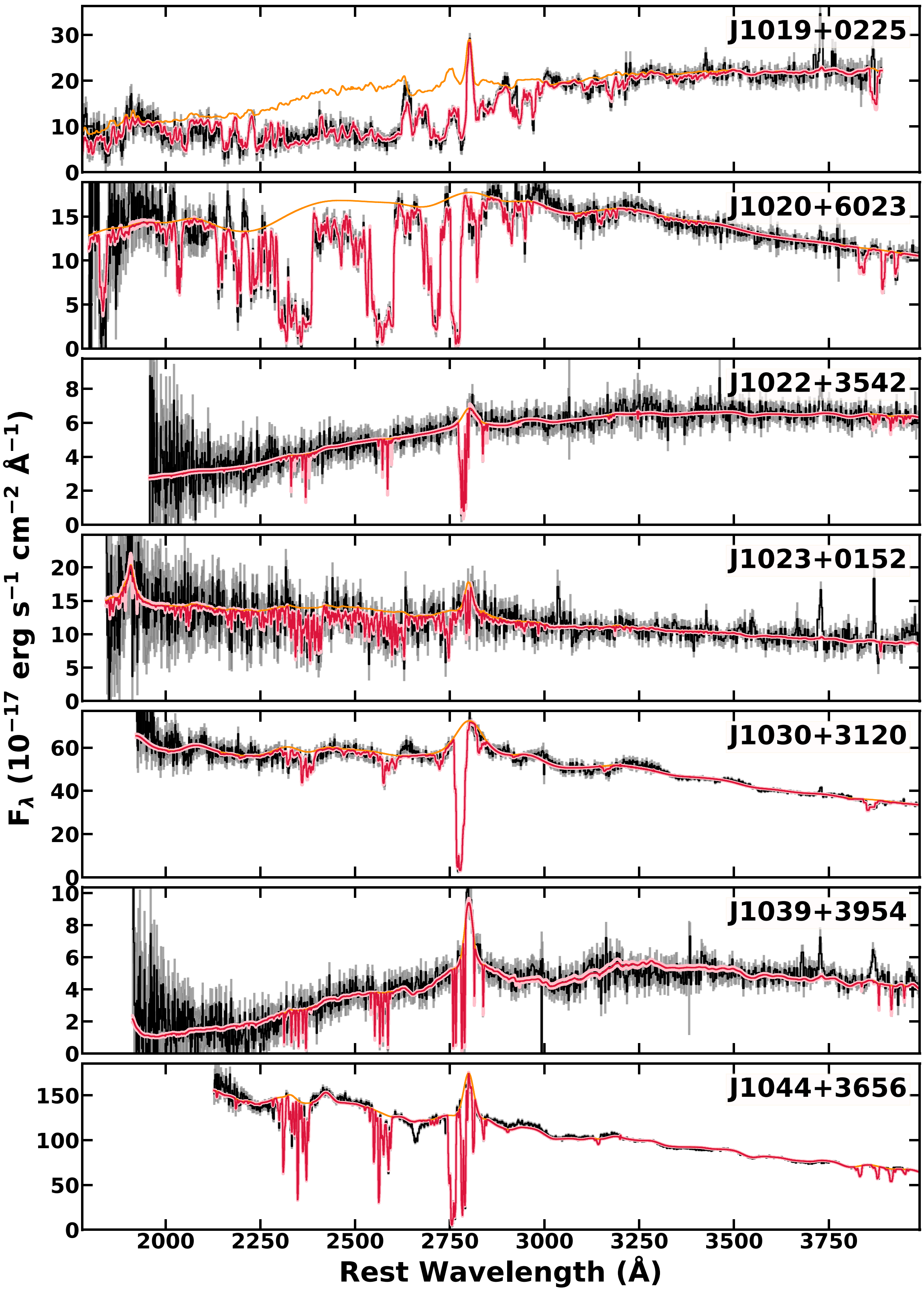

Figure 1. (Continued.)

and SDSS J1644+5307, an unabsorbed line-emission component alone was not sufficient to model the spectral features, and unabsorbed flux from the continuum emission was necessary to obtain the best-fitting spectral models. We modified the spectral model for these objects in two ways to account for the large amount of flux seen underneath the troughs. First, the line emission is not absorbed by the BAL, and second, only a fraction of power-law continuum emission is absorbed by BAL similar to the homogeneous step-function partial-covering (e.g., $I = C_f e^{-\tau} + (1 - C_f)$, C_f = covering fraction; Arav et al. 2005).

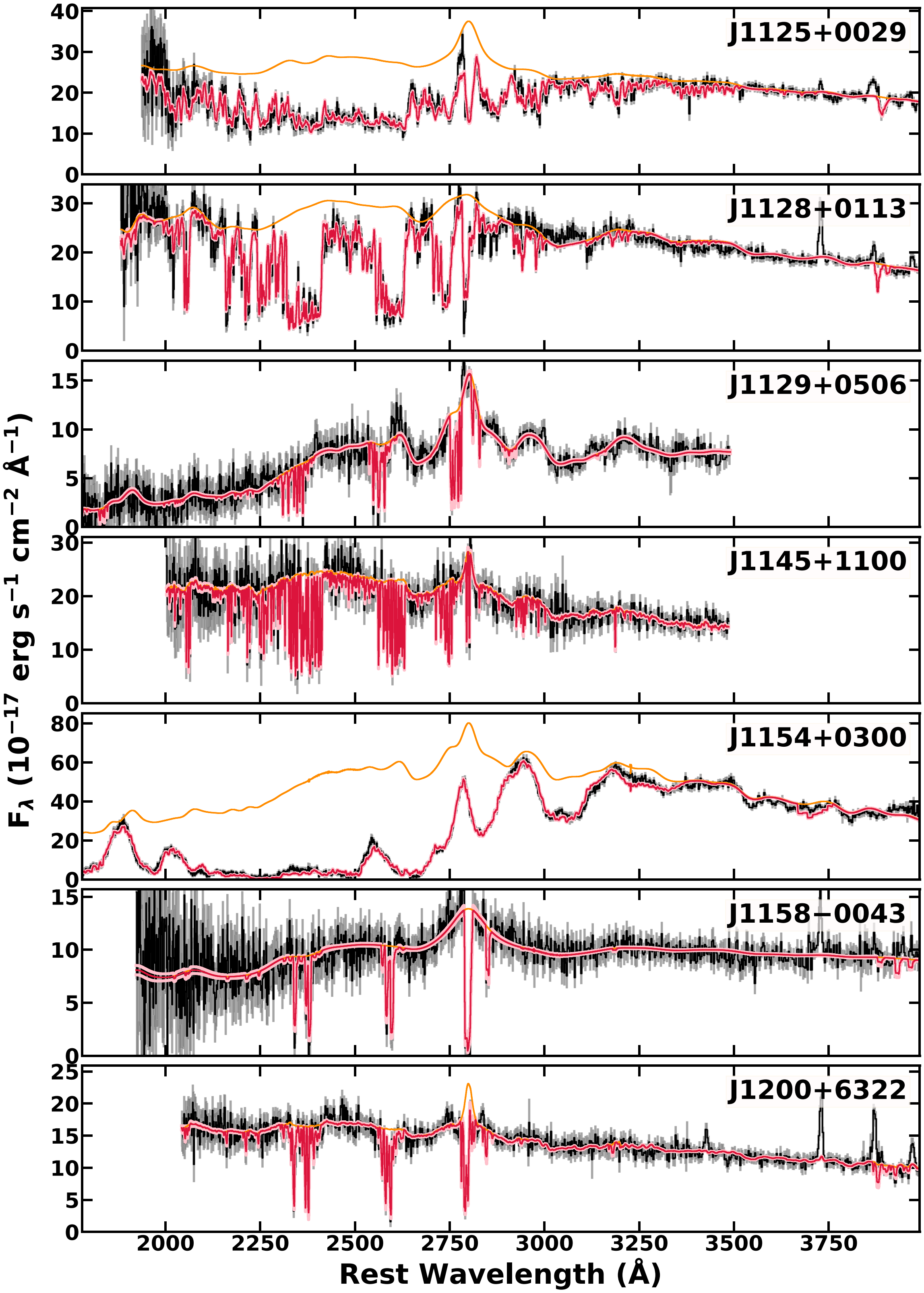

Figure 1. (Continued.)

The absorbed part still requires the power-law opacity ($\log a$) to model the significant contribution of weak absorption-lines. In other words, the BAL winds in these objects have both the inhomogenous partial-covering presumably originating from the complex cloud structures within the BAL gas (e.g., de Kool et al. 2002c; Leighly et al. 2019) and the homogeneous partial-covering that originates from the BAL gas absorbing only a fraction of continuum and none of the line emission from the central engine. With this model setup, we were able to create the overlapping-trough features with blended, saturated absorption lines and still

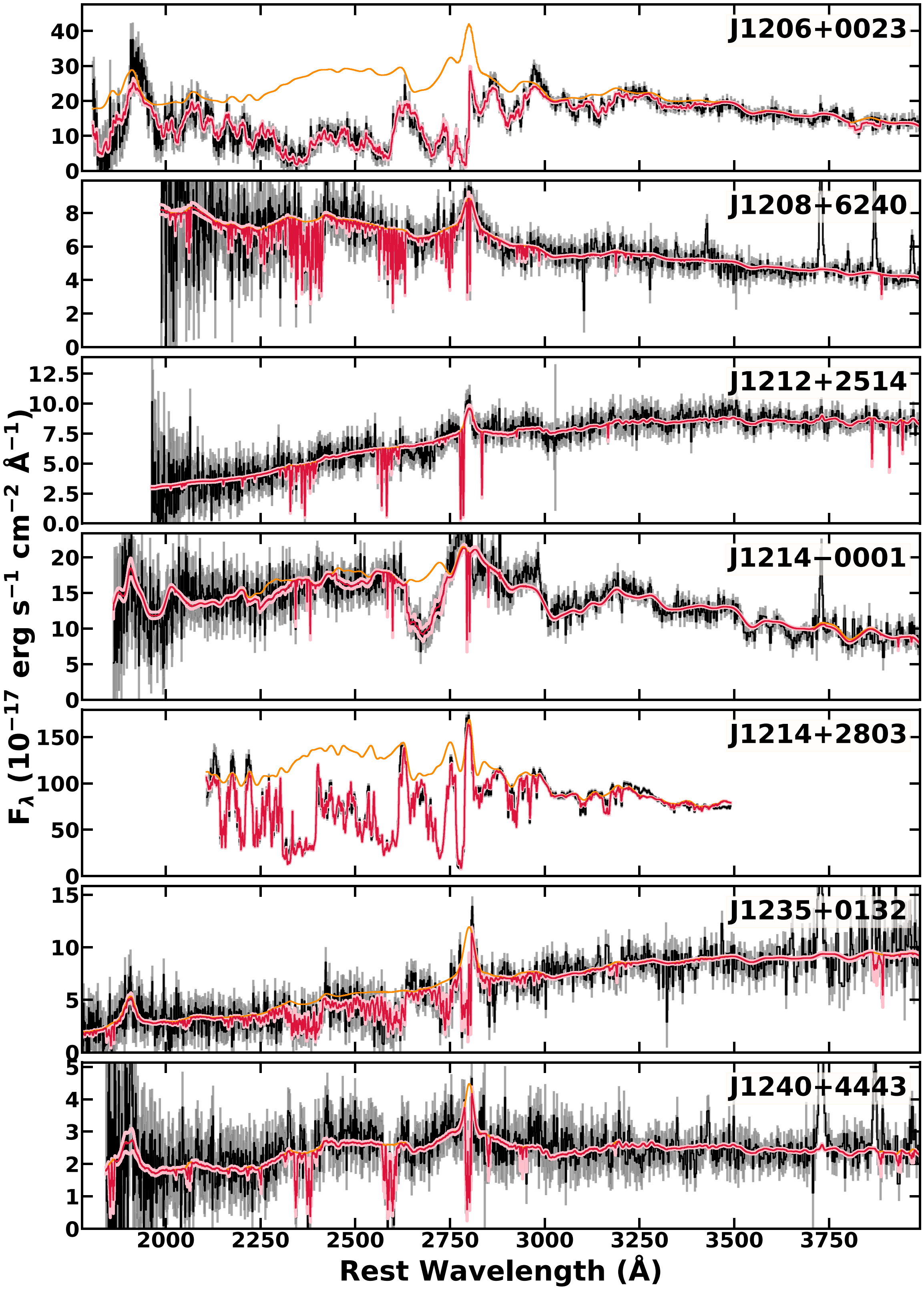

Figure 1. (Continued.)

have a significant amount of flux underneath the troughs. From the three objects, we obtained $C_f \sim 0.65$–0.71.

We note that the lower-velocity components in the spectral models for SDSS J1125+0029 and SDSS J1644+5307 were allowed to freely absorb both the continuum and line emission in a standard fashion unlike the higher-velocity components as described above. That is because the lower-velocity components in these objects are presumed physically separate from

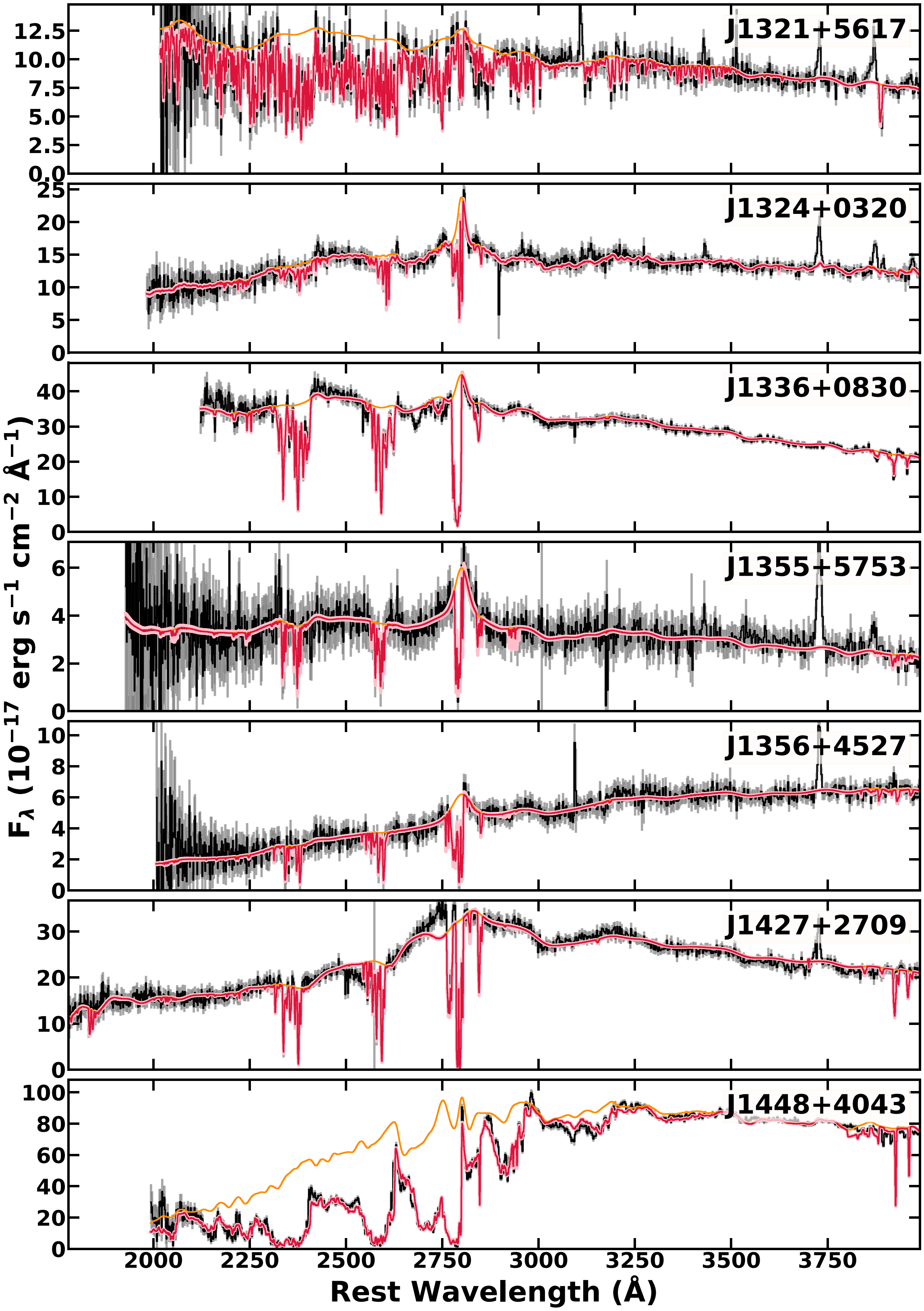

Figure 1. (Continued.)

the main higher-velocity component and are located at larger distances from the accretion disk and the BLR. This allowed the lower-velocity components to fit the deep Mg II absorption features seen in the spectra.

5.1.2. Absorption Lines in FeLoBALs

FeLoBALs are known to show absorption lines from Fe II as well as various iron-peak elements, such as Cr II, Ni II, in the near-UV wavelengths from their high column density gas (e.g.,

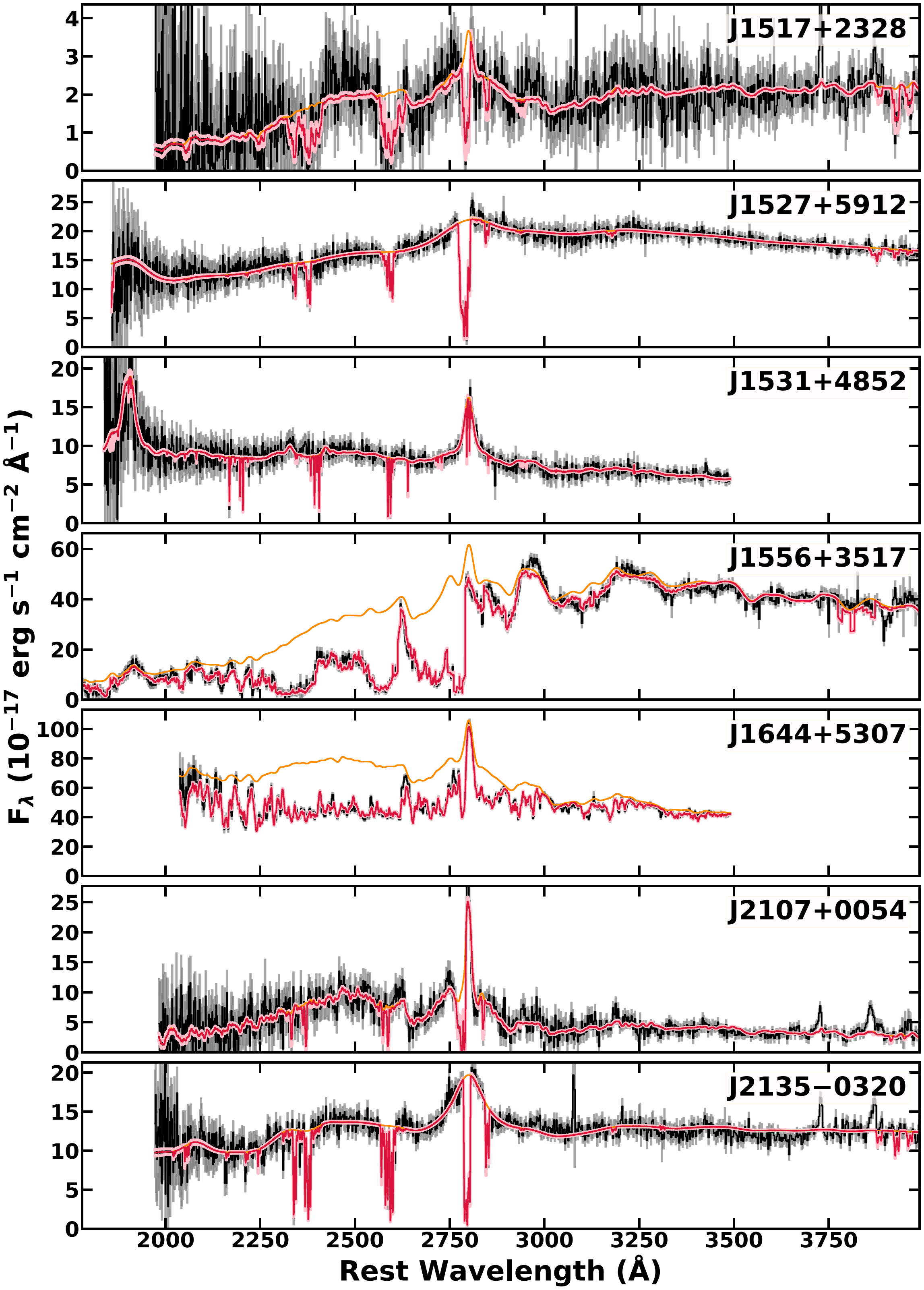

Figure 1. (Continued.)

Choi et al. 2020; de Kool et al. 2002b). Often these transitions are blended, and thus the isolation of individual line transitions is not possible in many cases, making it extremely challenging to analyze the FeLoBALQ spectra and to constrain the physical properties of the FeLoBAL absorbing gas. The forward-modeling technique used in *SimBAL* allows us not only to

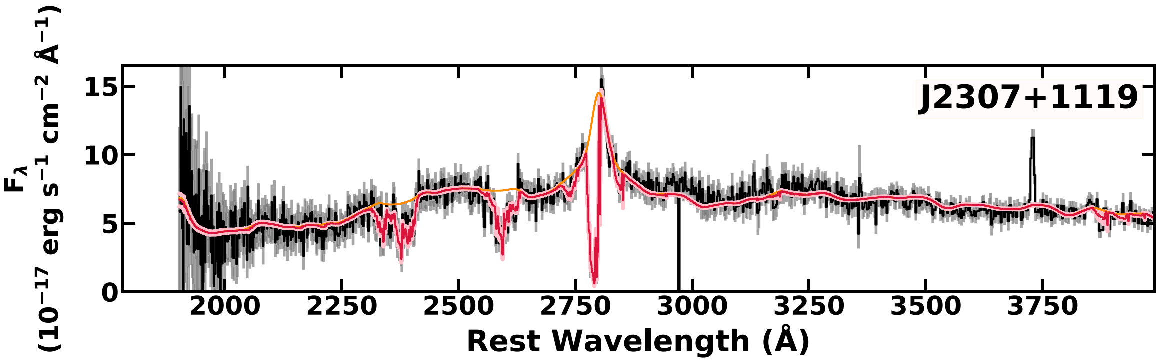

Figure 1. (Continued.)

analyze heavily absorbed spectra with line blending features but also to study the individual line transitions observed in the spectra by spectral synthesis.

Figure 3 highlights some of the major absorption lines observed in FeLoBALs with the special *SimBAL* models generated using the best-fitting model parameters and user-defined line transition lists. We used SDSS J1214+2803 as an example because this object has a high-opacity BAL absorbing gas ($\log N_H - \log U \sim 23.4$ [cm^{-2}]). The FeLoBAL in this object showed most of the prominent absorption lines found in FeLoBALs. The strength and/or the presence of (or the lack of) absorption lines from certain ionic species provide specific information about the physical conditions of the outflowing gas. The iron-peak elements are rare (e.g., [Ni/Fe] ~ -1.2 for $Z = Z_\odot$), and therefore their absorption lines only appear when the column density is sufficiently high, and these lines are often not saturated unlike Fe II or Mg II absorption lines. For example, the absorption feature near $\lambda \sim 2200$ Å from Ni II can be used as an excellent indicator of outflow column density. They suffer less line blending with Fe II absorption lines and produce stronger absorption lines compared to other rare iron-peak elements, such as Cr II. This particular feature is not observed in FeLoBALQs with low column density BALs (e.g., SDSS J2307+1119, $\log N_H - \log U \sim 23.0$ [cm^{-2}] in Figure 1). In addition, the absorption line from He I* λ 3188, also noted in Figure 3, has been previously known for its column density and ionization diagnostics (Leighly et al. 2011). For FeLoBALs, the ionization parameter is directly related to the column density of the gas (Section 5.3; Figure 7), which means the overall amount of opacity observed in the troughs scales with ionization, and this parameter is constrained by not only a subset of line transitions but also an ensemble of absorption lines.

The bottom panel in Figure 3 shows the models of Fe II absorption lines that have been grouped by the lower-level excitation energy. Fe II has a large number of excited-state levels, and the plethora of absorption lines that they produce can be used to constrain the density of the outflowing gas (e.g., Lucy et al. 2014; Choi et al. 2020). Most FeLoBAL quasars show excited-state Fe II* absorption lines with lower-level excitation of $E_{\text{lower-level}} \sim 1$ eV in their spectra (e.g., SDSS J0840+3633). Most excited-state Fe II transitions have critical densities $\log n \sim 4.5$ [cm^{-3}] or greater (e.g., Korista et al. 2008). If the density exceeds this value, then the BAL will show strong absorption lines from Fe II across various excited energy levels, including high-excitation levels ($E_{\text{lower-level}} \sim 5$ eV) especially when the density is high. For instance, SDSS J1214+2803 shown in the figure has a high-density outflowing gas ($\log n \sim 7.8$ [cm^{-3}]), and we observe significant opacity from the Fe II* absorption lines form multiple excited levels. If an absorbing gas has low enough density and no Fe II in the excited states, then the FeLoBAL will mostly only show absorption features from the ground-state Fe II (e.g., SDSS J0802+5513, $\log n \sim 4.4$ [cm^{-3}]). In some BALs with no excited-state Fe II* absorption lines, we were only able to constrain density upper limits ($\log n \ll 2.8$ [cm^{-3}], column density grid limit). And thus, these BALs will have lower limits on their distance estimates from the central engines (see Section 4.2). Also, the high-ionization condition can populate Fe II to excited states.

5.1.3. Classifications of FeLoBALs

In the figures throughout the paper, we mark three special types of FeLoBALs identified in the sample: (1) overlapping troughs, (2) loitering BALs, and (3) inflows. The overlapping-trough identification was done based on the spectral morphology. If an object showed heavily blended Fe II absorption feature in the spectrum shortward of $\lambda \sim 2800$ Å, then we classified it as having overlapping-trough features (e.g., SDSS J0300+0048 and SDSS J1154+0300). Second, based on the outflow properties obtained from *SimBAL* modeling, we classified "loitering BALs" by selecting BALs that have $\log R < 1$ [pc] and $|v_{\text{off,FeII excited}}| < 2000$ km s^{-1} (offset velocities calculated from the excited-state Fe II* λ2757; Section4.3). Lastly, the inflows ($v_{\text{off}} > 0$ km s^{-1}) were classified based on the opacity-weighted velocities (Section 4.2). We note that unlike the loitering BAL or inflow classifications, the overlapping-trough classification is solely based on empirical visual classification and not based on the physical and kinematic properties. Also, FeLoBAL can have multiple classifications. For instance, the majority of loitering BALs are also classified as overlapping troughs and inflows. Following the classification scheme, we identify the following: 8 overlapping troughs, 11 loitering BALs, and 5 inflows. 41 out of 60 FeLoBALs do not belong in any of the three special classes, and they can be considered typical outflowing FeLoBALs with moderate opacity. Detailed discussion on overlapping troughs and loitering BALs can be found in Sections 6.4 and 6.5, respectively.

Following the theoretical predictions (e.g., Scannapieco & Oh 2004; Di Matteo et al. 2005; Hopkins & Elvis 2010), we identified energetic BALs as those that have outflow energy (L_{KE}) greater than 0.5% of the bolometric luminosity (L_{Bol}) of the quasar. Because some of the BAL outflows were constrained with lower limits on the distances of the BAL absorbers from the central engines, not all BALs in our sample have robust constraints on the outflow energy calculations.

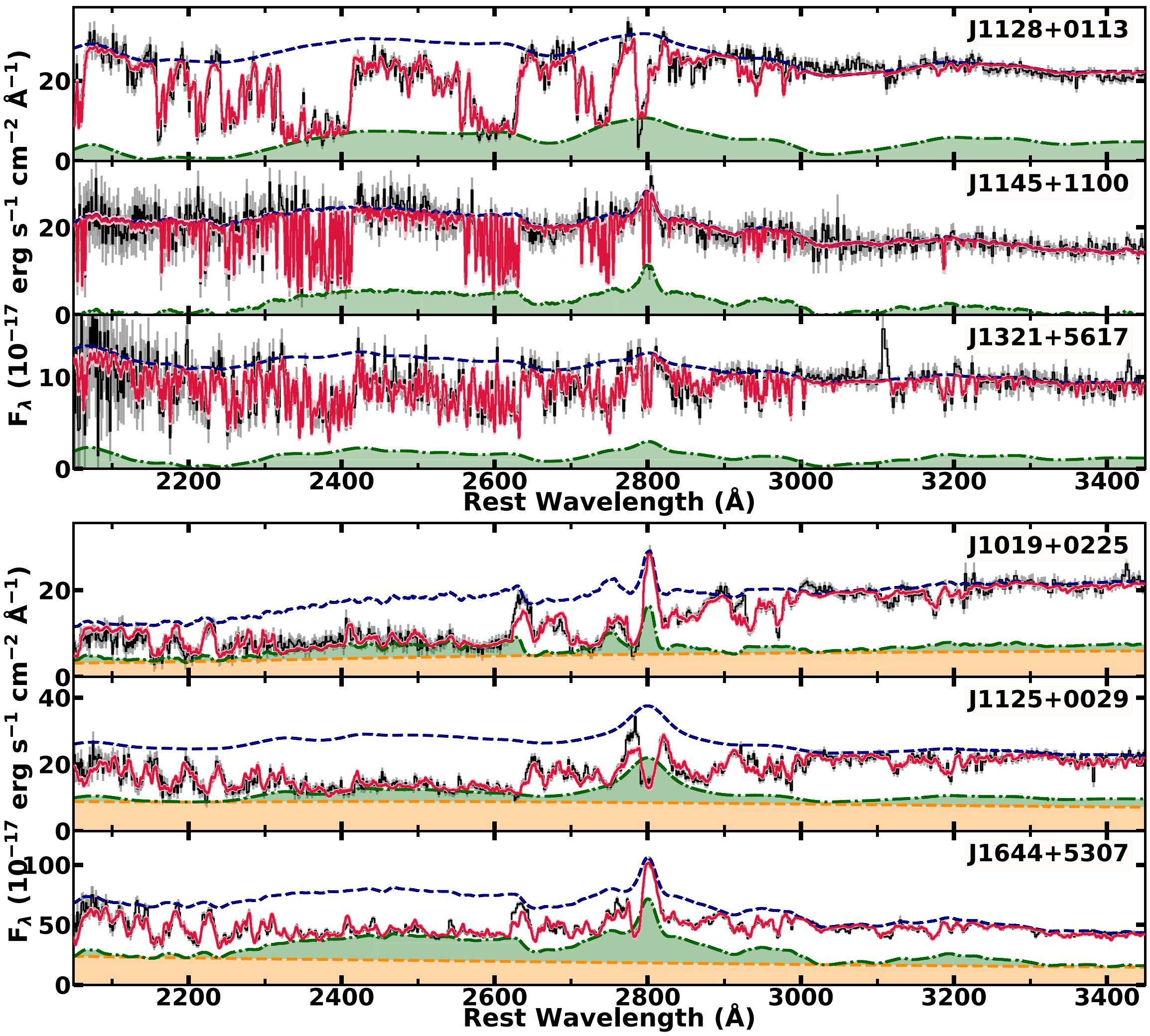

Figure 2. The best-fitting *SimBAL* models for six objects modeled using the modified partial-covering scheme. The best-fitting models and the unabsorbed continuum emission models are shown in red solid lines and blue dashed lines, respectively. *Top*: the FeLoBAL gas does not absorb the emission lines (green shaded region). *Bottom*: the FeLoBAL gas does not absorb both emission lines and a fraction of the continuum emission (green and orange shaded regions). The power-law partial-covering (log *a*) used in *SimBAL* alone could not model the heavy nonblack saturation seen in these spectra.

Therefore, among the energetic BALs that meet $L_{\mathrm{KE}} > 0.005 L_{\mathrm{Bol}}$ condition, we only selected the ones with well-constrained physical properties (e.g., $\log U$, $\log n$) as powerful BALs. They are represented in the figures with cyan (or pink) square outlines.

5.2. Best-fitting Parameters

5.2.1. Physical Gas Properties of the BALs

Figure 4 shows the distribution of $\log U$, $\log N_H - \log U$, and $\log n$ of the FeLoBALs in our sample. The FeLoBALs have a wide range of ionization parameter ($\log U \sim -4$ to 1.2) and density ($\log n \sim 2.8 - 8.0$ [cm^{-3}]); these values span our computational grid. Most of the BALs have column density parameter ($\log N_H - \log U$) high enough to encompass the hydrogen ionization front ($\log N_H - \log U \sim 23$ [cm^{-2}]). This high column density is expected for FeLoBALs because a column density thick enough to include the hydrogen ionization front is necessary to produce the observed Fe II absorption (e.g., Lucy et al. 2014). As shown in the left panel of Figure 4, we found no FeLoBALs with $\log U > -1.5$ and $\log N_H - \log U < 22.9$ [cm^{-2}], because insignificant Fe II is produced in that region of parameter space.

Starting at lower-$\log U$ FeLoBALs ($\log U \lesssim -2$), the outflows have lower density ($\log n \lesssim 5$ [cm^{-3}]), and some of them have column densities insufficient to breach the hydrogen ionization front ($\log N_H - \log U \lesssim 23$ [cm^{-2}]). The physical condition of the gas at the low-ionization parameter and density does not dramatically change across the hydrogen ionization front in the lower-$\log U$ gas, and thus the ionic column density of Fe II gradually increases across the ionization front. Therefore, BAL gas with lower $\log U$ can populate Fe II ions even at the slightly lower $\log N_H - \log U$ before the gas column density encompasses the hydrogen ionization front. Their spectra are least absorbed with no significant line blending or saturation, and often the individual absorption lines can be easily identified. The opacity mainly comes from the ground-state Fe II and Mg II with weak or no observable opacity from the excited-state Fe II or other rare metal ions (e.g., SDSS J0835+4242, SDSS J1240+4443 in Figure 1). Although we were able to constrain the densities of most FeLoBALs, we assigned density upper limits for some of the low $-\log U$ FeLoBALs that showed no absorption lines from the excited-state Fe II.

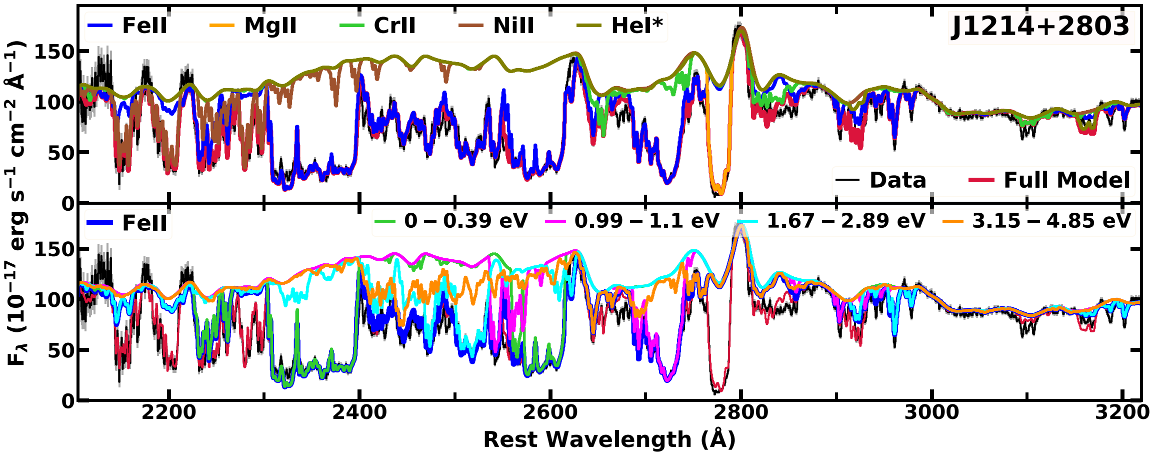

Figure 3. Anatomy of the near-UV spectrum of an FeLoBAL quasar. *SimBAL* models for SDSS J1214+2803 showing some of the principal line transitions observed in FeLoBAL troughs are plotted. *Top*: the best-fit model has been divided by the ionic species that are the major contributors of the opacity in the near-UV bandpass for FeLoBALs. *Bottom*: the Fe II model has been further broken up into 4 different models depending on the lower-level excitation energy.

Most of our FeLoBALs have a moderate ionization parameter of $\log U \sim -2$. These medium $-\log U$ FeLoBALs have the widest range of densities, spanning the entire range that we found in our sample ($2.8 \lesssim \log n \lesssim 8.0$ [cm^{-3}]). These FeLoBALs have the spectral morphology of *typical* FeLoBALs with strong absorption lines from Mg II and ground-state Fe II as well as excited-state Fe II and other iron-peak elements depending on the gas density and column density (e.g., SDSS J0840+3633, SDSS J1214+2803 in Figure 1). Moreover, the standard BAL spectral features (e.g., nonblack saturation, line blending) can be easily found in their spectra. Most of the previously well-studied FeLoBALs belong to moderate $-\log U$ FeLoBALs (e.g., QSO2359−1241, Arav et al. 2001; FIRST J104459.6+365605, de Kool et al. 2001; FBQS 0840+3633, de Kool et al. 2002a; FIRST J121442.3+280329, de Kool et al. 2002b).

We discovered a number of FeLoBALs with high ionization parameter ($\log U \gtrsim -1$; e.g., SDSS J0158−0046, SDSS J1154+0300 in Figure 1), which were responsible for the large range of ionization parameter that we found in our FeLoBAL sample. High-ionization FeLoBALs have higher column density gas that includes a significantly larger number of excited-state ions compared with the low-$\log U$ FeLoBALs. Most of the FeLoBALs with high ionization parameter also have special classifications, due to their spectral morphology and physical properties (e.g., overlapping-troughs, loitering BALs; Section 5.1.3). These high opacity FeLoBALs (e.g., overlapping-trough BALs) have not been previously analyzed in detail due to the difficulty in analyzing FeLoBALQs with the extreme absorption features that are often seen in these objects.

The FeLoBALs with higher $\log U$ also have higher $\log n$ and larger $\log a$ (less covering; Figure 4). The absence of FeLoBALs with high ionization and low density can be explained by the geometrical constraints expected from the outflows. The physical thickness of outflowing gas ($\Delta R \sim U/n$, for a fixed $\log N_H - \log U$) cannot be greater than the distance of the gas from the central engine ($\log R$). The overlapping-trough BALs and loitering BALs (marked with red circles and blue diamonds, respectively) have both higher $\log U$ and $\log n$ compared to the rest of the BALs. The trend between $\log U$ and $\log a$ might be as a selection effect. In high-$\log U$ outflows, the large amount of opacity from the larger number of excited-state ions and rare metal ions would heavily absorb the quasar spectrum. Therefore, unless the covering fraction is low (high $\log a$), FeLoBALs with high $\log U$ cannot be detected easily.

5.2.2. Kinematic Properties of the BALs

Figure 5 shows how the kinematics of the outflow (e.g., outflow velocity and width) compare with the physical properties of the gas (i.e., $\log U$, $\log n$, and $\log N_H - \log U$). Of the 60 BALs in our sample, we found 5 BALs with positive offset velocities (SDSS J0158−0046, SDSS J0802+5513, SDSS J0916+4534, SDSS J0918+5833, and the second BAL component in SDSS J1125+0029). We have robust redshift measurements for theses objects from the narrow emission lines of [O II], narrow Hβ component, or high-ionization [Ne V] line. The offset velocity of the FeLoBALs does not seem to be correlated with either $\log U$ or $\log N_H - \log U$, and for a given outflow velocity, we found a wide range of physical properties. However, we found that the FeLoBALs with the highest velocities have higher ionization parameters, but the converse is not true. The subtle v-shaped distribution seen between $v_{\rm off}$ and $\log U$ potentially suggests that there may be more than a single population within FeLoBALQs; this topic as well as the analysis of the relationship between quasar properties (e.g., Eddington ratio) and outflow (kinematic) properties are explored further using the Hβ/[O III] properties in Choi et al. (2022). We discuss the potential acceleration mechanisms for the FeLoBAL outflows in Section 7.2.

The distribution of the widths and the velocities of the outflows show a nearly one-to-one relationship (the right panel in Figure 5). This suggests that most of the outflows in our sample have widths similar to the offset velocities; the outflows are not detached but rather they start from near rest ($\sim$0 km s^{-1}). Our result is consistent with what has been seen in composite spectra of BALQs that showed troughs beginning from near the peaks of the emission lines (Hamann et al. 2019a; Rankine et al. 2020). The outflows with the higher velocities have proportionately larger widths and tend to have higher densities compared to other outflows in our sample, although there are also FeLoBALs with low velocity and high density. Most of the overlapping-trough BALs (red circles in Figure 5) have the highest outflow velocities with large widths as well as high density.

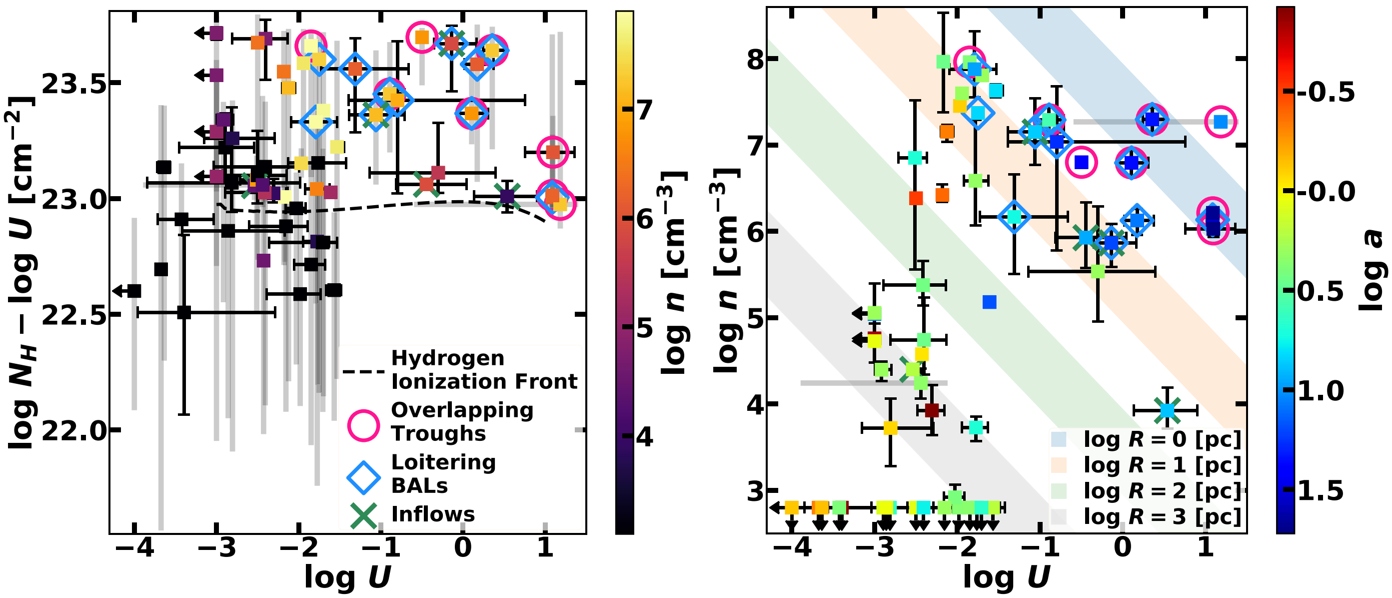

Figure 4. The FeLoBAL outflows in our sample show a wide range of physical properties including ionization parameter (log U) and density (log n). The gray shaded bars represent the range of values among the tophat model bins for each BAL. For Gaussian opacity profile models or when the tophat bins for a given BAL had a single ionization and/or density parameter, the 2σ (95.45%) uncertainties from the MCMC posterior distributions are plotted as error bars. Some of the special BALs are marked as follows: red circles for overlapping-trough BALs (Section 6.4), blue diamonds for loitering BALs (Section 6.5), and green crosses for inflows. *Left panel*: the dashed line shows the location of the hydrogen ionization front as a function of ionization parameter. *Right panel*: the locations of the BAL gas from the central SMBH (log R) are marked as shaded areas for reference. They were calculated assuming the typical ranges of photoionizing photon flux used in our sample of FeLoBALQs (log $Q \sim 55.5$–56.5 [photons s^{-1}]).

5.3. Derived-physical Properties of the Outflows

The large range, in ionization parameter and density observed, means that the outflows are located throughout the quasar, ranging from near the torus at log $R \sim 0$ [pc] to the host galaxy log $R \sim 3$ [pc]. We recovered an inverse relationship between log R and the two gas parameters log U and log n that can be explained with the definition of log U ($U \propto 1/nR^2$). Given the range of the total number of photoionizing photons per second (Q) from the AGN for the objects in our sample and the range of densities that we have for the BAL clouds, we can identify a region in the log $R-$log U parameter space where we expect the BALs to be located. If the values of log U and log n were distributed evenly for our sample of FeLoBALs, we would find them evenly distributed in the area between the two dashed-shaded strips for log n = 3 and 8 [cm^{-3}] in Figure 6 (calculated assuming log N_H − log $U = 23 \sim 23.5$ [cm^{-2}] and log $Q \sim 55.5 - 56.5$ [photons s^{-1}]); it is clear that they are not. Instead of a uniform distribution, we find that high-log U outflows have higher log n, and the outflows with lower log n tend to have lower log U as well. This behavior is found because most of our FeLoBALs have a small range of volume filling factors (or normalized radial widths, log $\Delta R/R \sim -5$; log $\Delta R = \{\log U + (\log N_H - \log U)\} - \log n$) except for the compact BALs that are located log $R \lesssim 1$ [pc], which have large volume filling factors (log $\Delta R/R \gtrsim -3$). We discuss this point and other geometrical constraints in Paper III (Choi et al. 2022).

We found mass outflow rates of $\dot{M}_{\rm out} = 0.049 \sim 520$ M$_\odot$yr^{-1}. The mass outflow rates span more than four orders of magnitude, which reflects the wide range of $v_{\rm off}$ that we found in our FeLoBAL outflows. We also report mass inflow rates of $\dot{M}_{in} = 0.016 \sim 55$ M$_\odot$yr^{-1} from the 5 BALs with $v_{\rm off} > 0$ km s^{-1}. For a couple of BAL components with $v_{\rm off} \sim 0$ km s^{-1} that were modeled using tophats, we calculated both the mass outflow and inflow rates depending on the velocities of the bins. Except for SDSS J1125+0029 in which there is an additional outflowing BAL, SDSS J0158−0046, SDSS J0802+5513, SDSS J0916+4534, and SDSS J0918+5833 only showed inflow BALs and did not have other outflowing BALs in the spectra. These inflow BALs are mostly located within log $R < 2$ [pc] (one at log $R \sim 3$ [pc]) and have low offset velocities ($v_{\rm off} \lesssim 600$ km s^{-1}). We note that there is a caveat that mass outflow rates are dependent on the assumed global covering fraction (Ω) of (FeLo)BALs. We used $\Omega = 0.2$ in this work (Section 4.2), and detailed discussion on the global covering fraction for FeLoBALs can be found in Choi et al. (2020).

Figure 7 shows that the higher log U outflows have higher partial-covering-corrected column density. The correlation may be an artifact of sample selection because the column density of the outflowing gas needs to be high enough to reach the hydrogen ionization front for the FeLoBALs (log N_H − log $U \gtrsim 23.0$ [cm^{-2}], left panel in Figure 4; Section 5.2.1). Moreover, we see a relatively small dynamic range of about 1 dex across log N_H − log U whereas log U ranges from ~-4 to $\sim$1.5. From the distributions of the parameters alone, we can expect log N_H is highly dependent on log U so that the gas with higher log U also has higher log N_H.

The mass outflow rate ($\dot{M}$) does not seem to be strongly correlated with either ionization parameter or partial-covering-corrected column density. Outflows with high mass outflow rates ($\dot{M}_{\rm out} \sim 100\, M_\odot$ yr^{-1}) were found across the entire log N_H and log U range. This is because the magnitude of the mass outflow rate is mainly determined by the outflow velocity rather than the location or the physical properties of the gas (Section 6.1).

We found a strong correlation between the outflow strength and the outflow velocity (Figure 8). Considering that $\dot{M} \propto v$,

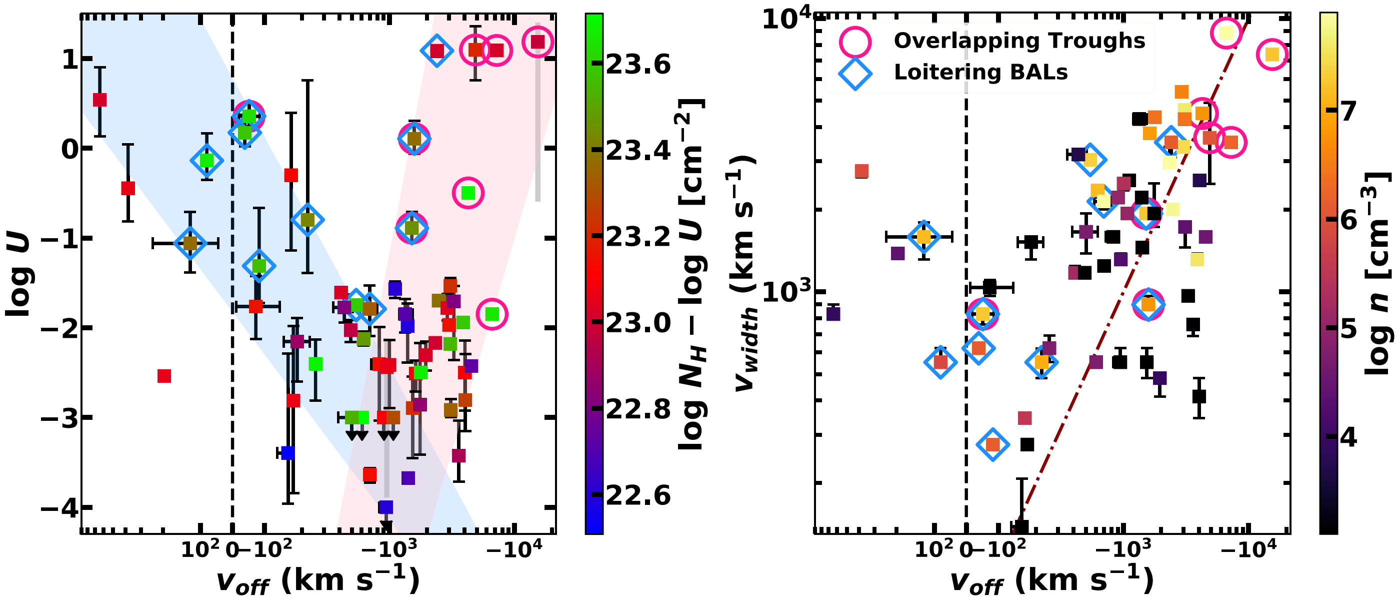

Figure 5. *Left panel*: we found no strong correlations between the offset velocities and the physical properties of the BAL gas (log U and log N_H − log U) for the whole FeLoBAL sample. Instead, there is a "v" shape with high-log U BALs present at the lowest and highest velocities (red and blue shades). *Right panel*: the widths of the BALs scale with the velocity offsets. The distribution roughly follows a one-to-one ratio (brown dotted–dashed line), which indicates that most of the FeLoBAL outflows are not detached from the emission line at rest. A linear scale was used in the region $|v_{\rm off}| < 100$ km s^{-1}, and log scale was used elsewhere in the x-axis. Markers and error bars as in Figure 4.

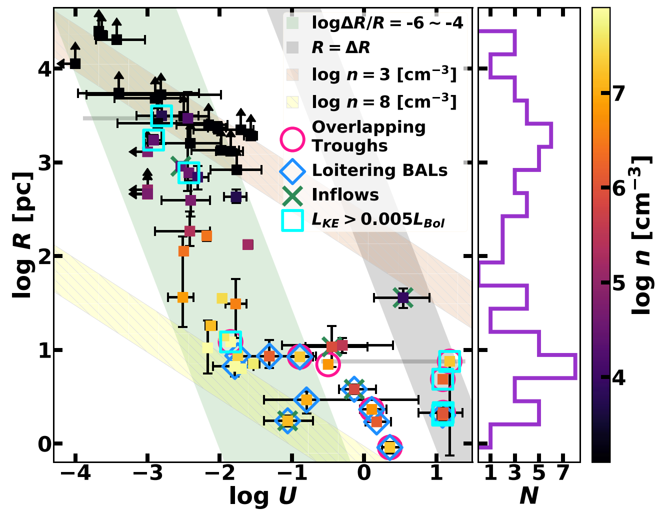

Figure 6. The BALs have a wide range of distances from the central engine, ranging from a torus scale (∼pc) to a host-galaxy scale (∼kpc). The cyan squares mark the powerful outflows that have well-constrained physical parameters (log U and log n) and kinetic luminosity ($L_{\rm KE}$) greater than 0.5% of the bolometric luminosity of the quasar ($L_{\rm Bol}$). The powerful outflows are located in a various distances from the central black hole, and they have a variety of physical properties. The histogram on the y-axis shows the distribution of log R in our sample. There is a lack of FeLoBALs near log R ∼ 2 [pc] (Section 7.1). A range of BAL cloud volume filling factors (or normalized radial widths, log ΔR/R) and two log n values are marked as shaded areas for reference. Markers and error bars as in Figure 4.

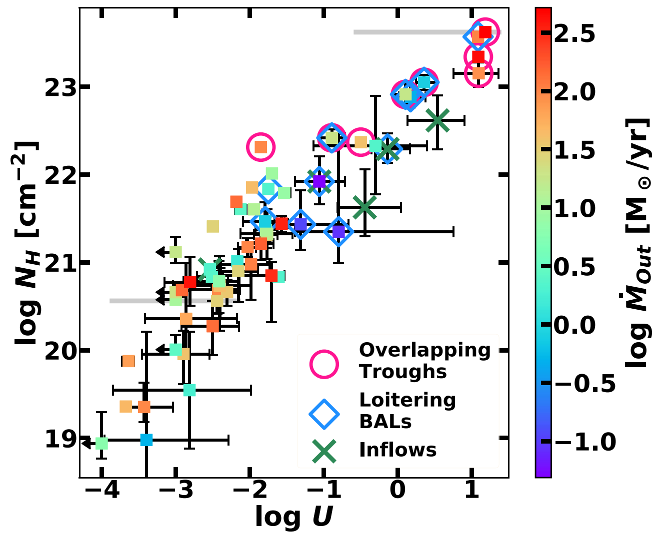

Figure 7. The BALs with high log U have larger covering-fraction-corrected hydrogen column densities. The strong correlation between the two parameters is expected for FeLoBALs that require the gas column densities to be high enough to reach the hydrogen ionization front (log N_H − log U ∼ 23 [cm^{-2}]). Markers and error bars as in Figure 4.

$L_{\rm KE}$ of an outflow is proportional to v^3 , which explains the tight correlation between $L_{\rm KE}$ and $v_{\rm off}$ observed in our sample of FeLoBALs. All the outflows with the highest outflow velocities (8 out of 55 FeLoBALs with $v_{\rm off} \lesssim -2400$ km s^{-1}) in our sample have enough energy to produce quasar feedback (Section 7.4). While many of these powerful outflows with high velocities are located near the vicinity of torus log $R \leqslant 1$ [pc], we did not find robust evidence suggesting a connection between log R and $L_{\rm KE}$ (Section 6.1). This lack of correlations suggests that the outflow strength or the outflow's role in quasar feedback is mainly determined by the outflow velocity and the physical properties of the gas. In other words, where the outflows are located at present does not have significant influence on the inferred energetics of the outflows.

6. Analysis of the Full Sample

6.1. Correlations

In order to systematically study the relationship between the physical and kinematic properties of FeLoBALs and the derived-wind properties, we calculated the Kendall rank correlation coefficients for all pairs of the measured quantities

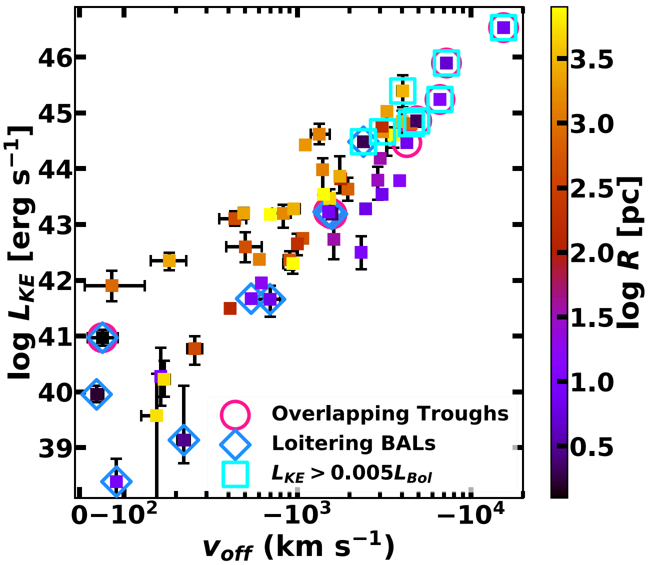

Figure 8. The kinetic luminosities ($L_{\rm KE}$) of the FeLoBAL outflows scale with the outflow velocities with the slope of ∼3. This relationship is expected from the definition of $L_{\rm KE}$. The scatter in the $L_{\rm KE}$ direction can be mainly ascribed to the range of mass outflow rate ($\dot{M}$) of the outflows as well as gas physical conditions such as covering-fraction-corrected hydrogen column densities. The colors of the markers represent the locations of the outflows ($\log R$), and for an FeLoBAL outflow at a given outflow velocity, larger $\log R$ will yield larger $\dot{M}$ and greater $L_{\rm KE}$. We did not find any particular trend with $\log R$ and the properties plotted in the figure; however, the outflows with the highest velocities in our sample were all found to be within the vicinity of torus $\log R \lesssim 1$ [pc]. The 5 BALs with inflows are not plotted.

and examined the ones that showed significant correlations ($p < 0.01$). Because we have BALs with upper or lower limits of $\log n$ or $\log U$, we used `pymccorrelation` by Privon et al. (2020)[11], which provides a python implementation of Kendall's tau rank correlation coefficient calculator for censored data (Isobe et al. 1986). Only the values from the BALs from the outflowing gas ($v_{\rm off} < 0$ km s^{-1}) were used for the correlation analysis with outflow properties ($\dot{M}_{\rm out}$, $L_{\rm KE}$). The results are shown in Figure 9.

6.1.1. Outflow Physical Properties

Among the fit parameters that were directly constrained from the models, we found correlations between $\log n$ and $\log U$ and $\log N_H - \log U$ for gas physical properties, and between $v_{\rm off}$ and $v_{\rm width}$ for gas dynamical parameters. The correlations with $\log n$ suggest that, for the FeLoBALs in our sample, the gas with higher density also tends to be more highly ionized and thicker with a higher column density. The covering-fraction parameter $\log a$ was also highly correlated with $\log U$. The correlations between $\log U$, $\log n$, and $\log a$ were seen on the right panel of Figure 4 where the BALs with higher $\log U$ were found to be denser with lower partial-covering (higher $\log n$ and $\log a$). As we discussed in Section 5.2, the correlation between the partial-covering parameter $\log a$ and the ionization parameter may be due to a selection effect: FeLoBALs with high $\log U$ and low $\log a$ (large covering) are unlikely to be detected due to heavy absorption. We only observe high-$\log U$ outflows that have high $\log a$ (i.e., not completely covered).

While we also found that $\log U$ shows correlations with both $\log R$ and $\log N_H$, we interpret these correlations mainly arising from a selection effect (Section 5.3). $\log R$ is calculated using the definition of $\log U$: $R \propto (Q/nU)^{1/2}$ (Section 4.2). For the range of number of photoionizing photons per second emitted from the AGN, Q, this sample only spans about a dex for the FeLoBAL quasars; therefore we can expect $\log R$ to be negatively correlated with both $\log U$ and $\log n$, as found. Similarly, the correlation that we observe between $\log U$ and $\log N_H$ (partial-covering-corrected column density) is expected for an FeLoBAL sample because FeLoBALs require the outflow gas to be thick enough to reach the hydrogen ionization front $\log N_H - \log U \sim 23.0$ [cm^{-2}] (Section 5.3).

A negative correlation between velocity offset and velocity width is seen in the right panel of Figure 5 (as well as with the correlation coefficient). The FeLoBAL outflows in our sample show a near one-to-one correlation between the two velocity parameters, which indicates that FeLoBAL features are seldom seen as detached troughs; the absorption starts from rest. We can also see from the p-value and the correlation coefficient that there is a weak positive correlation between $\log n$ and $v_{\rm width}$ but not with $v_{\rm off}$. Although the statistical test suggests that there exists a correlation between these parameters in our sample of low-redshift FeLoBALQs, we cannot confidently conclude whether they represent a true global trend in the parameter space. We will need to analyze a larger homogeneous sample of FeLoBALQs in order to substantiate this result.

The parameters that measure the strength of the outflow ($\dot{M}_{\rm out}$, $L_{\rm KE}$) showed strong correlations with BAL velocity offset. As discussed in Section 5.2, it is expected for $\dot{M}_{\rm out}$ and $L_{\rm KE}$ to be strongly dependent on $v_{\rm off}$. The correlation analysis from our FeLoBALs further supports the relationship between the two properties and also suggests that the dependence of $\dot{M}_{\rm out}$ and $L_{\rm KE}$ on the dynamics of the gas ($v_{\rm off}$) is so strong that the physical properties of the gas (e.g., $\log U$, $\log N_H - \log U$) do not significantly influence the energetics of the BAL outflow or the outflow's potential impact on the host galaxy. We did not observe any significant correlations between $L_{\rm KE}$ and other parameters used to calculate this value ($\log R$ or $\log N_H$), again emphasizing its strong dependence on velocity above all other parameters (Figure 8).

6.1.2. Quasar Properties

In addition to the BAL properties, we also investigated potential connections between the outflows and the properties of the quasars. The quasar properties (e.g., $L_{\rm Bol}$) were measured using the observation data and *SimBAL* modeling (Section 4.1).

We found a strong positive correlation between the velocity offset and the bolometric luminosity of the quasar ($L_{\rm Bol}$). Our result is consistent with previous studies that found that quasars with higher $L_{\rm Bol}$ have outflows with higher velocities (e.g., Laor & Brandt 2002; Ganguly et al. 2007; Fiore et al. 2017). The outflow velocity is expected to depend on the bolometric luminosity normalized by the Eddington value ($L_{\rm Bol}/L_{Edd}$) for radiatively driven quasar winds. We explore this correlation in Paper III (Choi et al. 2022) using the objects that have black hole mass measurements from the rest-optical emission-lines (Leighly et al. 2022). Because the velocity offset determines the strength of the outflow, we found a positive correlation between $L_{\rm Bol}$ and $L_{\rm KE}$; the more luminous quasars tend to have faster and more energetic outflows.

---

[11] https://github.com/privong/pymccorrelation/

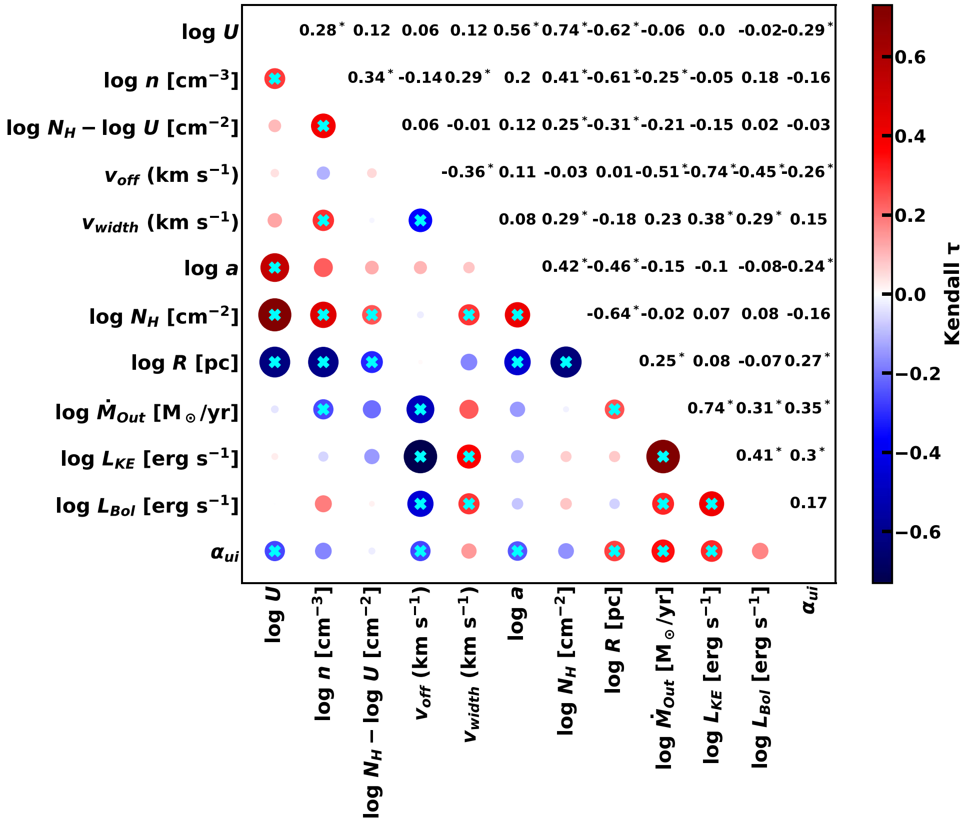

Figure 9. The correlation coefficients calculated for all measured-BAL property pairs. The size and the color of the markers reflect the values of Kendall's rank correlation coefficient. The values with asterisks and cyan crosses represent the pairs that showed statistically significant correlations ($p < 0.01$). The first six parameters ($\log U$, $\log n$, $\log N_H - \log U$, $v_{\rm off}$, $v_{\rm width}$, and $\log a$) are the best-fitting model parameters from *SimBAL*, and the rest are the derived properties calculated from the model parameters.

We found that α_{ui} is strongly correlated with $\log R$ and $v_{outflow}$ ($v_{\rm off}$). Quasars with flatter SEDs ($\alpha_{ui} \gtrsim -0.5$) have redder colors and have faster and thus more powerful outflows. The quasars with steeper or bluer SEDs ($\alpha_{ui} \lesssim -0.5$) have FeLoBALs that are located closer to the central engine (smaller $\log R$) that are more ionized (higher $\log U$), and they tend to have smaller outflow velocities. Most of these compact, low-velocity FeLoBALs are loitering BALs that do not show the properties expected for typical quasar-driven winds. We further discuss the properties of these FeLoBALs in Section 6.5.

Our result seems somewhat similar with what have been found in extremely red quasars (ERQs). These objects show a higher incidence of outflow signatures in [O III]$\lambda\lambda$4959, 5007 emission lines than typical blue quasars, and a correlation between the outflow speeds and the redness of the SED has been found (Hamann et al. 2017; Perrotta et al. 2019). We note, however, that the FeLoBALQs in our sample are not ERQs, and the quasar winds seen in emission lines can exhibit different properties than the BAL winds. We discuss the implications of the SED color on the acceleration mechanism of the BAL outflows in Section 7.2.

In summary, the only physically significant correlations that we found from the FeLoBAL and quasar properties were between $L_{\rm Bol}$ and $v_{\rm off}$, which propagates because of the functional dependence to $\dot{M}_{\rm out}$ and $L_{\rm KE}$. We also found correlations with α_{ui} where FeLoBALs found in objects with flatter (redder) spectral slope have larger $\log R$ and $L_{\rm KE}$.

6.2. Objects with Multiple FeLoBAL Outflows

We identified more than one outflow component in nine objects (excluding the broad Mg II component in SDSS J1214−0001 and the extra component in SDSS J1644−5307 only seen in Mg II; see Section 5.1 and Appendix C). While three of the nine objects showed several troughs distinctly separated by velocity, the others required a rigorous modeling with *SimBAL* to identify multiple outflows in blended troughs.

Figures 10 and 11 show the two groups of objects with more than one BAL component. The three objects in the first group have more than one narrow Mg II trough that are separated by velocity (e.g., SDSS J1044+3656 in Figure 10). In these objects, the differences in the gas physical parameters were not extreme, and the estimated distances for the BALs only differ by a moderate amount (Figure 12). In the second group (Figure 11), the features are blended. *SimBAL* analysis identified multiple components, and large differences in the gas properties, especially $\log U$, were found (Figure 12). The difference in $\log U$ resulted in large differences in $\log R$. The BAL components with higher $\log U$ include a plethora of absorption line transitions including the rare transitions from the excited-state ions, but due to the large $\log a$ (low covering fraction), the depth of these troughs is small. These particular components played a critical role in creating the overlapping-trough features because they provided excited-state Fe II transitions around ∼2500 Å (i.e., between the ground-state multiplet features near ∼2400 Å and ∼2600 Å) as well as the absorption lines observed longward of ∼2800 Å (Section 6.4; see also Lucy et al. 2014).

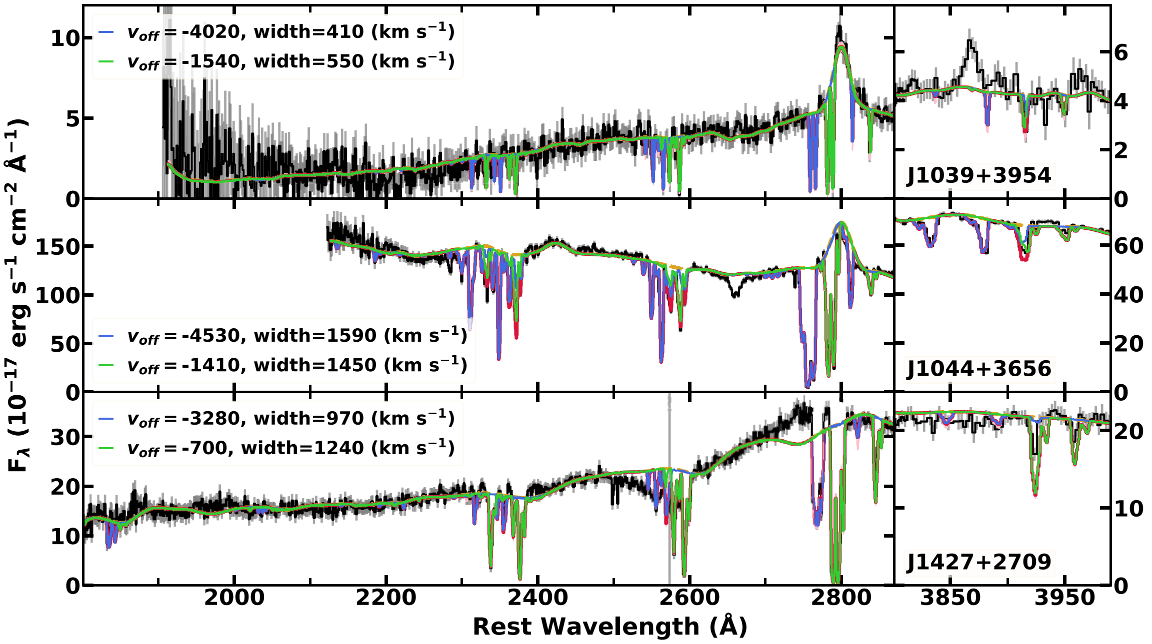

Figure 10. Objects that show multiple outflows where each BAL component (indicated with blue and green model curves) is clearly separated (Mg II$\lambda\lambda$2796,2803 troughs are not blended, left column). The data (error) is plotted in black (gray), and the best-fitting model is shown in red with the BAL components overplotted in green and blue. The column on the right shows the wavelength region where He I*, Ca II H, and K absorption lines are found. Note the BALs in these objects have low ionization, and no He I* absorption-lines are observed.

The higher-velocity components in the multiple-outflow objects have higher $\log U$ and lower covering fraction compared with the lower-velocity component (e.g., SDSS J1020+6023 in Figure 11; Figure 12). They produced opacity from both the excited-state and the ground-state Fe II transitions. In contrast, the lower-velocity components produced higher opacity overall from the ground-state Fe II and Mg II only and were responsible for the most of the strong Mg II absorption features observed in the spectra. Choi et al. (2020) and Leighly et al. (2018) both observed a similar trend where they found higher-ionization parameter and lower covering fraction for the tophat bins with higher velocities in the best-fitting *SimBAL* models. The distinct gas properties constrain the location to different radii: the higher-velocity component is found much closer to the SMBHs than the lower-velocity component in a given object.

The FeLoBALQs with multiple blended components show some of the most extreme spectral features, such as overlapping troughs (e.g., SDSS J1556+3517 in Figure 11). However, the BAL component decomposition revealed that the lower-velocity components in these objects actually resemble a typical FeLoBAL. In other words, without the higher-velocity components, these FeLoBALQs would show spectra that are indistinguishable from those of the moderately absorbed FeLoBALQs with low- to moderate-ionization parameter (Section 5.2.1). Because of the difference in location, we expect the dynamic timescales between the higher-velocity components and the lower-velocity components would be dramatically different, with the higher-velocity components expected to have much shorter timescales. It is plausible that these higher-velocity components at $\log R \lesssim 1$ [pc] may represent a a transient phenomenon. For example, the objects that have overlapping-trough features originating from higher-velocity components may show BAL variability in which the overlapping trough disappears to reveal spectra that look like typical FeLoBALQs. Such variability has been seen in a number of FeLoBAL quasars (e.g., Rafiee et al. 2016).

There could be many origins of the lower-velocity components for the multicomponent objects. *SimBAL* modeling assumes that these multiple components are not physically related (i.e., independent photoionization modeling for each absorber). Because the BAL components in a given multi-BAL FeLoBALQ are separated by a large radial distance, it is unlikely that they are physically related and formed in the same gas. One possibility is that the lower-velocity components might represent the remnants from earlier ejection episodes that are located along the line of sight (e.g., Choi et al. 2020). A variability study of these objects could potentially give us a more detailed picture of the geometry of the multi-BAL system. For instance, we may expect a systematically different variability pattern between the two absorbers if we assume the two gas clouds are not physically related (e.g., Leighly et al. 2015).

Nevertheless, it is possible that the multiple absorbers in a given object may be related in terms of their photoionization processes. Voit et al. (1993) proposed structures in outflowing gas cloudlets that can produce BALs with stratified ionization conditions based on the observations of high-ionization BALs (C IV $\lambda\lambda$1548, 1550) and low-ionization BALs (e.g., Mg II $\lambda\lambda$2796, 2803). In their models, the highly ionized condition can be formed in the higher-velocity portion of the BAL gas clumps, and the lower-ionization environment is found near the lower-velocity end, similar to how we found higher-velocity components with higher ionization. If the multiple components found in a given object are physically related and their photoionization processes are interdependent, it would be conceivable that we may be overestimating the distances between the lower-velocity BALs and the higher-velocity BALs. In such scenario, a single absorbing gas may be able to produce multiple components with different ionization states;

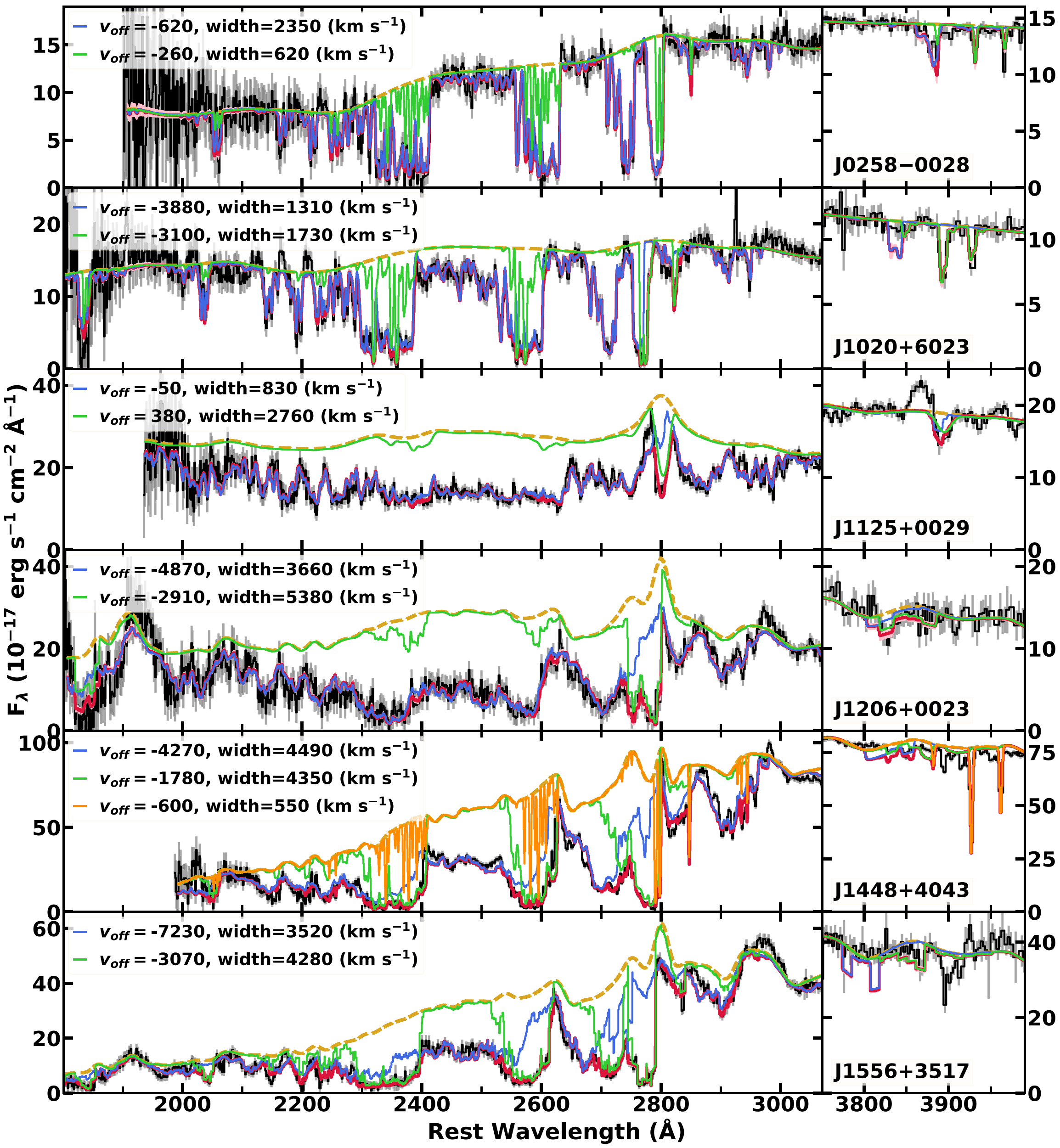

Figure 11. Objects that have multiple blended BAL components. The differences in gas physical properties can be observed most clearly with Ca II H and K lines where these absorption lines are only found the lower-velocity components with lower log U and log n (right column). For example, we found three BAL components in SDSS J1448+4043 with the lowest-velocity component showing deep Mg I absorption line as well as Ca II H and K absorption lines (plotted in orange). The data (error) is plotted in black (gray), and the best-fitting model is shown in red with the BAL components are overplotted in green and blue with the continuum plotted in dashed tan lines.

however, *SimBAL* neither has grids nor performs the dynamical photoionization modeling needed to reproduce such physical conditions. Furthermore, the objects in our current sample have too low redshift to observe the C IV lines that we need to investigate such scenario; therefore we do not have robust observational evidence supporting a complex ionization structure in absorbing gas. We will investigate this question using a sample of higher-redshift FeLoBALQs.

A third possibility is that the lower-velocity gas may originate from more distant structures in the quasar system. At the distances calculated from the gas properties (10s–1000s pc), the molecular clouds in the host galaxy could be the source for the material illuminated by the quasar (e.g., Faucher-Giguère et al. 2012).

6.3. Opacity Profiles of the Outflows

6.3.1. Mg II and Fe II Absorption Lines

Comparing the opacity profiles between line transitions from the ions that have different properties can potentially tell us about the structure of the BAL winds. For instance, Voit et al. (1993) proposed a schematic picture of BAL clouds based on the differences in the opacity profiles between the high-ionization lines (e.g., C IV) and the low-ionization lines (e.g., Mg II). They suggested that the BALs originate from a turbulent absorbing region, and the absorbing gas clouds may have structures with dense cores with inhomogeneous photoionization conditions.

We found evidence for gas structure in the profiles in our sample. Although most of the FeLoBALs were modeled with a

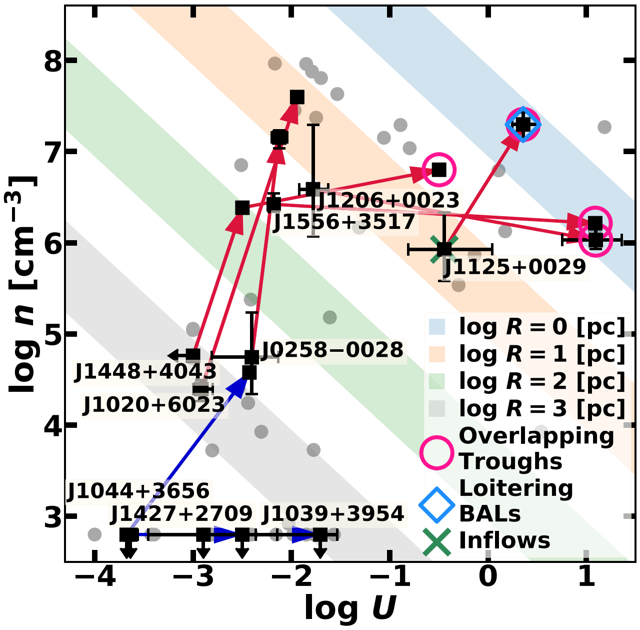

Figure 12. The outflows from the objects that have more than one FeLoBAL feature are plotted with squares, and the rest of the outflows shown by gray dots. The arrows start from the lower-velocity component and end at the higher-velocity component in the same object. Blue and red arrows (labeled by object) represent objects shown in Figures 10 and 11, respectively. The shaded diagonal bars for log R were calculated using the typical range of photoionizing photon flux found in our sample of FeLoBALQs ($\log Q \sim 55.5$–56.5 [photons s^{-1}]). All of the higher-velocity components have higher-ionization parameter, and the majority of them have higher density compared to the lower-velocity components in the same object. Thus the higher-velocity components are located closer to the central black hole. Four of the higher-velocity components with significantly higher log U are overlapping-trough BALs. The error bars show 2σ (95.45%) uncertainties.

single ionization parameter and a single density (Section 5.1), we found dramatic changes in column density and covering fraction across the BAL velocity profile. Two of the I/I_0 models for SDSS J0840+3633 and SDSS J1527+5912 are shown in Figure 13. These models show remarkable differences between the profiles of the Fe II and Mg II lines that are caused by a change in both $\log N_H - \log U$ and $\log a$ across the trough. In particular, the excited-state Fe II opacity profile for SDSS J0840+3633 has a prominent double-peak structure with lower apparent opacity in the center that is not obvious in the opacity profile of the Mg II. The I/I_0 model for SDSS J1527+5912 shows the presence of a high-column-density core at the lower-velocity end of the profile; therefore, we observe a narrower width for Fe II. This BAL has low density ($\log n \sim 4.7$ [cm^{-3}]), and the excited-state Fe II transition is not observed.

Figure 14 shows that the BAL widths measured from Fe II transitions are generally smaller or similar to those measured from Mg II. The widths of the excited-state Fe II transitions were significantly smaller than the widths of the ground-state Fe II and Mg II. Since a higher column density is required to accumulate significant opacity in excited-state Fe II*, this means that the trough column density is not constant with velocity. In other words, the differences in widths can be ascribed to the intrinsic inhomogeneous physical structure of BAL gas, such as change in $\log N_H - \log U$ across the BAL troughs. For example, the model for SDSS J1527+5912 show a significantly wider profile in Mg II than in the ground-state Fe II because the bins at higher velocities show a drop in $\log N_H - \log U$ (below the hydrogen ionization front at $\log N_H - \log U \sim 23$ [cm^{-2}]), and thus they do not produce opacity from Fe II. BALs identified with substantially larger Mg II widths than the Fe II widths showed extended low $\log N_H - \log U$ structure where the bins at the lowest and highest ends in velocity only produced Mg II opacity. Similarly the opacity from the excited-state Fe II only appeared in the bins with high $\log N_H - \log U$, and oftentimes these high-opacity concentrations or *cores* were only found in a small subset of bins for a given BAL component.

In addition to the change in column density, the covering fraction also varies with velocity, and the combination of the two can change the relative widths of these lines. For saturated lines, the line depths and shapes are mostly controlled by the partial-covering. *SimBAL* takes both of the effects into consideration when using tophat accordion models to fit the spectra. For example, in Figure 13, both $\log N_H - \log U$ and $\log a$ change significantly across the trough, and as a result, we observe a sawtooth-shaped line profile in excited-state Fe II in the I/I_0 model for SDSS J0840+3633.

We measured the offset velocities for all three transitions separately (Section 4.3) using the I/I_0 models, and they showed no systematic difference from the summary outflow velocities that we calculated from the distributions of intrinsic opacity for each BAL (Section 4.2). This result shows that our definition of summary outflow velocities is not biased against any particular transition, and in general, where the intrinsic opacity is high, the maximum of the apparent opacity is also high despite partial-covering heavily influencing the apparent line and opacity profiles.

Voit et al. (1993) found that the low-ionization lines such as Mg II and Al III are typically only located at the low-velocity ends of the BAL troughs with narrow line profiles whereas high-ionization lines C IV appear in a wider-velocity range extending to much higher velocity showing much broader line profiles. They concluded that nonmonotonic acceleration or deceleration of outflow gas scenarios can explain such velocity structures. Although we found that physical properties change across the BAL troughs and thus the opacity profiles for different transitions may show completely different shapes for a given BAL component, we did not find robust systematic trends between the profiles of Mg II, Fe II, and Fe II*. Future work with a sample of high-redshift FeLoBALQs will allow us to study the absorption line profiles of C IV using SDSS spectra, and we will be able to examine how their line profiles differ from the low-ionization lines and to investigate the potential ionization structure in BAL absorbing clouds.

Trends in the absorption-line structure hold promise for illuminating the nature of the acceleration mechanisms or gas cloud structure as a function of radial position in the quasar. To explore this possibility, we created composite I/I_0 profiles for subsamples with similar ionization and radial location for the outflowing gas. Specifically, we grouped the BALs into three groups using log U values: 16 low-opacity BALs with low log U that have lower limits on log R estimates (due to upper limits on log n constraints); 28 intermediate-opacity BALs with $\log U < -1.5$ that have well-constrained log R (and log n); 16 high-opacity BALs with $\log U > -1.5$. The median log U for the three groups are −2.66, −2.24, and −0.02. Because there is a strong correlation between log R and log U (Sections 5.3, 6.1), these groups also showed clear differences in log R properties: the median log R for the low −log U, intermediate-

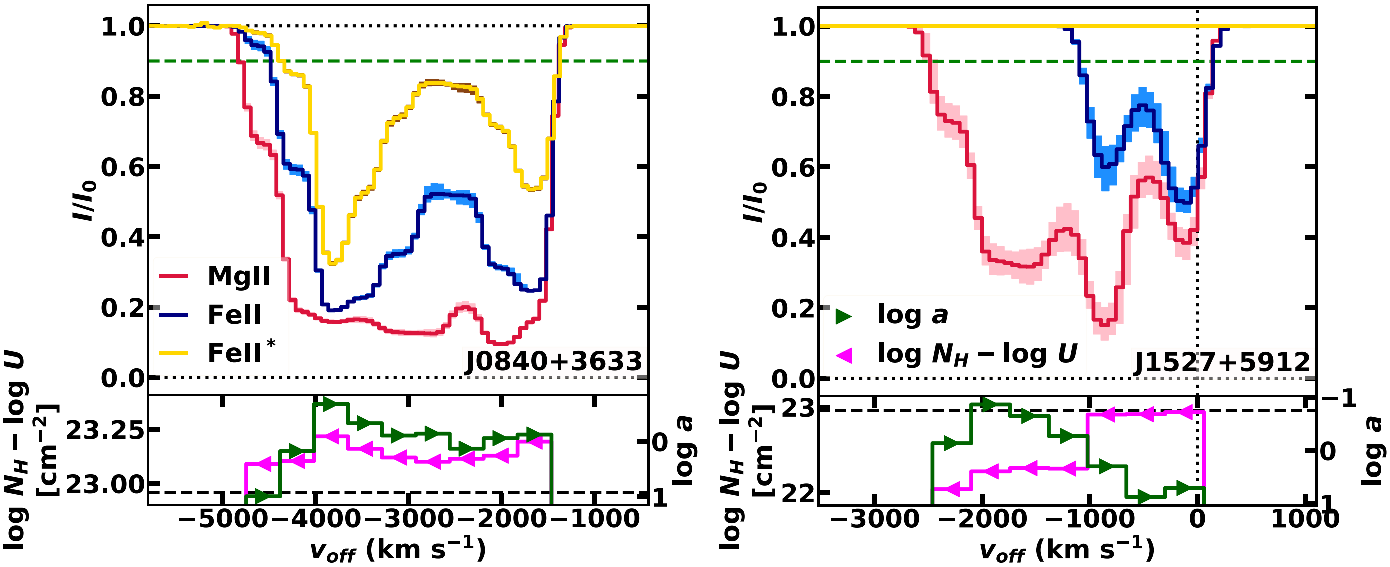

Figure 13. The top panels show normalized spectrum (I/I_0) models for three line transitions (Mg IIλ 2796, Fe IIλ 2383, and Fe II$^*\lambda$ 2757) from SDSS J0840+3633 and SDSS J1527+5912. The lighter shaded regions around each model represent 2σ (95.45%) uncertainties. In the bottom panels, the column density parameter ($\log N_H - \log U$) and the covering fraction parameter ($\log a$) as a function of velocity are plotted in pink and green, respectively. The complete figure with I/I_0 models from all 60 BALs is available in the online journal.

(The complete figure set (30 images) is available.)

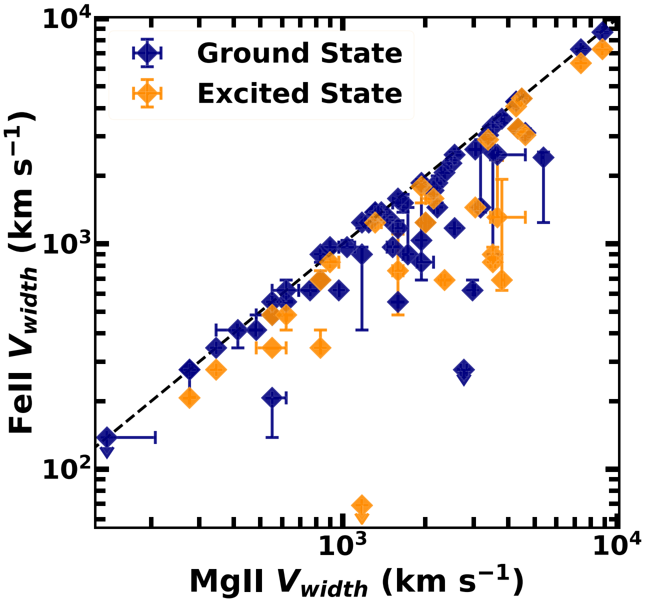

Figure 14. The width measurements from different line transitions are plotted with 2σ (95.45%) error bars. The widths measured with the excited-state Fe II are noticeably smaller than the widths measured from the Mg II or the ground-state Fe II transitions. Objects with the excited-state Fe II transition are plotted with orange diamonds.

log U, and high-log U BAL group are 3.45, 2.24, and 0.63 [pc], respectively. The three groups represent (1) distant, low-ionization BALs with kiloparsec-scale winds, (2) intermediate-scale medium ionization BALs, and (3) compact high-ionization BALs that are located within ∼10 pc from the central engine with size-scales comparable to the torus scale. The I/I_0 models for each BAL component were normalized with respect to their maximum offset velocity where in the new normalized $v_{\rm off}$ axis −1 (or 1 for $v_{\rm off} > 0$) represents the maximum velocity measured from the I/I_0 models (a similar parameterization can be found in Borguet & Hutsemékers 2010). We then median combined the I/I_0 models and calculated the median absolute deviation. Figure 15 shows the composite I/I_0 model spectra from the three BAL groups.

The composite I/I_0 models showed large differences in the line depths of Mg IIλ 2796 and the excited-state Fe II$^*\lambda$ 2757. Noting that log U is correlated with log n and log a, we expect the BALs in the low-log R BAL group with high log U to also have higher log n and log a (less covering) as observed. The high log a (less covering) makes all the line transitions appear shallow, which is why the line depth of Mg II is the smallest in the composite for the small −log R group. On the other hand, the higher value of log n can populate the excited-state Fe II ions in the gas and create strong excited-state Fe II absorption lines, so we see the deepest excited-state Fe II line profile compared to the other composites. The composite for the low-log U group with distant winds shows no opacity from the excited-state Fe II. While the differences in the line depths seen in the composites for different log R can be unambiguously explained by the differences in the physical properties, we did not find robust evidence for a systematic difference in gas structures or opacity profiles between the composite I/I_0 models. We may expect to find a more definitive answer with the composite I/I_0 models from a larger sample; however, the large dispersion (median absolute deviation) seen in Figure 15 suggests that the line profiles depend more strongly on the individual physical conditions of each FeLoBALs than any global trend. We also expect larger differences between the low-ionization lines considered here, and high-ionization lines such as C IV$\lambda\lambda$1549,1551.

6.3.2. Ca II, He I*, and Balmer Absorption Lines

Ca II H and K, He I$^*\lambda$ 3889, and Balmer absorption lines found in the rest-optical wavelengths can provide crucial

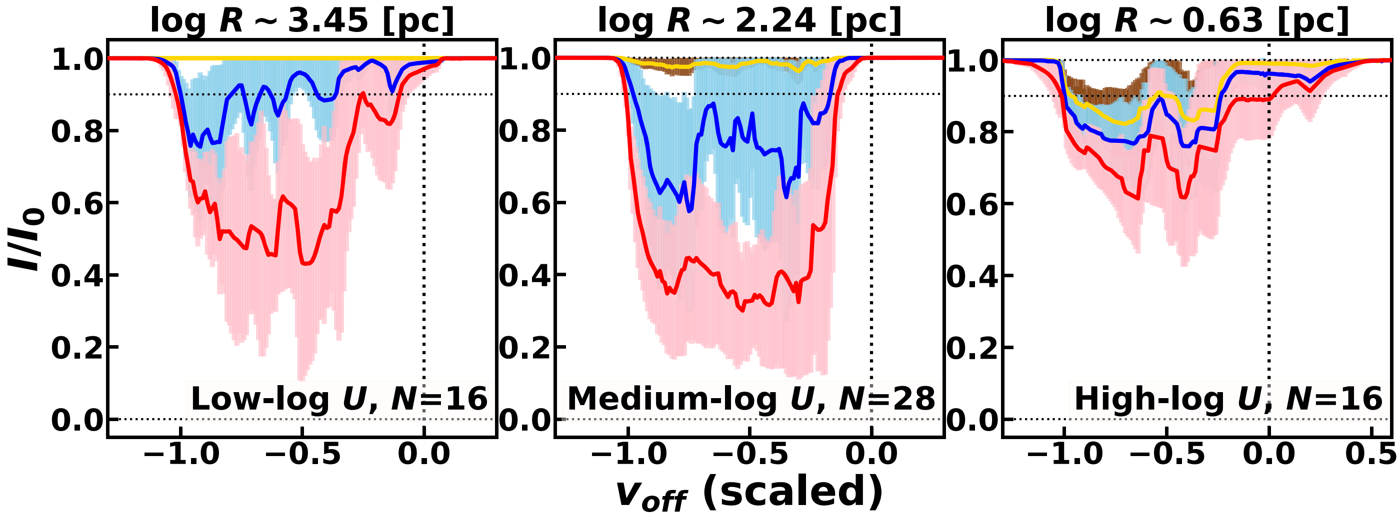

Figure 15. The three composite I/I_0 model spectra are plotted. The left panel shows the median composite I/I_0 model spectrum for the low $-\log U$ BALs, and the middle and the right panels show the same model for the medium $-\log U$ BALs and high-log U BALs, respectively. The median log R for each group is noted above each panel. The numbers of BAL components used to generate each composite are also noted. The Mg II λ 2796, Fe II λ 2383, and Fe II* λ 2757 transition models are plotted in red, blue, and yellow, respectively. The pink, light blue, and brown shaded areas represent the median absolute deviation for the Mg II λ 2796, Fe II λ 2383, and Fe II* λ 2757 transitions, respectively. The normalized $v_{\rm off}$ was used on the x-axis where 0 represents $v_{\rm off} = 0$ km s^{-1}, and −1 (or 1 for $v_{\rm off} > 0$) represents the maximum BAL velocity measured for each I/I_0 model.

information about the physical properties of the outflowing gas. Leighly et al. (2014) analyzed Ca II, Na I, and He I* absorption lines observed in the optical spectrum of the nearby Seyfert 1 object Mrk 231 to discover evidence for an interaction between a quasar outflow and the surrounding the interstellar medium (ISM). Leighly et al. (2011) discussed the advantages of using He I* λ 3889 absorption line to study BAL winds that have high column densities. The density of the BAL gas needs to be high ($\log n \gtrsim 7$) in order to produce an observable amount of opacity from Balmer transitions (e.g., Leighly et al. 2011). Therefore, Balmer absorption lines can be used as diagnostics to detect the compact BAL winds (small log R) with high densities.

We found that many of our FeLoBALQs show Ca II, He I*, and Balmer absorption lines in the spectra. The best-fit models provided excellent fit both for the main Fe II and Mg II troughs and for the rest-optical absorption lines as well (Figure 1; 10; 11). In contrast, previous BAL studies only found a small number of (FeLo)BALQs with Ca II BAL features (e.g., Boksenberg et al. 1977; Arav et al. 2001; Hall et al. 2003). Moreover, Balmer absorption lines have been observed in only a small number of FeLoBALQs (e.g., Hall 2007; Shi et al. 2016; Schulze et al. 2018). That is maybe because there has been no systematic study of FeLoBALQs prior to this work. We investigated how these rest-optical absorption lines are related to the FeLoBAL winds and what information about outflows we can gain from analyzing these transitions.

Out of 60 BAL components analyzed, we found 26, 40, and 18 BAL components are predicted to show opacity from Ca II H, K, He I* λ 3889, and Balmer transitions, respectively. Because our sample contains a wide range of redshifts ($0.66 < z < 1.63$), not all SDSS/BOSS spectra that we analyzed included these transitions in the bandpass. Therefore, we had to extrapolate the best-fitting models to longer wavelengths to calculate the absorption strengths for some of the BALs. Figure 16 shows the distributions of the absorption strength predicted by the models (Section 4.3) along the log U and log R axes.

The opacity from Balmer transitions is only found in BALs with $\log R \lesssim 1$ [pc]. In other words, we suggest that the presence of Balmer absorption lines can be used as an indicator for compact BAL winds. In contrast, only the kiloparsec-scale BAL winds showed opacity from Ca II. This is expected given that the distant BALs have low log U and low log n (Figure 4), the physical conditions required to create Ca$^+$ ions. However, in a few cases, Ca II BALs were observed with other high-log U or high $-\log n$ absorption lines at similar velocities (e.g., He I*, excited-state Fe II), and therefore these Ca II outflows likely lie at small radii ($\log R \ll$ kpc) and have unusual physical conditions. For instance, Leighly et al. (2014) inferred a density increase at the hydrogen ionization front to explain Na ID absorption in Mrk 231. Hall et al. (2002) suggested a significant gas temperature change to explain the Ca II absorption lines observed in SDSS J0300+0048. The opacity from He I* was found in the majority of FeLoBALs over a wide range of log R. This result is consistent with what has been reported by Liu et al. (2015) where they also found a large fraction of Mg II selected LoBALQs with He I* absorption lines observed in the spectra. The presence of He I* absorption lines in (Fe)LoBALQs is a direct consequence of the absorbing gas having a high enough column density to produce observable low-ionization absorption lines such as Mg II (Fe II).

In summary, the absorption lines from Ca II, He I*, and Balmer transitions observed and predicted in rest-optical spectra of FeLoBALQs provide us with critical information about the physical properties. In particular, the presence of Ca II or Balmer absorption lines can be used to estimate the size scales of the BAL outflows, and the He I* absorption line can be used to identify (Fe)LoBALs. This shows that, even without a detailed photoionization modeling of rest-UV (FeLo)BALQ spectrum, one could potentially predict the approximate outflow spectral properties from the rest-optical spectrum.

6.4. Overlapping-trough FeLoBALs

Overlapping troughs show magnificent absorption features in the rest-UV spectra where the continuum emission is often

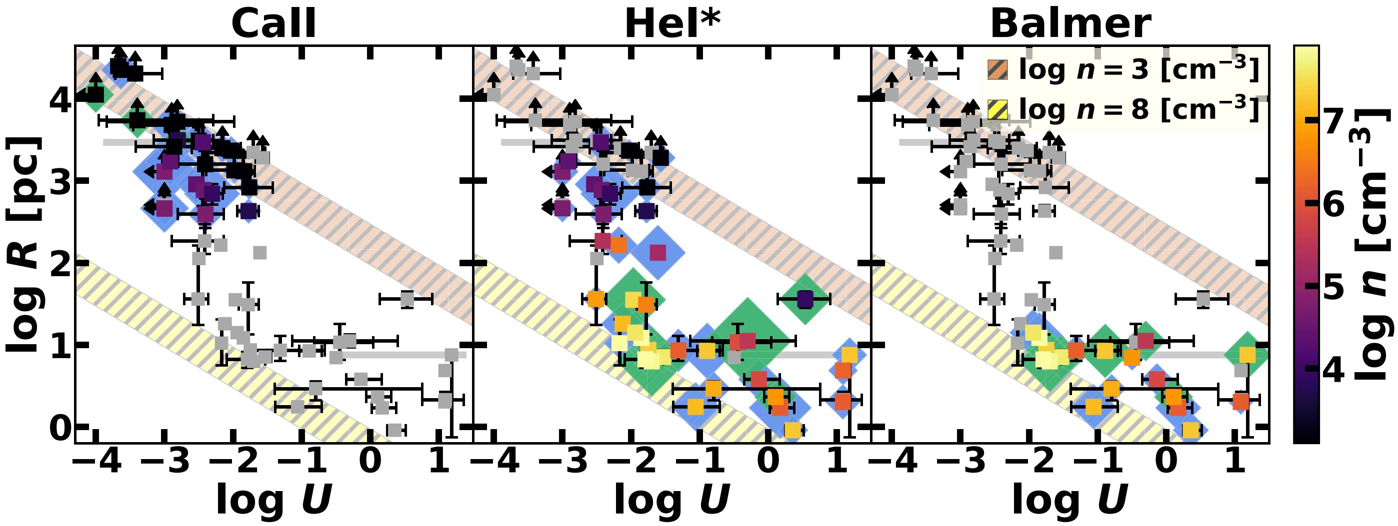

Figure 16. Figure 6 modified to show the distributions of absorption strengths (Section 4.3) of select line transitions predicted using the I/I_0 models. Our results point toward the presence of specific absorption lines as being key diagnostics for the location of the outflow (R). The blue diamonds represent the absorption strengths calculated from best-fitting models. The absorption strengths represented with green diamonds were calculated from the extrapolated *SimBAL* models (see text). The gray squares represent the BAL components that are not predicted, showing any opacity from the line transition featured in each panel. The size of the diamonds is proportional to values of the absorption strength parameter (i.e., larger markers represent stronger absorption). The Ca II absorption lines are only found in distant BALs ($\log R \gtrsim 3$ [pc]), and Balmer absorption lines are found in BALs with $\log R \lesssim 1$ [pc]. He I* absorption lines are predicted and found in nearly all FeLoBALs. The error bars show 2σ (95.45%) uncertainties, and the gray shaded bars represent the range of the values among the tophat model bins for each BAL.

nearly completely absorbed between $\lambda \sim 2000$ Å and $\lambda \sim 2800$ Å by a multitude of Fe II absorption lines. Hall et al. (2002) introduced several objects with overlapping troughs and discussed their spectral features; however, in-depth analysis of overlapping-trough BALs has not been possible with conventional methods (e.g., measuring ionic column densities from the individual line profiles) due to extreme line blending. *SimBAL* can be used to analyze spectra with overlapping troughs, as demonstrated in SDSS J1352+4239, a heavily absorbed overlapping-trough object (Choi et al. 2020).

The term “overlapping trough” has been used differently by different authors (e.g., Hall et al. 2002; Meusinger et al. 2016). In the literature, overlapping-trough objects generally refer to the FeLoBALQs with very broad absorption features reaching near-zero flux at the bottom, following the more stringent criteria introduced by Hall et al. (2002). We used a modified criterion to identify overlapping troughs that is based only on BAL morphology: such BALs were identified based on whether the continuum emission at $\lambda \sim 2500$ Å (outflow reference frame) where the absorption lines from the excited-state Fe II are expected to appear in the spectrum is heavily absorbed or not. This method allowed us to focus only on the morphology of the troughs and identify all extremely wide troughs regardless of the amount of partial-covering or the continuum shape.

Figure 17 shows the eight objects with overlapping troughs that we found in our sample as well as SDSS J1352+4239 (Choi et al. 2020). We observe a great diversity in spectral morphology and gas kinematics as well as outflow gas properties. Their broad troughs have been fit with tophat models, and five objects (SDSS J0300+0048, SDSS J1154+0300, SDSS J1556+3517, SDSS J1206+0023, SDSS J1448+4043) required the use of general reddening (Choi et al. 2020) to model the anomalous reddening. Three out of the eight objects (SDSS J1019+0225, SDSS J1125+0029, SDSS J1644+5307) also required additional unabsorbed components underneath the troughs (Section 5.1.1). A similar plot can be found in Figure 12 of Lucy et al. (2014) where they show different spectral morphologies of FeLoBALs with narrower lines.

Although the significant absorption seen in overlapping troughs indicates high-opacity and high-column-density gas, this feature does not necessarily mean that the overlapping-trough BALs have high kinetic luminosities ($L_{\rm KE}$). The wide range of outflow velocities seen in the overlapping-trough BALs (marked by the lengths of the arrows in Figure 17) shows that some of them have no significant outflow velocity and thus are not carrying any significant mass or energy in the wind. As shown in Section 6.1, the most important factor in determining the kinetic luminosity of an outflow is the outflow velocity. Thus, we found that five objects have overlapping-trough BALs that are powerful outflows with $|v_{\rm off}| > 4000\ {\rm km\ s^{-1}}$ and $L_{\rm KE}/L_{\rm Bol} > 0.5\%$. These five objects also show blended troughs reaching near-zero flux at the bottom and can be called overlapping-trough objects based on the classification criteria by Hall et al. (2002). They are further distinguished by the presence of anomalous reddening (e.g., Choi et al. 2020). The other three objects, represented in the third column in Figure 17, have outflows with low velocities ($|v_{\rm off}| < 1600\ {\rm km\ s^{-1}}$) thus do not have the high $L_{\rm KE}$ required for the quasar feedback.

In contrast to the wide range of outflow velocities found in the overlapping-trough BALs, all of these outflows were found at similar distances from the central engine ($\log R \lesssim 1$ [pc]). Figure 6 shows where the overlapping-trough BALs are found in the distributions of $\log R$ and $\log U$ as well as $\log n$. The BAL gas that creates overlapping troughs has higher densities ($\log n \gtrsim 6\ [{\rm cm^{-3}}]$), higher ionization parameters ($\log U \gtrsim -1.85$), and higher hydrogen column density (Figure 7) compared to the BALs in the overall sample. These conditions are required to produce the high-excitation transitions that yield the necessary opacity at $\lambda \sim 2500$ Å. While the overlapping-trough BALs have a range of $\log U$ that spans about 2 dex, they are all found to be located in the vicinity of the dusty torus

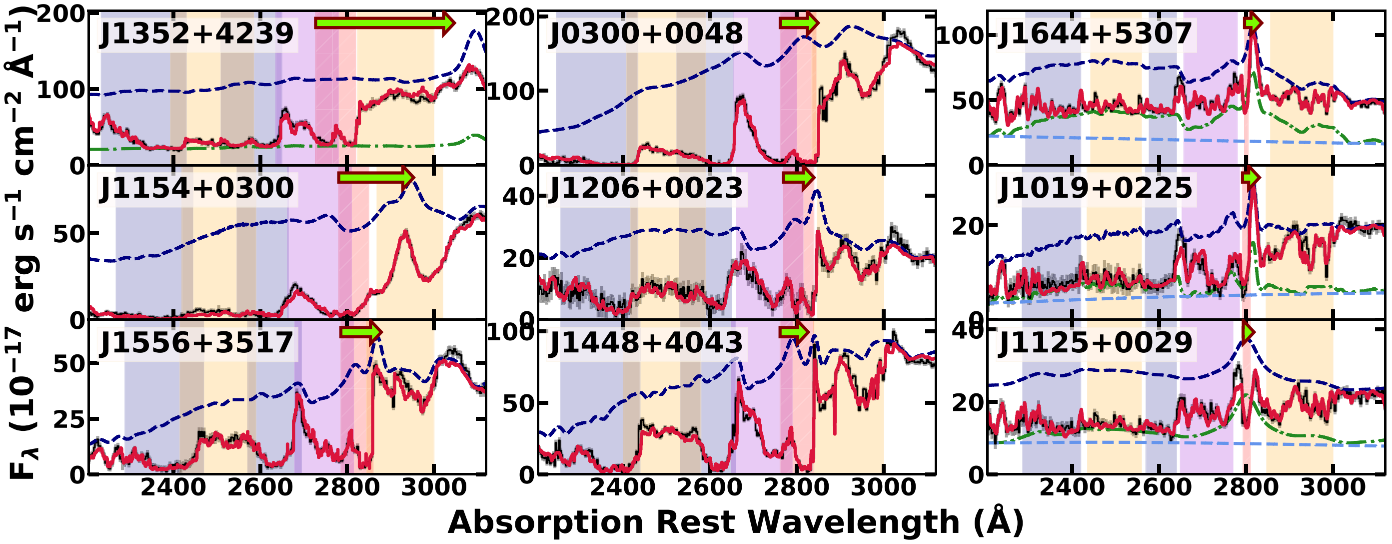

Figure 17. The eight objects with overlapping troughs are plotted with SDSS J1352+4239 (Choi et al. 2020). All the spectra have been shifted to the reference frame of the main BAL trough. The arrows extend from the estimated center of the Mg II trough to the center of emission line to illustrate the BAL offset velocity. The full spectral models and the continuum models are plotted in red and dashed blue lines, respectively. The green dotted–dashed lines show the unabsorbed line emission and continuum emission if present. The additional blue dashed lines in the three objects on the right column represent the unabsorbed power-law continuum emission. The shaded regions represent various absorption lines and absorption-line classes: red, Mg II; blue, low-excitation Fe II; pink, high-opacity moderate-excitation Fe II; yellow, low-opacity moderate-excitation Fe II. Also see Figure 3.

($\log R \lesssim 1$ [pc]). Based on the results from our sample, we conclude that the overlapping-trough features in the FeLoBALQ spectra can be used to identify compact BAL winds. Overlapping-trough BALs could give us information about the inner regions of quasars where we expect most of the acceleration to occur for radiatively driven outflows (e.g., Arav & Li 1994).

We identified three main ways FeLoBAL outflows create overlapping troughs. The most straightforward method is with large velocity widths. Although the kinematic properties of the BALs showed a wide range among the overlapping troughs in our sample, the high-velocity overlapping troughs plotted in the left two panels in Figure 17 represent the FeLoBALs with the highest outflow velocities and widths in our sample (Figure 5). For instance, SDSS J1154+0300 has the largest BAL width with ~7400 km s^{-1} and the offset velocity of ~−15,400 km s^{-1}. Naturally, with larger widths, the line blending is significant, and the high-opacity gas in these winds will be able to create wide overlapping-trough FeLoBAL features.

Second, overlapping troughs can be produced from moderate to narrow width BALs with large amounts of opacity from rare transitions. The width of the trough in SDSS J1644+5307 is only ~900 km s^{-1}, a value that is comparable or slightly smaller to the average value from other nonoverlapping FeLoBAL troughs. The overlapping-trough feature in that object is caused by the large number of excited-state Fe II transitions and absorption lines from multiple iron-peak elements between ~2000 and ~3000 Å. If an outflowing gas has a high enough density, ionization parameter, and column density to have a significant population of highly excited-state Fe II ($E_{\text{lower-level}} \gtrsim 3\,eV$), then the gas will be able to create thousands of absorption lines (see Figure 3). Because these absorption lines are densely packed, they can easily form a wide trough by line blending even with a narrow absorption line velocity width.

Finally, the objects that have an ordinary FeLoBAL component at lower velocity with an additional high-opacity component at higher velocity may show overlapping troughs in the spectra. As discussed in Section 6.2, some of the objects in the sample required more than one BAL component, and the overlapping-trough features were created by the higher-velocity, higher-log U components. For example, in Figure 12, we see that most of the higher-velocity components in objects with blended multi-BALs features (red arrows) are also identified as overlapping-trough BALs (pink circles). Figure 11 shows how these higher-velocity components produce the majority of the opacity needed to complete the overlapping-trough features near $\lambda \sim 2500$ Å. The lower-velocity components (Figure 11, plotted in green) resembled typical FeLoBALs, mainly showing BALs from the ground-state Fe II and Mg II transitions with little to no highly excited-state Fe II transitions (see Figure 3; Section 5.1.2). Without the higher-velocity components, these objects would appear nearly indistinguishable from the nonoverlapping-trough FeLoBALQs.

Some compact HiBAL outflows show BAL variability possibly due to the transverse motion of the outflow clouds or change in photoionization state of the outflow gas (e.g., Capellupo et al. 2013). For instance, the disappearance of overlapping troughs has been observed in FBQS J140806.2+305448 (Hall et al. 2011) and in SDSS J123103.70+392903.6 (Rafiee et al. 2016; McGraw et al. 2015). It is plausible that in some cases the variability might be coming from the disappearance of the higher-velocity component. For example, while the overlapping-trough features from Fe II disappeared in these two objects, the strength of the deep absorption feature from Mg II at the lower-velocity end remained consistent. The sample of radio-selected quasars analyzed by Zhang et al. (2015) showed an enhanced spectral variability rate for the overlapping-trough objects. However, three objects (SDSS J0300+0048, SDSS J1125+0029, SDSS J1154+0300) have been analyzed by McGraw et al. (2015), but no evidence for BAL variability was found. Shi et al. (2016) found evidence for spectral variability in SDSS J1125+0029; the variability they found was attributed to the unabsorbed line emission flux underneath the Fe II trough, and they did not find any significant change in the BAL troughs.

Some of the multicomponent objects with overlapping troughs (SDSS J1125+0029 and SDSS J1206+0023) showed a lower velocity and lower $-\log U$ component that only produces significant opacity from Mg II with little Fe II opacity (Section 6.2). The velocity of these components extends across $\sim$0 km s^{-1}, and they are located at about an order of magnitude larger distances than the higher-velocity components (Figure 12). The origins of these BAL components are uncertain. Discussions related to redshifted BALs that have similar kinematic characteristics have suggested rotationally dominated outflows or infalls as potential origins (Hall et al. 2013).

Three objects (SDSS J1019+0225, SDSS J1125+0029, SDSS J1644+5307) were modeled with a modified partial-covering scheme (Section 5.1.1), because the usual power-law partial-covering that is used in *SimBAL* was not sufficient to model the observed nonblack saturation. Although these three objects show overlapping-trough BALs in the spectra with no continuum emission recovery shortward of $\lambda \sim 2800$ Å, they do not meet the usual criteria for overlapping-trough object classification due to significant flux beneath the troughs. Choi et al. (2020) discussed the unabsorbed component under the overlapping troughs in SDSS J1352+4239 as scattered flux where $\sim$29% of the light from the accretion disk and the broad line region (BLR) is scattered directly into the line of sight. In these three objects, the inferred scattered fraction would have to be greater than 50%; this is unphysical. All three of these objects have compact outflows with $\log R \lesssim 1$ [pc], and their close proximity to the BLR and the accretion disk suggests that the BAL gas is physically only covering part of the continuum and line emission. Thus the nonzero flux at the bottom of the troughs are due to the strong partial-covering effect. In Paper III (Choi et al. 2022), we discuss the angular size scales of the accretion disk and broad line region seen from the locations of the BAL winds using the black hole masses and Eddington ratio estimates obtained in Paper II (Leighly et al. 2022). We conclude that the large angular size scales of the accretion disk seen from the BAL gas at these small $\log R$ values can plausibly produce this partial-covering scenario.

6.5. Loitering *Outflows*

We identified a group of eleven compact FeLoBAL winds with small offset velocities and distinct properties, and classified them as *loitering* outflows (we use the term *outflow* in the nomenclature, but note that some loitering outflows have $v_{\rm off} > 0$ km s^{-1}). The loitering outflows are defined by the following properties: (a) $\log R < 1$ [pc]; (b) $|v_{\rm off,FeII\ excited}| < 2000$ km s^{-1} and $v_{width\rm ,FeII\ excited} < 2000$ km s^{-1}. In other words, the loitering outflows are relatively static gas clouds that are located close to the central SMBHs within the vicinity of the torus, and thus they appear to be neither outflowing nor inflowing. Figure 18 shows how the distribution of the physical properties of loitering outflows differs from the other more typical BAL winds and our defining criteria.

Instead of using $v_{\rm off}$ and $v_{\rm width}$ estimated from the Mg II transition, we used the values measured from the excited-state Fe II$^*\lambda$ 2757 extracted from the I/I_0 models discussed in Section 4.3. This was done to avoid excluding any BALs with narrow Fe II absorption features that may have larger $v_{\rm off}$ or $v_{\rm width}$ due to extended Mg II opacity profiles. Moreover, the opacity profile of the excited-state Fe II traces the high-density cores within the BAL gas structure that produce the majority of opacity and carry most of the mass and energy in the wind. However as can be seen in Figure 18, our classifications would not have been significantly affected if we had used the standard $v_{\rm off}$ and $v_{\rm width}$ from Mg II. Only one BAL, in SDSS J1006+0513, showed modest differences between the values ($v_{\rm off} \sim -2400$ km s^{-1}, $v_{width} \sim 3500$ km s^{-1}; $v_{\rm off,FeII\ excited} \sim -1420$ km s^{-1}, $v_{width\rm ,FeII\ excited} \sim 830$ km s^{-1}). We note that the selection criteria were chosen based on the visual inspection of the distribution of parameters obtained from our low-redshift sample. Future work with larger samples and high-redshift objects may modify our selection criteria.

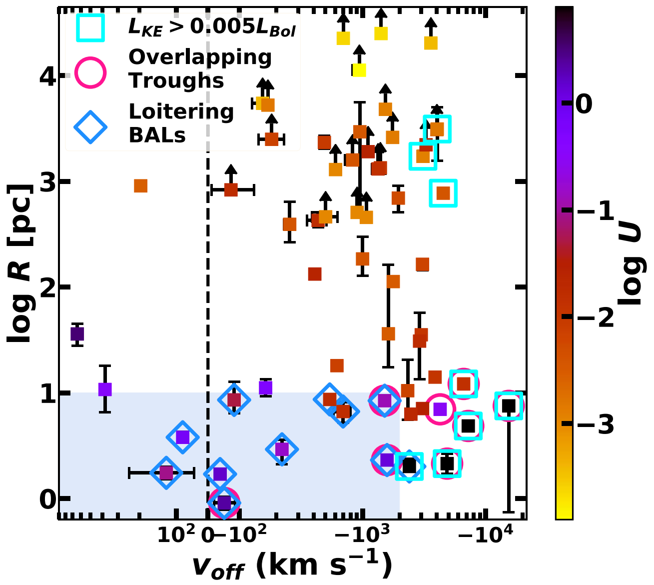

Figure 18. The distributions of the offset velocities ($v_{\rm off}$) and the distances of the BALs from the central SMBHs ($\log R$). The blue shaded region represents the defining criteria for the loitering outflows ($\log R < 1$, $|v_{\rm off,FeII\ excited}| < 2000$ km s^{-1}, and $v_{width\rm ,FeII\ excited} < 2000$ km s^{-1}). Excluding the loitering outflows and the inflows ($v_{\rm off} > 0$), we found robust statistical evidence ($p < 0.05$) for a correlation between $\log R$ and $v_{\rm off}$ where the high-velocity flows are found closer to the central engine. The error bars show 2σ (95.45%) uncertainties.

The loitering outflows have high $\log U$ with lower partial-covering (high $\log a$), and five out of eleven BALs required a modified partial-covering model. Conversely, five out of six objects modeled with modified partial-covering were found to have loitering outflows. These BALs show an extremely large number of absorption line transitions in the spectra because the high-$\log U$ FeLoBALs also have high column density, and such a thick gas slab can produce a plethora of rare line transitions from various excited-states Fe II as well as rarer iron-peak elements such as Co and Zn (Figure 3). Three of the eleven (SDSS J1019+0225, SDSS J1125+0029, and SDSS J1644+5307) loitering outflows are also classified as overlapping-trough BALs. These three were notable because they required step-function partial-covering for the power-law continuum emission and unabsorbed line emission in the model. In addition to these objects, SDSS J1128+0113 and SDSS J1321+5617 were modeled with modified partial-covering where the line emission was unabsorbed (Figure 2). The remaining six were modeled using the standard power-law partial-covering. These objects were characterized by lower signal-to-noise ratios (median signal-to-noise ratio $\sim$3–6), and it is possible that modified partial-covering would be required in higher signal-to-noise ratio spectra where the bottoms of the troughs would be better defined.

The locations of the loitering outflows in the quasar suggests the torus as a potential origin for the absorbing gas. The dust sublimation radius for quasars with $\log L_{\rm bol} \sim$ 46.0–47.0 [ergs^{-1}] is $R_{\rm sub} \sim$ 0.2–0.6 pc (Laor & Draine 1993). The outer radius of the torus was estimated to be $R_o \sim$ 40–120 [pc] using the equation $R_o < 12 L_{45}^{1/2}$ pc ($L_{45} = L_{\rm bol}/10^{45}\,{\rm erg\,s^{-1}}$; Nenkova et al. 2008). The loitering outflows are located at $R \sim 1-10$ pc, which is within the region where we expect the dusty torus to be. A wind origin of the torus has been proposed by Elitzur & Shlosman (2006), and recent studies using magnetohydrodynamic models of a dusty wind have been successful in finding potential connections between the outflowing winds and the windy torus structure (e.g., Keating et al. 2012; Gallagher et al. 2015). Paper II (Leighly et al. 2022) investigates the accretion properties of the FeLoBALQs that have loitering outflows (or so-called "loitering outflow objects"). We found that the loitering outflows all had lower-than-average accretion rates. Elitzur & Shlosman (2006) predict that, at low accretion rates, the wind forming the torus fails. In Paper IV (K. M. Leighly et al. 2022, in preparation), we conjecture that, in the loitering outflow objects, the torus wind is on the verge of failing, so that it is not optically thick enough to reprocess continuum into the infrared band, but is still optically thick enough to produce the observed Fe II absorption.

As expected from the similar size scales of the outflows ($\log R \lesssim 1.0$ [pc]), the spectral morphology of the loitering outflows resembles that of FeLoBALQs with Balmer absorption lines (Section 6.3.2). Using this spectral property, we can use the presence of the narrow Balmer absorption lines (as well as He I* to differentiate BALs from galaxy contamination) in the optical spectra to search for quasars with loitering outflows.

We found a significant correlation between the $v_{\rm off}$ of the BAL outflows and $\log R$ ($p = 0.02$, Kendall τ; Figure 18) when the loitering outflows and the inflows are removed ($N = 46$). The remaining compact BAL winds that are located at $\log R \lesssim 1.0$ [pc] have the highest outflow velocities, and most of them were also identified as overlapping-trough BALs with powerful outflows ($L_{\rm KE}/L_{bol} > 0.5\%$; Section 6.4). Assuming the BAL clouds have not traveled significantly such that their current locations in the quasars represent where they were initially launched, the simulations and statistical calculations predict that such a correlation should exist. For the line-driven outflows, the terminal velocities of the winds roughly correlate with the Keplerian circular velocity or the escape velocity at the launch radius (e.g., Proga & Kallman 2004; Giustini & Proga 2019). A simple equation of motion derivation using the radiative acceleration also predicts $v_{\rm off}$ or $v_\infty \propto R_{in}^{-1/2}$ where R_{in} is the inner wind radius or the launch radius (e.g., Hamann 1998; Leighly et al. 2009; Choi et al. 2020). Because the correlation was not apparent when the loitering outflows were included in the analysis, we postulate that the loitering outflows may represent a different BAL phenomenon with potentially different acceleration mechanisms involved (see also Paper III, Choi et al. 2022).

7. Discussion

7.1. Location and Origin of FeLoBAL Winds

Our results show that the FeLoBAL winds span a large range of radii or distances from the central SMBH. However, the number density of objects may not be constant with R. There is an apparent gap near $\log R \sim 2$ [pc]; see Figure 6. While a larger sample may fill this gap, we can use the assumed break around $\log R \sim 2$ [pc] to divide the FeLoBALs into two groups: the compact outflows with special spectral morphologies, and the distant galactic-scale outflows that could have potentially formed *in situ* Faucher-Giguère et al. (2012). In other words, these two groups that are largely separated in physical size may represent two intrinsically different types of BAL outflows that have different origins and physical processes including their acceleration.

The winds observed in these objects are not continuous but are clumpy (e.g., Hamann et al. 2011). Without an external confinement mechanism, the clumps should dissipate in order of sound-crossing time $t_{sc} = l/c_s$ where l is the characteristic cloud size and c_s is the sound speed (Hamann et al. 2001; Schaye 2001; Finn et al. 2014). For $l \sim \Delta R \sim 0.01$ pc (median from the sample) and $T \sim 10^4$ K BAL gas, the cloud will survive for $\sim$670 yr; however, it is more likely that the BAL wind is comprised of many smaller clouds with $l \sim \Delta R/N$ where N is the number of clouds (Hamann et al. 2013). In comparison, a characteristic flow time $t_f \sim R/v_{\rm outflow}$ for a BAL wind with $v_{\rm outflow} \sim 1000\,{\rm km\,s^{-1}}$ and $R \sim 1$ pc is $t_f \sim 1000$ yr. Based on these calculations and considering that the dissipation timescale cannot exceed the flow timescale, we can assume the FeLoBAL winds have not traveled far from their origin.

Theoretical disk wind models (e.g., Foltz et al. 1987; Arav & Li 1994) suggest the location of disk winds at $R \sim 0.01$ pc for luminous quasars (e.g., Proga et al. 2000; Proga & Kallman 2004). However, none of the FeLoBAL outflows in our sample were found at such a compact scale. Rather, the compact outflows in our sample ($R \sim 1-10$ pc) suggest a torus wind model where the winds originate from the dusty torus (e.g., Gallagher et al. 2015; Chan & Krolik 2016, 2017; Vollmer et al. 2018). It is possible that the polar dust discovered in spatially resolved mid-infrared observation (e.g., Hönig et al. 2013) has the same origin as these winds. Similar to the dusty torus winds, the polar dust models also predict dust at comparable-size-scales $R \sim 1-100$ pc with large dust masses, $M_{\rm dust} \sim 100$s $M_\odot$ (Hönig & Kishimoto 2017; Stalevski et al.2019).

The torus wind models may also provide intriguing explanations for some of the inflows that we observed in the sample (Section 5.1.3; Section 5.3). Most of the inflowing FeLoBAL gas is found at $R < 100$ pc (one at $R \sim 1000$ pc; Figure 18). It is plausible that these compact inflows may represent some kind of disruption in the vicinity of the torus where the resulting material falls toward the central engine. The distant inflow might be caused by some compaction of gas flows in the host galaxy.

Between $\sim$100 pc and $\sim$1000 pc from the center, photoionized gas can be observed in emission lines from the narrow line region (NLR). Observational evidence for quasar-driven winds at this size-scale is often observed in blueshifted [O III] lines (e.g., Zakamska et al. 2016; Vayner et al. 2021). These outflows have mass outflow rates comparable to the FeLoBAL outflows ($1 \lesssim \log \dot{M}_{\rm out} \lesssim 3$ [$M_\odot$ yr^{-1}]). Although a

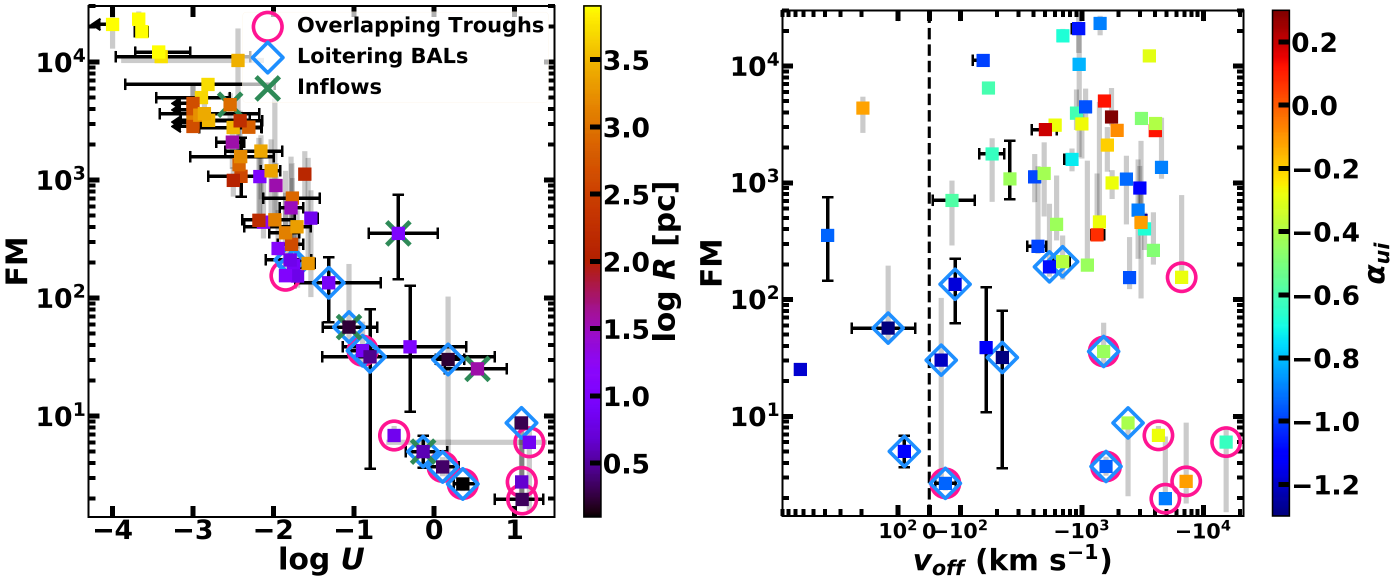

Figure 19. The force multiplier (FM) calculated using *Cloudy* with physical parameters from the best-fitting *SimBAL* models. *Left panel*: the FM is strongly correlated with ionization parameter. *Right panel*: we did not find robust correlation between the FM and the outflow velocity. The outflows with the highest-outflow velocities have relatively smaller FM. An extra source of opacity to capture the photon momentum, such as dust, or other acceleration mechanisms, may be needed to explain the high-velocity FeLoBALs. The high values of α_{ui}, flat or red SEDs, found in these objects could potentially indicate dusty outflows. Markers and error bars as in Figure 4.

direct connection between the [O III] outflows and BAL outflows is yet inconclusive (Paper III, Choi et al. 2022), it is possible that outflowing gas in the NLR can manifest as either BAL winds or emission line outflows or both depending on the physical conditions of the gas and/or sightlines.

Lastly, the potential origin of the kiloparsec-scale BAL winds can be explained by a model introduced by Faucher-Giguère et al. (2012), where a low radial filling factor results from in situ formation of outflows from the interaction between a dense ISM and a quasar blast wave. They concluded that the FeLoBAL outflowing gas may have properties comparable to massive molecular outflows that are generally found at similar distances from the central SMBHs (e.g., high momentum flux ratio; Section 7.3).

7.2. *Acceleration Mechanisms and SED Properties*

We used *Cloudy* to calculate the force multiplier (FM) for a radiatively driven outflow using the physical parameters constrained from the best-fitting models, and to investigate the relationship between the photoionization properties of the gas and the wind acceleration (i.e., outflow velocity). The FM is defined as the ratio of the total cross section (line and continuum processes) to the Thompson cross section. It represents how much radiative force the cloud can harness from the photons to power the outflow acceleration.

Figure 19 shows the distribution of FM as a function of $\log U$ and $v_{\rm off}$. FM decreases with $\log U$, which is consistent with analytical calculations that used the equation derived from the definition of FM (e.g., Castor et al. 1975; Arav & Li 1994; Arav et al. 1994). High-$\log U$ gas not only is highly ionized but also has larger hydrogen column density ($\log N_H$) and more material because $\log N_H - \log U$ is nearly constant in our FeLoBAL sample (Section 5.2.1). We found no correlation between FM and outflow velocity from our sample. In fact, the outflows with the highest velocities have among the lowest values of FM.

The low FM values in BALs with extreme outflow velocities ($v_{\rm off} \sim -10{,}000$ km s^{-1}) suggest that another acceleration mechanism is also playing a significant role. For instance, the radiation pressure on dust may play a significant role in accelerating the gas (e.g., Thompson et al. 2015; Murray et al. 2005; Ishibashi et al. 2017). Some of these high outflow velocity BALs are overlapping-trough BALs with anomalous reddening (Section 6.4), and they have flatter SED slopes (α_{ui}) than the rest (represented by the colors of the marker in the right panel of Figure 19). The flat SED slopes may indicate reddening in the quasar, which may suggest that the BALs in these objects are dusty. That is not to say that the BALs themselves have high dust content; dust reddening tends to suppress photoionization.

Figure 20 reveals that the outflow velocity is correlated with α_{ui} ($p = 0.003$, Kendall τ). The top axis shows the inferred values of $E(B-V)$ calculated using the composite quasar SED from Richards et al. (2006) ($\alpha_{ui} = -1.23$) and SMC reddening (Prevot et al. 1984). This strong correlation between the SED slope and outflow velocities in the FeLoBAL outflows is consistent with what has been found for ERQs. Hamann et al. (2017) analyzed a unique sample of ERQs at $2.0 < z < 3.4$ and discovered a high BAL fraction (∼30%–68%) and frequently the presence of outflow features. Perrotta et al. (2019) analyzed the [O III] emission lines in a subsample of ERQs from Hamann et al. (2017). They found a correlation between *i*–W3 color and outflow velocity where faster and more powerful outflows were found in redder quasars. It is plausible that this trend can be explained by FeLoBALQs being at a similar evolutionary stage as dusty, red quasars in a transitional phase in quasar evolution where obscured quasars are expelling gas and dust via outflows to become normal quasars (e.g., Hopkins et al. 2005; Urrutia et al. 2008; Glikman 2017; Glikman et al. 2018). However, FeLoBALQs in our sample are not ERQs, and the link between the red quasars and FeLoBALQs is still uncertain; LoBALQs are found among red quasars but no enhanced merger rates or

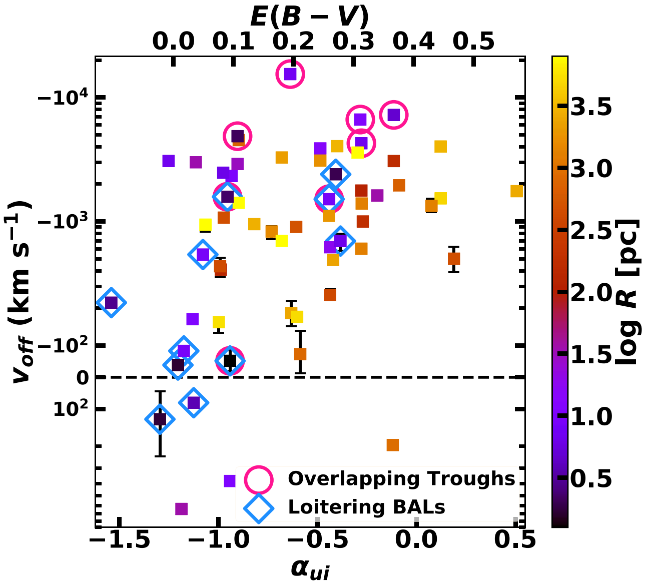

Figure 20. The outflow velocity ($v_{\rm off}$) is plotted against the SED slope parameter (α_{ui}). FeLoBALs with higher outflow velocities are found in objects with flatter or redder SEDs, where FeLoBALQs with steeper or bluer SEDs have compact outflows ($\log R \lesssim 1$ [pc]). Most of the compact outflows with steep SEDs are loitering outflows, and α_{ui} in these objects might be potentially affected by other SED properties than reddening such as the strength of IR emission from the torus (K. M. Leighly et al. 2022, in preparation). The top axis shows the values of $E(B-V)$ that correspond to the range of α_{ui} plotted on the bottom axis (assuming a composite quasar SED (Richards et al. 2006) and SMC reddening (Prevot et al. 1984)). The vertical error bars show 2σ (95.45%) uncertainties.

star formation rate has been found for FeLoBALQs (e.g., Violino et al. 2016; Villforth et al. 2019).

A simpler explanation for the correlation between the two properties is that the outflow itself as the source of reddening. First of all, a quasar outflow from the dusty torus can form a dusty wind (e.g., Gallagher et al. 2015). The dust is then sublimated, and we see BAL. Further downstream, the dust precipitates out of the gas (Elvis et al. 2002) producing the reddening. For instance, Dunn et al. (2015) suggested that the reddening in FeLoBALQs occurs at larger radial distances than the outflows. A multiwavelength SED analysis of red quasars supports the idea that dust in the winds are responsible for the reddening in these objects (Calistro Rivera et al. 2021). Thus for our FeLoBALs, flatter or redder SEDs can be the result of high-velocity outflows that carry more mass and energy causing more dust reddening. Similarly, the FeLoBALQs with the steepest, or the bluest, SEDs have the compact, low mass outflows with the lowest-outflow velocities that are characteristics of loitering outflows (Section 6.5).

In summary, FM analysis using *Cloudy* suggested that radiative line driving is insufficient for outflows with the highest outflow velocities located close to the central engine. We found compelling evidence that FeLoBALQs with redder SEDs have faster outflows. Based on these results, we speculate that the additional acceleration mechanism is acceleration by dust for these FeLoBALs. We note that the SED slope (α_{ui}) calculated from specific fluxes at rest-frame 2000 Å and 3 μm used in this work can be affected not only by reddening but also by other properties of the quasar such as the strength of torus. This point is investigated further in Paper IV (K. M. Leighly et al. 2022, in preparation).

7.3. Comparison with Other Forms of Outflows

Observational evidence for quasar outflows can be found both in blueshifted absorption lines and blueshifted or broad emission lines (e.g., Fabian 2012; King & Pounds 2015). All together, AGN-driven winds are found at a wide range of distance scales, from the ultra fast outflows seen in the X-ray band that are located in subparsec scales (e.g., Tombesi et al. 2010) to molecular winds at kiloparsec scales (e.g., Cicone et al. 2014). BAL outflows (e.g., Arav et al. 2018; Leighly et al. 2018; Choi et al. 2020) and the outflows seen as blueshifted [O III]$\lambda\lambda$4959,5007 emission lines (e.g., Harrison et al. 2014; Zakamska et al. 2016) are often found at parsec to kiloparsec scales, i.e., between the size scales of the X-ray and molecular outflows. It is conceivable that the different forms of outflows that we observe are related and originate in the same AGN-driven outflow phenomenon.

Fiore et al. (2017) compiled an extensive list of quasar outflows and their properties with more than one hundred wind measurements from the literature, limited to those that have robust estimates of the physical sizes of the outflows. Only 7 BAL outflows were included in their sample, possibly because BAL outflows were not the main focus of their investigation. Figure 21 shows our FeLoBAL outflows ($v_{\rm off} < 0$ km s^{-1}) combined with the Fiore et al. (2017) sample, as well as the FeLoBAL outflow in SDSS J135246.37+423923.5 (Choi et al. 2020). The color bar illustrates our observation of a strong relationship between the outflow properties and the observed shape of the SED. Outflows found in objects with a flatter SED slope tend to be more massive and powerful, which is expected given that there is a strong relationship between the outflow velocity and the slope of the SED (Sections 6.1; 7.2).

Similar to the other forms of quasar outflows, $\dot{M}$ and $L_{\rm KE}$ both increase with $L_{\rm Bol}$ in our FeLoBAL sample. We performed a Bayesian linear regression using `linmix`,[12] a python implementation of Kelly (2007), to determine how the correlation that we found among the FeLoBALs in our sample compares with the other outflow channels. We took into account the uncertainties associated with $\dot{M}_{\rm out}$ for the regression analysis. The log linear slope for our FeLoBALs is 1.02 ± 0.25, which is similar to the values Fiore et al. (2017), and it is found for other types of quasar outflows, except for the molecular outflows that were found to have a flatter slope of 0.76 ± 0.06 and higher mass outflow rates. Our slope is steeper than the values expected from the theoretical models (e.g., King & Pounds 2015, $\dot{M}_{\rm out} \propto L_{\rm Bol}^{1/3}$); however, as Fiore et al. (2017) pointed out in their discussion, the discrepancy might be explained by the presence of multiphase winds (i.e., underestimated $\dot{M}_{\rm out}$). Our regression slope for FeLoBALs corresponds to the ratio between the mass outflow rate and the mass accretion rate of 3. However, there is a large range in this ratio among the objects in our sample, from ∼0.04 to ∼80, more than two orders of magnitude. This result strongly suggests that a simple prescription of a fixed ratio between the mass outflow rate and mass accretion (or inflow) rate used in the subgrid physics in cosmological simulations (e.g., Choi et al. 2012) may not be adequate to reproduce the realistic quasar outflows and mechanical quasar feedback from the BAL winds. The sample of FeLoBALQs that we analyzed contains a number of BALs with low outflow velocities ($|v_{\rm off}| < 1000$km s^{-1}, Figure 5), which are seen in the right panel of Figure 21 in

---

[12] https://github.com/jmeyers314/linmix/

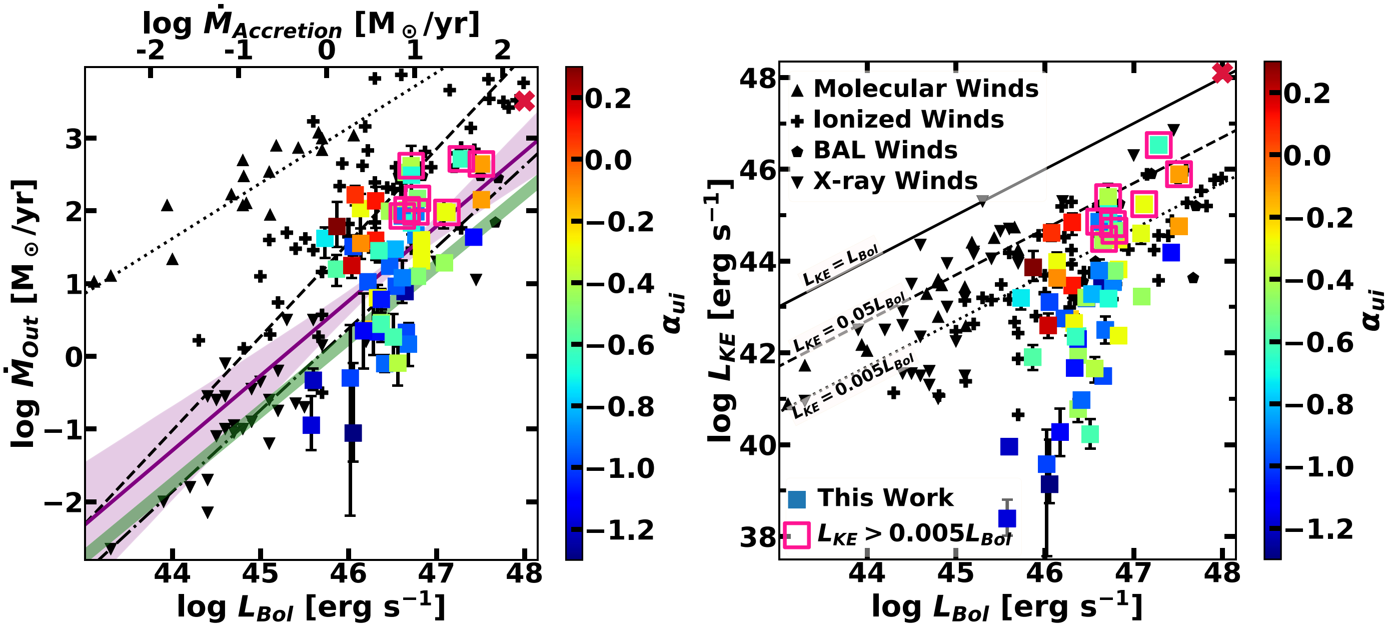

Figure 21. Our sample of FeLoBAL outflows and the compilation of outflows from Fiore et al. (2017). *Left panel*: the regression slopes shown as the dotted, dashed, and dotted–dashed lines for the molecular outflows, ionized winds, and X-ray outflows, respectively, taken from Fiore et al. (2017). The green line has a slope of one that represents $\dot{M}_{\rm Out} = \dot{M}_{\rm Accretion}$ (assuming the energy-conversion efficiency, $\eta = 0.1$). The purple line (shade) showing the regression for our sample of FeLoBALs has the slope of 1.02 ± 0.25, which is consistent with both ionized winds (1.29 ± 0.38; dashed line) and X-ray outflows (1.12 ± 0.16; dotted–dashed line). This result is also consistent with $\dot{M}_{\rm Out}/\dot{M}_{\rm Accretion} \sim 3$, although we observe a wide range of this ratio from ~0.04 to ~80 among the objects in our sample. *Right panel*: the solid, dashed, and dotted lines show $L_{\rm KE} = 1.0, 0.05, 0.005L_{\rm Bol}$, respectively. Pink square outlines denote the powerful outflows ($L_{\rm KE}/L_{\rm Bol} > 0.005$) in our sample that have well-constrained physical parameters and outflow properties. The red cross represents the outflow in SDSS J1352+4239 (Choi et al. 2020). The vertical error bars show 2σ (95.45%) uncertainties.

the comparatively lower values of $L_{\rm KE}$. Objects with weak or less massive outflows possibly have not been included in the Fiore et al. (2017) compilation or have not been analyzed in detail due to publication bias. The objects in our sample, on the other hand, were chosen to either have low redshift (Leighly et al. 2022) or be from the objects analyzed by Farrah et al. (2012), and are included in the sample regardless of the strength of the outflow.

We found a positive correlation between $L_{\rm Bol}$ and $v_{\rm off}$ in our sample of FeLoBAL outflows (left panel in Figure 22) that is consistent with trends observed in quasar outflows in general (e.g., Laor & Brandt 2002; Ganguly et al. 2007; Spoon et al. 2013; Veilleux et al. 2013; Fiore et al. 2017). Also, BALs with higher outflow velocities are found in objects with flatter or redder SED for a given bolometric luminosity (Section 7.2). This further propagates to the mass outflow rates and kinetic luminosity of the outflows (Figure 21) where, for a given bolometric luminosity, the objects that are redder have more massive and powerful outflows.

In a simple model for radiatively accelerated outflows where the wind is driven by the scattering of photons, and that process provides the momentum to accelerate the gas (i.e., a momentum-driven/conserving outflow), the maximum value for the momentum flux ratio ($\dot{P}_{\rm outflow}/\dot{P}_{\rm AGN}$; $\dot{P}_{\rm outflow} = \dot{M}_{\rm out} v_{\rm outflow}$, $\dot{P}_{\rm AGN} = L_{\rm Bol}/c$) is about 1 (e.g., King 2003; King & Pounds 2003). The right panel in Figure 22 shows that the FeLoBALs from our sample mostly show $\dot{P}_{\rm outflow}/\dot{P}_{\rm AGN} \lesssim 1$, and only a small fraction of outflows with high velocities have $1 \lesssim \dot{P}_{\rm outflow}/\dot{P}_{\rm AGN} \lesssim 10$. The distribution in momentum flux ratios can be ascribed to the relationship that outflows at larger distances from the center ($\log R$) have larger momentum flux ratios due to the winds being more massive ($\dot{M} \propto RN_H v$). However, it is also possible that the bolometric luminosity may have changed since the winds were launched thus potentially creating a large range of the momentum flux ratios depending on how the luminosities evolved in these objects (e.g., Ishibashi & Fabian 2018; Zubovas 2018). For instance, King et al. (2011) showed that an outflow may persist for an order of magnitude longer than the duration of the AGN event that powered it.

The outflows that have $\dot{P}_{\rm outflow}/\dot{P}_{\rm AGN} \gg 1$ may require different acceleration mechanisms to explain the large momentum load. Dust in the outflows can increase the opacity of the gas and harness the momentum of the photons more effectively, and this mechanism could potentially produce a momentum flux ratio above unity (e.g., Fabian et al. 2008, 2018). For the compact outflows with the highest outflow velocities, it seems likely the dust opacity has contributed to the momentum flux (Section 7.2). Molecular winds located at large distances ($\log R \gtrsim 2$ [pc]) also have high momentum flux ratios ($\dot{P}_{\rm outflow}/\dot{P}_{\rm AGN} > 10$); these outflows are thought to be accelerated by an energy-conserving outflow mechanism (e.g., King & Pounds 2015). A large fraction of the FeLoBAL outflows in our sample with high $\dot{P}_{\rm outflow}/\dot{P}_{\rm AGN}$ are found at large distances ($\log R \sim 3$ [pc]), which supports the energy-conserving outflow scenario. Conversely, not all distant FeLoBAL outflows have high momentum flux ratios, and the *in situ* wind formation model postulated by Faucher-Giguère et al. (2012) may explain the properties of these outflows more suitably.

7.4. Implications for AGN Feedback

In order for cosmological models and theoretical calculations to successfully explain the coevolution of the galaxies and the central black holes and to reproduce AGN feedback, the energy

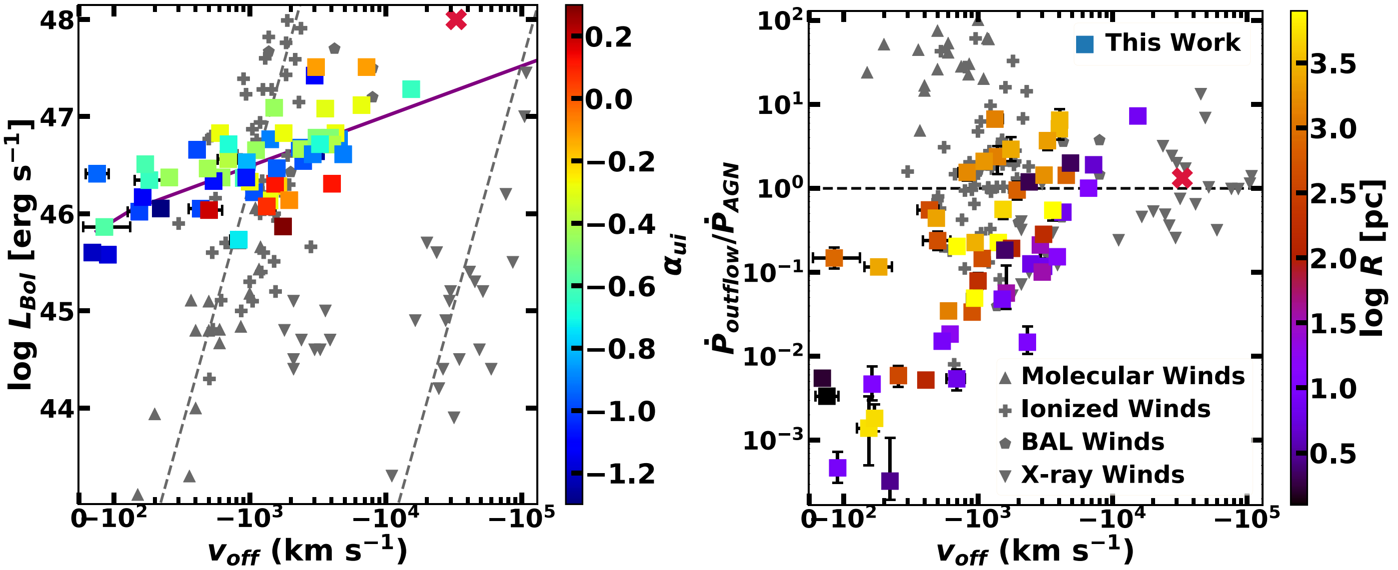

Figure 22. *Left panel*: the bolometric luminosity as a function of outflow velocity. The gray points represent the compilation of outflows from Fiore et al. (2017), and the red cross shows the FeLoBAL outflow in SDSS J1352+4239 (Choi et al. 2020). The purple line represents the regression slope, $L_{\rm Bol} \propto v_{\rm off}^{0.5}$, for our sample of FeLoBAL outflows, which differs dramatically from the $L_{\rm Bol} \propto v_{\rm off}^{5}$ scaling (dashed gray lines) described in Fiore et al. (2017). *Right panel*: the momentum flux ratio ($\dot{P}_{\rm outflow}/\dot{P}_{\rm AGN}$) as a function of outflow velocity. The dashed horizontal line marks the expected ratio for a momentum conserving outflow. The error bars show 95% uncertainties.

input from the AGNs to the host galaxies needs to be at least 0.5% $\sim$ 5% of the bolometric luminosity of the quasar (e.g., Scannapieco & Oh 2004; Di Matteo et al. 2005; Hopkins & Elvis 2010). From the 55 FeLoBAL outflows ($v_{\rm off} < 0$ km s^{-1}), we found that 8 BALs have kinetic luminosities greater than the 0.5% of the quasar bolometric luminosity. Out of 50 FeLoBALQs from the sample, 9 objects with BAL signatures were identified with powerful BAL outflows (note, two high-velocity outflows in SDSS J1448+4043 combined have $L_{\rm KE} > 0.005 L_{\rm Bol}$). Five objects out of the 9 with energetic outflows showed overlapping-trough features in the spectra (Section 6.4).

We identify a couple of reasons why this number may be underestimating the feedback potential of FeLoBAL outflows. First, we may not be finding many energetic outflows because our sample is dominated by objects with relatively low bolometric luminosities (median $\log L_{\rm bol} \sim 46.4$ [erg s^{-1}]). Energetic outflows are found in luminous quasars, and the outflow strength is correlated with the bolometric luminosity (Figure 21 right panel). This is further highlighted by the fact that the 9 objects with energetic outflows are among the most luminous quasars in our sample ($\log L_{\rm bol} > 46.6$ [ergs^{-1}]). For example, if we limit our sample to include only these high-luminosity objects, then we find that 50% of our FeLoBALQs have energetic outflows sufficient to power quasar feedback ($46.6 < \log L_{\rm Bol} < 47.6$ [erg s^{-1}]; 18 objects). This result is similar to what Miller et al. (2020) found in their sample of BALQs that have similar bolometric luminosity range as this high-luminosity subset. The flux-limited nature of a survey such as the SDSS means that more luminous objects are found at higher redshifts, and we expect such objects to have more powerful outflows.

Another reason that the outflow energy may be underestimated for FeLoBALs analyzed in this work is that they were calculated from the BAL physical properties estimated from the low-ionization lines, mainly using Fe II and Mg II absorption lines. (Fe)LoBALs also show absorption lines from the high-ionization species (e.g., C IV, Si IV) in the spectra, and they often show larger widths with higher outflow velocities (e.g., Voit et al. 1993; Hamann et al. 2019a). Thus we are not including the $L_{\rm KE}$ contributed by the higher-velocity portion of the high-ionization lines. In other words, the kinetic luminosity estimates based only on low-ionization lines may be taken as lower limits. Once taking these two effects into consideration, the distributions of FeLoBAL outflows in our sample described in Section 7.3 may shift to higher velocities and may not appear relatively weaker or less massive compared to the other forms of outflows included in the Fiore et al. (2017) compilation.

8. Summary and Conclusions

In this work, we presented the results and analysis from the first systematic study of a large sample of low-redshift FeLoBALQs. This work increases the number of well-studied FeLoBALQs by a factor of five. We were able to constrain the physical properties of the FeLoBAL outflows from the best-fitting *SimBAL* models and quantify the outflow properties. The summary of FeLoBAL properties is shown in Figure 23. Our principal results are the following:

1. We performed the first systematic study of a sample of 50 low-redshift ($0.66 < z < 1.63$) FeLoBALQs using *SimBAL*. From the best-fitting *SimBAL* models, we were able to identify 60 FeLoBAL components and constrain their physical properties as well as calculate their outflow properties (Figure 1; Section 5.2).
2. We found a wide range of ionization parameters ($\log U \sim -4$ to 1.2) and densities ($\log n \sim 2.8 - 8.0$ [cm^{-3}]) from our FeLoBALs, each spanning more than five orders of magnitude (Figure 4). The forward-modeling technique used in *SimBAL* enabled us to analyze high-log U FeLoBALs from heavily absorbed FeLoBALQ spectra.
3. The outflow properties calculated using the physical properties extracted from best-fitting *SimBAL* models

	R < 1 pc	1 < R < 10 pc	10 < R < 100 pc	100 < R < 1000 pc	R > 1000 pc
Quasar Property	Accretion disk, broad line region	Torus	Torus, polar dust, narrow line region (NLR)	NLR, extended NLR (ENLR)	ENLR, galaxy
Outflow Channels	Ultra fast outflows (UFOs)	BALs	BALs, ionized outflows (e.g., [OIII])	BALs, ionized outflows, molecular outflows (e.g., CO)	
Spectral Morphology	No FeLoBALs observed	Overlapping Trough, Loitering BAL (excited state FeII up to ~ 5 eV; iron peak elements, e.g., CrII, MnII)	Spectral archetype of FeLoBALs (mainly ground state FeII and MgII; excited state FeII up to ~ 1 eV)		Resemble intervening absorption systems (weak or no excited state FeII)
FeLoBAL Gas Properties (Ionization parameter, log U; density log n)		log U > -1 log n > 6 [cm^{-3}]	log U ~ -2 log n > 6 [cm^{-3}]	log U ~ -2 log n < 6 [cm^{-3}]	log U < -2 log n < 3 [cm^{-3}]
Observed Kinematic Properties		$-15{,}400 \lesssim v_{off} \lesssim 120$ km s^{-1} $280 \lesssim v_{width} \lesssim 7{,}400$ km s^{-1}	$-6{,}600 \lesssim v_{off} \lesssim 640$ km s^{-1} $350 \lesssim v_{width} \lesssim 8{,}800$ km s^{-1}		$-4{,}000 \lesssim v_{off} \lesssim -150$ km s^{-1} $140 \lesssim v_{width} \lesssim 4{,}300$ km s^{-1}
Gas Confinement and Structure		$-3 \lesssim \log \Delta R/R \lesssim 0$	$-6 \lesssim \log \Delta R/R \lesssim -4$		
Plausible Acceleration Mechanisms		Radiative line driving, dust acceleration		Radiative line driving, in-situ formation by "cloud-crushing"	In-situ formation by "cloud-crushing"

Figure 23. The summary of FeLoBAL properties found in our sample.

revealed a wide range of outflow locations ($\log R \sim 0.0$–4.4 [pc]; Figure 6). We found a significant correlation between outflow strength ($L_{\rm KE}$) and outflow velocity ($v_{outflow}$) from our sample (Figure 8) and confirmed that the outflow velocity is the principal factor in determining the outflow strength.

4. From the best-fitting *SimBAL* models, we identified multiple-outflow components in ~18% of the FeLoBALQs in our sample. The higher-velocity components had higher $\log U$, and some of them played a role in creating the overlapping-trough BALs (Sections 6.2; 6.4). The line profiles extracted from the *SimBAL* models showed discrete outflow gas structures and demonstrated how the BALs from the rare line transitions (e.g., He I*, Balmer series) that are found in the rest-optical band alone can be used to estimate the distances and physical properties of the FeLoBAL outflows (Figure 16).
5. Eight FeLoBALQs in our sample showed overlapping-trough features in the spectra (Figure 17). All of the overlapping-trough BALs were found close to the central engine $\log R \lesssim 1$ [pc]. Their kinematic properties showed a wide range ($v_{\rm off} \sim -15{,}400$ to $-50\,{\rm km\,s^{-1}}$, $v_{width} \sim 900$–$7400\,{\rm km\,s^{-1}}$), a fact that suggests that a large width is not required to create an overlapping-trough BAL. The five objects (~63%) that showed typical overlapping-trough features (e.g., high-velocity troughs reaching near-zero flux at the bottom) and anomalous reddening in the spectra have powerful outflows with $L_{\rm KE}$ exceeding 0.5% of $L_{\rm Bol}$.
6. We identified a new class of FeLoBALs dubbed loitering outflows (Section 6.5). They are characterized by compact outflows ($\log R < 1$ [pc]) and low outflow velocities ($|v_{\rm off}| \lesssim 2,\ 000\,{\rm km\,s^{-1}}$). Loitering outflows have high-$\log U$ and high-$\log n$ gas with large opacity; however, ~50% of them showed no absorption in the emission lines, and ~27% of the loitering outflow objects required an additional step-function partial-covering in the model because only a fraction of continuum emission was absorbed by the BAL (Section 5.1.1). The FeLoBALQs with loitering outflows can be identified by predicted Balmer absorption lines, and some of them show overlapping troughs as well. Their outflow property distributions (Figure 18) suggest that these objects may represent a distinct subpopulation within FeLoBALQs.
7. We found that the compact outflows are located within the vicinity of a dusty torus where a dusty wind scenario can be used to explain the origin and the acceleration mechanism of these FeLoBALs (Section 7.2). A FM analysis showed that radiative line driving alone may not be sufficient to accelerate the compact outflows at $R \lesssim 100$ pc to extreme velocities ($v_{\rm off} \sim -10{,}000\,{\rm km\,s^{-1}}$). An additional mode of acceleration (e.g., dust opacity; Figure 19) may be needed to explain these high-velocity outflows. In situ formation of FeLoBALs from the ISM (Faucher-Giguère et al. 2012) is a plausible model to describe the outflow properties of the kiloparsec-scale winds.
8. We found a significant correlation between SED slope (α_{ui}) and outflow velocity (Figure 20). The objects that have flatter SED slopes have faster and more powerful FeLoBAL outflows. A flatter SED slope may indicate strong dust reddening; note that the SED slope also depends on intrinsic AGN properties such as slope of the rest-optical/UV power law and the strength of torus emission.
9. We found that more luminous quasars have more powerful outflows (Figures 9; 21), consistent with trends observed in other forms of quasar outflows. The FeLoBAL outflows in our sample showed a wide range of the ratio between the mass outflow rate and the mass accretion rate, from ~0.04 to ~80, more than two orders of magnitude. This wide distribution suggests that a simple fixed ratio prescription used in some cosmological simulations may be insufficient for an accurate depiction of feedback by BAL outflows
10. Only nine objects out of 50 FeLoBALQs have sufficiently powerful outflows to produce quasar feedback. We suspect that a low fraction of powerful outflows is a

> consequence of the low redshift and therefore lower luminosity of our sample (median $\log L_{\mathrm{bol}} \sim 46.4$ [erg s^{-1}]). In addition, our analysis relied exclusively on the information extracted from the low-ionization lines, and it is known that the high-ionization lines from the same outflow tend to show extended structures at higher velocities. Therefore, our kinetic luminosity estimates may be considered to be lower limits.

We have expanded the number of FeLoBALQs that are analyzed in detail by a factor of five. More importantly, the detailed analysis made possible by *SimBAL* has fleshed out our picture of quasar outflows, allowing us to study the trends as a function of location and velocity. But there are still many questions left unanswered that we plan to investigate in the future. Do the outflow properties show correlations with the emission-line properties in these FeLoBALQs (Paper III, Choi et al. 2022)? Do the outflows in high redshift FeLoBALQs have similar physical properties as the low-redshift objects presented in this paper? We expect the FeLoBAL quasars with higher redshifts and therefore higher luminosities to have more powerful outflows than the low-redshift objects. However, it is uncertain whether the outflows in high-redshift FeLoBALQs have comparable physical properties such as ionization parameter and density. Preliminary results (Voelker et al. 2021) found a higher fraction of objects with powerful outflows in a sample of higher-redshift objects. They also found intriguing evidence suggesting that the distribution of physical properties of the FeLoBALs may change as a function of luminosity. Furthermore, we are developing a convolutional neural net to identify the FeLoBALQs from the SDSS archive with which we will be able to build larger samples of FeLoBALQs to perform follow-up studies (FeLoNET; Dabbieri et al. 2020, C. Dabbieri et al. 2022, in preparation). Future studies using a spectroscopic time series may provide additional information about the origin and acceleration mechanism of FeLoBAL winds. The outflow properties of our newly discovered class of FeLoBALs, loitering BALs (e.g., small R), potentially suggest that they might experience a higher probability of spectral variability (e.g., Zhang et al. 2015). New data may allow us to investigate the variability in these objects that could further constrain the geometry of the BAL gas around the accretion disk and the BLR to help us understand the partial-covering that we see in these BALQs.

The author thanks the current and past *SimBAL* group members and Jens-Kristian Krogager for useful discussions and comments on drafts. The work is funded by NSF grant AST-1518382, NSF grant AST-2007023, and AST-2006771 to the University of Oklahoma. This research has made use of the data from the SDSS/BOSS archive. Some of the computing for this project was performed at the OU Supercomputing Center for Education & Research (OSCER) at the University of Oklahoma.

Long before the University of Oklahoma was established, the land on which the University now resides was the traditional home of the “Hasinais” Caddo Nation and “Kirikiris” Wichita & Affiliated Tribes. This land was also once part of the Muscogee Creek and Seminole nations. We acknowledge this territory once also served as a hunting ground, trade exchange point, and migration route for the Apache, Comanche, Kiowa, and Osage nations. Today, 39 federally recognized Tribal nations dwell in what is now the State of Oklahoma as a result of settler colonial policies designed to assimilate Indigenous peoples. The University of Oklahoma recognizes the historical connection our university has with its Indigenous community. We acknowledge, honor, and respect the diverse Indigenous peoples connected to this land. We fully recognize, support, and advocate for the sovereign rights of all of Oklahoma’s 39 tribal nations. This acknowledgement is aligned with our university’s core value of creating a diverse and inclusive community. It is our institutional responsibility to recognize and acknowledge the people, culture, and history that make up our entire university community.

Funding for the Sloan Digital Sky Survey IV has been provided by the Alfred P. Sloan Foundation, the U.S. Department of Energy Office of Science, and the Participating Institutions. SDSS-IV acknowledges support and resources from the Center for High Performance Computing at the University of Utah. The SDSS website is www.sdss.org. SDSS-IV is managed by the Astrophysical Research Consortium for the Participating Institutions of the SDSS Collaboration including the Brazilian Participation Group, the Carnegie Institution for Science, Carnegie Mellon University, Center for Astrophysics | Harvard & Smithsonian, the Chilean Participation Group, the French Participation Group, Instituto de Astrofísica de Canarias, The Johns Hopkins University, Kavli Institute for the Physics and Mathematics of the Universe (IPMU)/University of Tokyo, the Korean Participation Group, Lawrence Berkeley National Laboratory, Leibniz Institut für Astrophysik Potsdam (AIP), Max-Planck-Institut für Astronomie (MPIA Heidelberg), Max-Planck-Institut für Astrophysik (MPA Garching), Max-Planck-Institut für Extraterrestrische Physik (MPE), National Astronomical Observatories of China, New Mexico State University, New York University, University of Notre Dame, Observatário Nacional/MCTI, The Ohio State University, Pennsylvania State University, Shanghai Astronomical Observatory, United Kingdom Participation Group, Universidad Nacional Autónoma de México, University of Arizona, University of Colorado Boulder, University of Oxford, University of Portsmouth, University of Utah, University of Virginia, University of Washington, University of Wisconsin, Vanderbilt University, and Yale University.

Software: emcee (Foreman-Mackey et al. 2013), Sherpa (Freeman et al. 2001), SimBAL (Leighly et al. 2018), Cloudy (Ferland et al. 2017).

Appendix A
Modeling the Continuum

The absorption line optical depths depend on the level of the continuum. When there is significant blending, it is important to have a reasonably robust method for modeling the continuum. In the first paper reporting *SimBAL* results, Leighly et al. (2018), we modeled the continuum, and then divided the spectrum by the model to isolate the absorption lines. In Leighly et al. (2019), we kept the shape of the continuum fixed, but allowed the normalization to vary. In Choi et al. (2020), we developed emission-line models from an Hubble Space Telescope (HST) observation of Mrk 493 and modeled the continuum with those and a power law.

All of these methods were stop-gap approximations that served while we developed a robust and reliable method that could routinely be used in *SimBAL*. Here we describe the method based on PCA that we found to work the best. Previous work on this topic has been reported by Leighly et al. (2017); Marrs et al. (2017); and Wagner et al. (2017). We note that we have also tried a variational autoencoder method (McLeod et al. 2020), but we found it that it did not offer any advantage over the PCA method that we describe below.

Spectral PCA has a long history in AGN and quasar astronomy, both as a method to study quasar line emission (e.g., Francis et al. 1992; Shang et al. 2003; Yip et al. 2004), or as a tool to model quasar spectra (e.g., Suzuki 2006; Pâris et al. 2011). Our methodology differs from typical analysis in several ways. First, we subtract the continuum, and only perform analysis on the emission lines. Second, we use the `EMPCA` algorithm (Bailey 2012), which weights the contribution of a spectrum to the PCA according to the uncertainty. Third, we split the results into groups of objects with similar spectra using k-means clustering on the eigenvector coefficients, and then we compute the eigenvectors for each group. This grouping method is useful because we can explain more of the variance with fewer eigenvectors and therefore require fewer parameters for continuum modeling in the *SimBAL* modeling procedure. Finally, we use the PCA model coefficients of the training set to set priors on the relative normalization of the eigenvectors compared with the mean spectrum. These methods are described further below.

A.1. The Sample and Continuum Modeling

The parent sample was drawn from SDSS DR4 quasars with redshifts between 1.2 and 1.8. These were examined by eye, and the ∼12000 objects with relatively narrow Mg II lines were selected. All of these objects were modeled between 2200 and 3050 Å using the method described in Leighly & Moore (2006). The spectral fitting was done using IRAF `SpecFit` using a model consisting of an iron template developed by us from the I Zw 1 HST observation following Vestergaard & Wilkes (2001), a power-law continuum, and additional Gaussians modeling C II]λ 2325, Fe II$\lambda\lambda$2419.3, 2438.9, and Mg II$\lambda\lambda$2795.5, 2802.7. The redshifts of the spectra were fine-tuned based on Mg II fit wavelengths. Objects with FWHM of Mg II greater than 3500 km s^{-1} were excluded, and, of those, the objects with signal-to-noise ratios less than the median value between 2200 and 2600 Å were excluded. The final sample consisted of 2626 objects. These were cleaned of bad points and the absorption lines from intervening absorbers.

We chose to remove the continuum from the spectra before performing the PCA analysis. The continuum of quasars has a large range of slopes (e.g., Krawczyk et al. 2015), and those differences in continuum shape add variance to the spectra. PCA measures the variance among spectra. Therefore, if the continuum is included in the quasar spectrum, one or more of the first several principal components will be dominated by continuum variance. For example, see the second eigenvector from Shang et al. (2003; their Figure 3). In addition, using such eigenvectors complicates the continuum modeling. To avoid these complications, the continuum was modeled and subtracted. We used an empirical model (a broken power law) between relatively line-free areas near 1675 Å, 2200 Å, and 3050 Å. The spectra were then normalized near 2200 Å, and the scaled continuum was subtracted.

A.2. The Weighted Expectation Maximization Principal Components Analysis Method

Traditionally, PCA is performed using singular-value decomposition (e.g., Suzuki 2006; Pâris et al. 2011). While straightforward, this is not the only way to compute PCA: Bailey (2012) presented a method to compute PCA that is done iteratively using an expectation-maximization algorithm (`EMPCA`).

One of the difficulties with the singular-value decomposition method is that there is a range of signal-to-noise ratios among the spectra. Noise adds variance, and because PCA detects variance, the resulting eigenvectors may be noisy despite a large training data set (e.g., Bailey 2012, their Figure 5). The Bailey (2012) method weights the contribution of each spectrum according to the inverse variance. Weighting can be done spectrum by spectrum, but there is an additional advantage of using the point-by-point version: if a point is weighted to zero, it will not be used for computing the PCA. Thus missing data can be accounted for without interpolation. Although we use a common bandpass in this application, in principle this capability allows the construction of PCA eigenvectors with a range of redshifts and bandpasses.

The weighted-mean spectrum was subtracted from each spectrum before `EMPCA` was run. The output of `EMPCA` are the specified number of eigenvectors. Because the method does not solve the eigen problem, the eigenvalues are not output. Instead, the fractional variance modeled is made available; the fractional variance can be used in a scree plot as usual. Also the outputs are the reconstruction coefficients of the training sample. Note that, because of the weighting, these do not have the same value as the dot product of an eigenvector and a spectrum as in the singular-value decomposition method.

A.3. K-means Grouping of Spectra

How many eigenvectors are needed to model a spectrum? Often a scree plot is used to determine this number. But that number may be large; for example, both Suzuki (2006) and Pâris et al. (2011) produce 10 eigenvectors, although not that many may be necessary for any particular application. However, for the application in *SimBAL*, we want to use as few eigenvectors as possible, since each one requires a model fit parameter that has to be constrained by the MCMC procedure. One way to reduce the number of eigenvectors that need to be used is to group the like spectra together and make several sets of eigenvectors. Spectra are conveniently grouped using the PCA coefficients for the whole sample (e.g., Suzuki 2006, their Figure 4), since objects with similar coefficients will have similar reconstructions.

We used the SciPy[13] implementation of K-means applied to the first four coefficients of the EMPCA result for the 2626 spectra. We arbitrarily specified five clusters. The resulting clusters contained from 179 to 829 spectra. The weighted-mean spectrum from each cluster can be seen in Figure 24. The means differ in the relative contribution of Fe II emission, Mg II emission, and C III emission. For example, one particular cluster may be used when the near-UV Fe II emission is relatively strong, while another cluster is more useful when C III] is very strong. One additional set of spectra was considered: 75 objects with the highest values of Fe II/Mg II ratio.

---

[13] SciPy.org

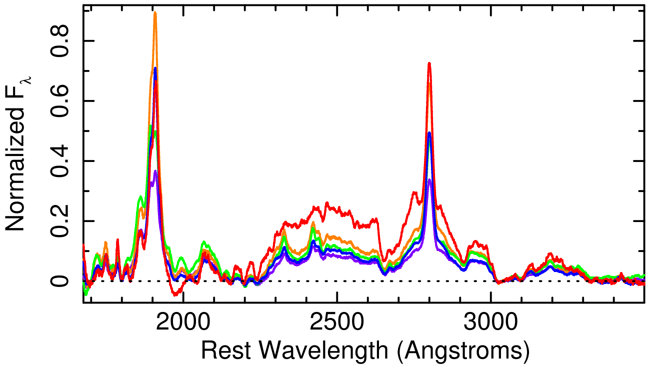

Figure 24. The mean spectra corresponding to our five principal sets of eigenvectors for near-UV model fitting. The five subsamples were constructed using k-means clustering on the first four `EMPCA` eigenvector reconstruction coefficients from analysis of the whole sample. The five sets of eigenvectors (plus an extreme Fe II/Mg II set) are sufficient to model most near-UV line emission morphologies.

We choose the appropriate set of eigenvectors to use by examination of the spectra. In cases of extreme absorption, the best choice is sometimes not clear (MacInnis 2018). However, because of the $e^{-\tau}$ nature of absorption, the uncertainties in continuum placement become less important for larger absorption columns.

A.4. PCA Coefficients as Priors

One of the challenges in using PCA eigenvectors to model the BAL quasar spectra is that, if unconstrained, the eigenvectors can model a portion of the absorption. The solution in the MCMC framework is to constrain the eigenvector amplitudes relative to the mean using priors. Specifically, a power-law-plus-emission-line continuum model may be expressed as follows:

$$C(\lambda) = N_{PL}(\lambda/\lambda_0)^{\alpha} + N_L \times (L_{\rm mean} + C_1E1 + C_2E2 + C_3E3 + C_4E4)$$

where N_{PL} is the power-law normalization at wavelength λ_0, α is the slope of power law, N_L is the normalization of the line emission, L_{mean} is the weighted-mean emission-line spectrum, C_1–C_4 are the fit coefficients for the eigenvectors, and $E1$–$E4$ are PCA eigenvectors. Thus this model has seven fit parameters—the two model component normalizations, the power-law slope, and the four eigenvector coefficients.

This problem of the PCA components modeling the absorption can be ameliorated if suitable priors are set on the eigenvector coefficients $C1$–$C4$. Initially, we fit a multidimensional Gaussian to the coefficients generated by the training sample. Because eigenvectors are orthogonal, the result was a nearly diagonal matrix. Then, a Gaussian prior was used for each of the coefficients.

In some cases, the Gaussian prior was not sufficient to control the eigenvector coefficients basically because a Gaussian profile has long tails. To more strongly disallow deviations very far from the center of the distribution, we also fit the coefficients with generalized Gaussian models, which have more sharply decreasing tails. In particular, an eighth-order generalized Gaussian was fit, and the priors for this distribution were provided as an option to the user.

A.5. The Long-wavelength Extension

Our sets of eigenvectors model the data satisfactorily between 1675 and 3500 Å. Some of the spectra of our lower-redshift objects extend to longer wavelengths, and include interesting absorption lines such as Ca II$\lambda\lambda$3994, 3968 and He I$^*\lambda$ 3889. Ideally, we would have a set of eigenspectra that extended to longer wavelengths; that infrastructure is planned for a future version of *SimBAL*. In the meantime, we use a single template spectrum that models the emission between 2870 Å and 4750 Å. The construction of this template spectrum is described in Leighly et al. (2011). The template is normalized to the eigenvectors using a lookup table matching the strong Fe II feature between 2820 and 3020 Å that appears in both the template and the mean spectrum from the EMPCA analysis. Thus, no additional normalization parameter is needed to use the long-wavelength extension.

Appendix B
FeLoBAL Outflow Properties

The best-fit parameters from the *SimBAL* models and the derived-outflow properties are presented in Tables 2 and 3, respectively. 95% uncertainties estimated from the posterior probability distributions are reported. For the BAL components that were fit using tophat accordion models, the range of values among the bins are reported. We report the opacity (column density) weighted velocity as the representative BAL velocity ($v_{\rm off}$) and the widths of BALs have been measured from the continuum emission normalized spectra (I/I_0) using the Mg IIλ2796 line transition (Section 4.2). The covering-fraction-corrected hydrogen column density ($\log N_H$; Section 5.3) for each individual BAL is reported in Table 3.

Table 2
SimBAL Fit Results

Name	log U	log n (cm^{-3})	$\log N_H - \log U$ (cm^{-2})	$v_{\rm off}$ (km s^{-1})	$v_{\rm width}$ (km s^{-1})	log a	Type[a]
J0111+1426	$-3.43^{+0.39}_{-0.29}$	<2.80	22.53-23.15	−3600 ± 30	760^{+0}_{-30}	−0.53 to 0.48	
J0158−0046	$-1.06^{+0.35}_{-0.33}$	$7.15^{+0.39}_{-0.38}$	23.06-23.64	120^{+120}_{-80}	1600^{+210}_{-80}	0.70-1.13	LB, IF
J0242−0722	-3.89 to -2.12	$4.24^{+0.17}_{-0.18}$	22.96-23.44	-950^{+60}_{-80}	1300^{+70}_{-80}	0.13-0.51	
J0258−0028a	$-2.12^{+0.08}_{-0.07}$	$7.15^{+0.08}_{-0.12}$	22.21-23.73	−620 ± 20	2300^{+0}_{-20}	−0.99 to 0.89	
J0258−0028b	$-2.40^{+0.27}_{-0.41}$	$4.74^{+0.49}_{-0.40}$	$23.69^{+0.08}_{-0.18}$	-260^{+20}_{-30}	620^{+70}_{-30}	$0.44^{+0.13}_{-0.23}$	
J0300+0048	-1.85 ± 0.001	$7.96^{+0.01}_{-0.02}$	23.09-23.72	−6600 ± 30	8800^{+0}_{-30}	0.08-0.60	OT
J0802+5513	$-2.54^{+0.04}_{-0.05}$	4.40 ± 0.04	22.99-23.10	200^{+9}_{-10}	1400^{+0}_{-10}	−1.45 to 0.36	IF
J0809+1818	$-1.53^{+0.09}_{-0.07}$	$7.63^{+0.07}_{-0.08}$	22.22-23.68	-3100^{+50}_{-60}	4600^{+0}_{-60}	−1.19 to 1.41	
J0813+4326	<−4.00	<2.80	22.08-22.92	-940^{+120}_{-60}	550^{+70}_{-60}	−0.54 to 0.11	
J0835+4242	-1.61 ± 0.06	5.18 ± 0.05	23.00-23.03	−410 ± 10	1200^{+70}_{-10}	0.58-1.26	
J0840+3633	-1.97 ± 0.03	$7.45^{+0.03}_{-0.01}$	23.09-23.22	−3000 ± 8	3400^{+0}_{-8}	−0.68 to 0.99	
J0916+4534	$-0.14^{+0.30}_{-0.21}$	$5.87^{+0.22}_{-0.28}$	$23.67^{+0.08}_{-0.21}$	80 ± 10	550^{+70}_{-10}	1.20 ± 0.05	LB, IF
J0918+5833	$0.54^{+0.36}_{-0.41}$	$3.92^{+0.27}_{-0.21}$	23.01 ± 0.07	640 ± 10	830^{+70}_{-10}	$0.88^{+0.06}_{-0.07}$	IF
J0944+5000	$-2.51^{+0.15}_{-0.20}$	$6.85^{+0.67}_{-1.29}$	22.50-23.18	−1600 ± 90	3800^{+140}_{-90}	0.15-1.78	
J1006+0513	$1.09^{+0.01}_{-0.07}$	$6.13^{+0.06}_{-0.10}$	22.95-23.71	−2400 ± 110	3500^{+140}_{-110}	0.86-2.43	LB
J1019+0225	$-0.89^{+0.18}_{-0.15}$	$7.29^{+0.15}_{-0.18}$	23.20-23.68	−1500 ± 20	1900^{+0}_{-20}	0.39-1.42	OT, LB
J1020+6023a	$-1.94^{+0.05}_{-0.01}$	$7.60^{+0.03}_{-0.05}$	23.16-23.73	-3900^{+10}_{-20}	1300^{+70}_{-20}	0.16-0.38	
J1020+6023b	$-2.92^{+0.12}_{-0.08}$	$4.40^{+0.10}_{-0.13}$	22.55-23.42	-3100^{+20}_{-30}	1700^{+70}_{-30}	−1.18 to 0.80	
J1022+3542	$-1.98^{+0.25}_{-0.41}$	<2.80	22.10-22.93	-1400^{+50}_{-60}	2200^{+0}_{-60}	−0.25 to 2.08	
J1023+0152	$-0.80^{+1.55}_{-0.59}$	$7.04^{+0.64}_{-1.26}$	$23.42^{+0.26}_{-0.40}$	−220 ± 20	550^{+70}_{-20}	1.27 ± 0.10	LB
J1030+3120	-2.17 ± 0.04	$7.97^{+0.57}_{-0.59}$	22.73-23.10	−2300 ± 20	3000^{+410}_{-20}	−0.21 to 1.55	
J1039+3954a	$-2.50^{+0.35}_{-0.42}$	<2.80	$23.10^{+0.19}_{-0.12}$	−4000 ± 10	410^{+70}_{-10}	$0.07^{+0.20}_{-0.24}$	
J1039+3954b	$-2.89^{+0.35}_{-0.56}$	<2.80	23.22 ± 0.15	−1500 ± 10	550^{+70}_{-10}	$0.10^{+0.18}_{-0.32}$	
J1044+3656a	-2.43 ± 0.01	$4.58^{+0.04}_{-0.05}$	21.98-23.02	-4500^{+6}_{-8}	1600^{+0}_{-8}	−1.04 to 0.32	
J1044+3656b	$-3.67^{+0.04}_{-0.05}$	<2.80	21.57–23.40	-1400^{+10}_{-9}	1400^{+0}_{-9}	−0.96 to 2.29	
J1125+0029a	$0.36^{+0.16}_{-0.11}$	$7.30^{+0.13}_{-0.15}$	23.21-23.74	−50 ± 30	830^{+0}_{-30}	1.24-2.04	OT, LB
J1125+0029b	$-0.45^{+0.49}_{-0.37}$	$5.93^{+0.41}_{-0.35}$	23.06 ± 0.02	380 ± 30	2800^{+140}_{-30}	0.94 ± 0.07	IF
J1128+0113	$-1.75^{+0.007}_{-0.001}$	$7.37^{+0.02}_{-0.01}$	22.16-23.71	-540^{+10}_{-20}	3000^{+0}_{-20}	−1.00 to 2.08	LB
J1129+0506	$-2.81^{+0.51}_{-0.35}$	$3.72^{+0.34}_{-0.44}$	21.91-23.42	-4000^{+280}_{-270}	2600^{+0}_{-270}	−0.41 to 0.57	
J1145+1100	$-0.30^{+0.70}_{-0.84}$	$5.54^{+0.76}_{-0.58}$	$23.11^{+0.22}_{-0.09}$	−160 ± 4	350^{+0}_{-4}	$0.31^{+0.13}_{-0.21}$	
J1154+0300	-0.60 to 1.40	7.27 ± 0.04	22.87-23.72	−15400 ± 50	7400^{+0}_{-50}	0.83-1.43	OT
J1158−0043	$-2.15^{+0.27}_{-0.45}$	<2.80	22.08-23.03	-180^{+40}_{-50}	1500^{+0}_{-50}	−0.36 to 0.37	
J1200+6322	$-1.77^{+0.15}_{-0.17}$	$3.73^{+0.13}_{-0.16}$	21.76-23.05	-440^{+80}_{-70}	3200 ± 70	−0.35 to 1.51	
J1206+0023a	$1.09^{+0.26}_{-0.34}$	$6.03^{+0.16}_{-0.09}$	22.94-23.36	-4900^{+160}_{-130}	3700^{+1200}_{-130}	1.42-2.08	OT
J1206+0023b	$-1.78^{+0.15}_{-0.14}$	$6.59^{+0.70}_{-0.52}$	23.01-23.07	-2900^{+160}_{-150}	5400^{+70}_{-150}	0.12-0.59	
J1208+6240	$-1.31^{+0.65}_{-0.41}$	$6.17^{+0.49}_{-0.66}$	$23.56^{+0.13}_{-0.27}$	-80^{+6}_{-4}	280^{+0}_{-4}	$0.74^{+0.14}_{-0.13}$	LB
J1212+2514	$-2.31^{+0.15}_{-0.17}$	3.93 ± 0.29	$23.02^{+0.06}_{-0.04}$	-2000^{+9}_{-10}	480^{+0}_{-10}	$-0.92^{+0.50}_{-0.55}$	
J1214−0001	$-2.81^{+0.83}_{-1.03}$	<2.80	$23.07^{+0.33}_{-0.13}$	−170 ± 10	280^{+0}_{-10}	$0.62^{+0.19}_{-0.31}$	
J1214+2803	$-1.70^{+0.004}_{-0.001}$	7.81 ± 0.01	22.15-23.72	-2500^{+6}_{-5}	2000^{+0}_{-5}	−1.22 to 0.53	
J1235+0132	$-1.79^{+0.26}_{-0.30}$	$7.88^{+0.44}_{-0.32}$	22.55-23.69	-700^{+110}_{-100}	2100^{+70}_{-100}	0.25-1.37	LB
J1240+4443	$-1.76^{+0.34}_{-0.36}$	<2.80	22.20-23.38	−70 ± 60	1000^{+70}_{-60}	0.33-1.26	
J1321+5617	$0.17^{+0.20}_{-0.15}$	$6.13^{+0.13}_{-0.17}$	23.07-23.75	-40^{+10}_{-20}	620^{+0}_{-20}	0.91-1.14	LB
J1324+0320	<−3.00	$5.04^{+0.35}_{-0.25}$	22.71-23.53	-900^{+70}_{-60}	2200^{+70}_{-60}	0.30-2.19	
J1336+0830	<−3.00	$5.06^{+0.03}_{-0.04}$	21.95-23.79	-1100^{+20}_{-7}	1900^{+0}_{-7}	−1.07 to 0.70	
J1355+5753	$-2.41^{+0.41}_{-0.63}$	<2.80	22.11-23.42	-830^{+110}_{-90}	1600^{+0}_{-90}	−0.22 to 1.86	
J1356+4527	$-1.85^{+0.17}_{-0.20}$	<2.80	21.93-23.14	-1300^{+140}_{-200}	4300^{+70}_{-200}	−0.16 to 1.07	
J1427+2709a	$-1.71^{+0.17}_{-0.65}$	<2.80	22.08-23.22	-3300^{+30}_{-60}	970^{+0}_{-60}	−0.54 to 1.09	
J1427+2709b	$-3.64^{+0.07}_{-0.09}$	<2.80	22.30-23.40	−700 ± 10	1200^{+0}_{-10}	−1.05 to 1.31	
J1448+4043a	$-0.50^{+0.008}_{-0.002}$	6.80 ± 0.01	23.49-23.74	−4300 ± 30	4500^{+0}_{-30}	1.24-1.67	OT
J1448+4043b	$-2.50^{+0.01}_{-0.02}$	$6.38^{+0.01}_{-0.02}$	22.73-23.80	−1800 ± 20	4300^{+0}_{-20}	−1.48 to 0.74	
J1448+4043c	<−3.00	$4.76^{+0.05}_{-0.06}$	23.72 ± 0.03	−600 ± 2	550^{+0}_{-2}	$-0.82^{+0.11}_{-0.13}$	
J1517+2328	<−3.00	$4.73^{+0.20}_{-0.25}$	23.03-23.60	-500^{+110}_{-120}	1700^{+280}_{-120}	−0.23 to 0.62	
J1527+5912	$-1.57^{+0.08}_{-0.10}$	<2.80	22.04-22.94	−1100 ± 30	2600^{+0}_{-30}	−0.86 to 0.87	
J1531+4852	$-3.40^{+1.11}_{-0.56}$	<2.80	$22.51^{+0.34}_{-0.44}$	-150^{+30}_{-7}	140^{+70}_{-7}	$-0.89^{+0.84}_{-0.59}$	
J1556+3517a	$1.09^{+0.005}_{-0.013}$	$6.21^{+0.06}_{-0.03}$	22.95-23.28	-7200^{+50}_{-60}	3500^{+0}_{-60}	1.03-2.06	OT
J1556+3517b	$-2.18^{+0.06}_{-0.04}$	$6.42^{+0.12}_{-0.08}$	22.71-23.72	-3100^{+40}_{-50}	4300^{+0}_{-50}	−1.33 to 0.67	
J1644+5307	$0.11^{+0.20}_{-0.17}$	$6.79^{+0.14}_{-0.16}$	23.23-23.61	−1600 ± 30	900^{+70}_{-30}	0.93-2.10	OT, LB
J2107+0054	$-2.86^{+0.69}_{-0.56}$	<2.80	22.05-23.13	-1800^{+90}_{-110}	1900^{+550}_{-110}	−0.37 to 1.14	
J2135−0320	$-2.03^{+0.11}_{-0.13}$	$2.92^{+0.15}_{-0.11}$	22.28-23.11	−490 ± 20	1200^{+0}_{-20}	−0.93 to 0.71	
J2307+1119	$-2.41^{+0.28}_{-0.48}$	$5.38^{+0.28}_{-0.23}$	22.98-23.05	-1000^{+60}_{-50}	2500^{+70}_{-50}	0.30-1.01	

Note.
[a] OT, overlapping-trough BAL; LB, loitering BAL; IF, inflow.

(This table is available in machine-readable form.)

Table 3
Derived-outflow Properties

Name	$\log N_H$ (cm^{-2})	$\log R$ (pc)	$\log \dot{M}_{\mathrm{out}}$ $(M_\odot\ \mathrm{yr}^{-1})$	$\log \dot{M}_{in}$ $(M_\odot\ \mathrm{yr}^{-1})$	$\log \dot{P}$ (dyne)	$\log L_{KE}$ $(\mathrm{erg\ s}^{-1})$	$\log L_{\mathrm{Bol}}$ $(\mathrm{erg\ s}^{-1})$	α_{ui}
J0111+1426	$19.35^{+0.28}_{-0.17}$	>4.31	$1.99^{+0.15}_{-0.23}$	⋯	$36.35^{+0.14}_{-0.23}$	$44.60^{+0.14}_{-0.23}$	47.08	−0.30
J0158−0046	$21.92^{+0.28}_{-0.26}$	0.24 ± 0.06	$-1.31^{+0.42}_{-0.51}$	$-0.82^{+0.42}_{-0.35}$	$32.06^{+0.43}_{-0.56}$	$39.33^{+0.44}_{-0.63}$	45.42	−1.29
J0242−0722	$20.56^{+0.16}_{-0.15}$	$3.47^{+0.28}_{-0.77}$	$1.47^{+0.10}_{-0.09}$	⋯	35.41 ± 0.09	43.28 ± 0.09	46.53	−0.82
J0258−0028a	21.61 ± 0.04	1.26 ± 0.04	$0.41^{+0.07}_{-0.05}$	⋯	$34.16^{+0.08}_{-0.05}$	$41.95^{+0.09}_{-0.06}$	46.37	−0.44
J0258−0028b	$20.70^{+0.24}_{-0.33}$	$2.59^{+0.21}_{-0.17}$	$0.46^{+0.18}_{-0.26}$	⋯	$33.67^{+0.20}_{-0.27}$	$40.77^{+0.22}_{-0.28}$	46.37	−0.44
J0300+0048	22.31 ± 0.01	1.08 ± 0.01	1.98 ± 0.01	⋯	36.64 ± 0.01	45.24 ± 0.01	47.12	−0.28
J0802+5513	$20.92^{+0.03}_{-0.04}$	$2.96^{+0.03}_{-0.02}$	0.33 ± 0.05	1.03 ± 0.03	33.55 ± 0.06	40.73 ± 0.06	46.62	−0.12
J0809+1818	$21.79^{+0.06}_{-0.05}$	$0.85^{+0.02}_{-0.01}$	0.89 ± 0.06	⋯	35.24 ± 0.06	43.54 ± 0.07	46.64	−1.25
J0813+4326	$18.94^{+0.35}_{-0.17}$	>4.05	$0.78^{+0.14}_{-0.18}$	⋯	$34.59^{+0.14}_{-0.18}$	$42.30^{+0.15}_{-0.18}$	46.37	−1.06
J0835+4242	20.83 ± 0.05	2.12 ± 0.03	0.33 ± 0.04	⋯	33.90 ± 0.05	41.50 ± 0.06	46.66	−0.99
J0840+3633	21.85 ± 0.02	$1.55^{+0.005}_{-0.008}$	$1.64^{+0.01}_{-0.02}$	⋯	$35.95^{+0.01}_{-0.02}$	$44.18^{+0.01}_{-0.02}$	47.42	−1.11
J0916+4534a	$22.29^{+0.18}_{-0.16}$	0.58 ± 0.05	⋯	$-0.47^{+0.19}_{-0.18}$	⋯	⋯	45.73	−1.12
J0918+5833	$22.62^{+0.28}_{-0.33}$	$1.56^{+0.10}_{-0.11}$	⋯	$1.74^{+0.20}_{-0.26}$	⋯	⋯	46.41	−1.19
J0944+5000	$20.83^{+0.13}_{-0.15}$	$1.56^{+0.65}_{-0.32}$	$0.37^{+0.59}_{-0.35}$	⋯	$34.56^{+0.58}_{-0.36}$	$42.73^{+0.58}_{-0.36}$	46.28	−0.20
J1006+0513	$23.57^{+0.04}_{-0.08}$	$0.30^{+0.07}_{-0.03}$	$2.01^{+0.06}_{-0.05}$	⋯	$36.27^{+0.07}_{-0.06}$	44.48 ± 0.08	46.67	−0.41
J1019+0225	$22.42^{+0.10}_{-0.07}$	0.92 ± 0.03	$1.29^{+0.10}_{-0.08}$	⋯	$35.29^{+0.10}_{-0.09}$	$43.23^{+0.10}_{-0.09}$	47.09	−0.44
J1020+6023a	$21.60^{+0.03}_{-0.02}$	$1.15^{+0.01}_{-0.02}$	1.10 ± 0.03	⋯	35.49 ± 0.03	43.79 ± 0.03	46.78	−0.48
J1020+6023b	20.68 ± 0.07	3.24 ± 0.05	$2.17^{+0.07}_{-0.06}$	⋯	$36.46^{+0.07}_{-0.06}$	$44.66^{+0.07}_{-0.06}$	46.78	−0.48
J1022+3542	$20.98^{+0.26}_{-0.40}$	>3.13	$2.03^{+0.20}_{-0.45}$	⋯	$36.04^{+0.20}_{-0.45}$	$43.98^{+0.21}_{-0.45}$	46.14	−0.28
J1023+0152	$21.35^{+1.11}_{-0.35}$	$0.46^{+0.09}_{-0.14}$	$-1.05^{+0.96}_{-0.39}$	⋯	$32.09^{+0.97}_{-0.40}$	$39.14^{+0.97}_{-0.41}$	46.05	−1.54
J1030+3120	$21.01^{+0.04}_{-0.05}$	$1.02^{+0.29}_{-0.27}$	$0.17^{+0.29}_{-0.30}$	⋯	$34.37^{+0.29}_{-0.30}$	$42.50^{+0.29}_{-0.30}$	46.68	−0.93
J1039+3954a	$20.27^{+0.29}_{-0.33}$	>3.49	$2.14^{+0.19}_{-0.28}$	⋯	$36.54^{+0.19}_{-0.28}$	$44.85^{+0.19}_{-0.28}$	46.31	0.12
J1039+3954b	$19.96^{+0.27}_{-0.34}$	>3.68	$1.60^{+0.17}_{-0.27}$	⋯	$35.58^{+0.17}_{-0.27}$	$43.47^{+0.17}_{-0.27}$	46.31	0.12
J1044+3656a	20.68 ± 0.01	2.89 ± 0.02	$1.99^{+0.03}_{-0.02}$	⋯	$36.45^{+0.03}_{-0.02}$	$44.81^{+0.03}_{-0.02}$	46.77	−0.90
J1044+3656b	19.36 ± 0.03	>4.40	1.67 ± 0.01	⋯	$35.65^{+0.01}_{-0.02}$	43.54 ± 0.02	46.77	−0.90
J1125+0029a	23.05 ± 0.09	-0.04 ± 0.06	$-0.10^{+0.12}_{-0.11}$	$-0.31^{+0.14}_{-0.12}$	33.46 ± 0.13	$40.97^{+0.14}_{-0.15}$	46.41	−0.94
J1125+0029b	$21.63^{+0.43}_{-0.33}$	$1.03^{+0.22}_{-0.21}$	⋯	$0.01^{+0.28}_{-0.27}$	⋯	⋯	46.41	−0.94
J1128+0113	21.84 ± 0.01	0.94 ± 0.01	0.34 ± 0.01	-0.50 ± 0.04	34.04 ± 0.01	$41.67^{+0.01}_{-0.02}$	46.34	−1.08
J1129+0506	$20.78^{+0.29}_{-0.27}$	$3.49^{+0.21}_{-0.30}$	$2.62^{+0.28}_{-0.27}$	⋯	37.05 ± 0.28	$45.39^{+0.28}_{-0.29}$	46.71	−0.40
J1145+1100	$22.33^{+0.57}_{-0.55}$	1.05 ± 0.08	$0.35^{+0.51}_{-0.52}$	⋯	$33.36^{+0.51}_{-0.52}$	$40.28^{+0.51}_{-0.53}$	46.17	−1.13
J1154+0300	23.62 ± 0.02	$0.88^{+0.03}_{-1.01}$	$2.71^{+0.03}_{-0.02}$	⋯	$37.67^{+0.03}_{-0.02}$	$46.53^{+0.03}_{-0.02}$	47.28	−0.64
J1158−0043	$20.90^{+0.25}_{-0.36}$	>3.40	$1.45^{+0.13}_{-0.16}$	$0.87^{+0.22}_{-0.30}$	$34.93^{+0.14}_{-0.16}$	$42.35^{+0.14}_{-0.17}$	46.35	−0.63
J1200+6322	$21.31^{+0.14}_{-0.15}$	$2.63^{+0.08}_{-0.07}$	1.51 ± 0.12	1.01 ± 0.17	35.32 ± 0.13	$43.11^{+0.14}_{-0.13}$	46.05	−0.99
J1206+0023a	$23.15^{+0.12}_{-0.16}$	$0.33^{+0.10}_{-0.09}$	$1.93^{+0.07}_{-0.09}$	⋯	$36.44^{+0.07}_{-0.09}$	$44.86^{+0.08}_{-0.10}$	46.61	−0.90
J1206+0023b	$21.37^{+0.14}_{-0.13}$	$1.49^{+0.27}_{-0.36}$	$1.08^{+0.24}_{-0.35}$	⋯	$35.46^{+0.24}_{-0.35}$	$43.79^{+0.24}_{-0.35}$	46.61	−0.90
J1208+6240	$21.43^{+0.39}_{-0.29}$	$0.93^{+0.17}_{-0.13}$	$-0.95^{+0.40}_{-0.34}$	⋯	$31.77^{+0.41}_{-0.36}$	$38.39^{+0.41}_{-0.37}$	45.58	−1.17
J1212+2514	$20.66^{+0.14}_{-0.15}$	$2.84^{+0.12}_{-0.13}$	$1.55^{+0.20}_{-0.21}$	⋯	$35.64^{+0.20}_{-0.21}$	$43.63^{+0.20}_{-0.21}$	46.14	−0.09
J1214−0001b	$19.55^{+0.66}_{-0.67}$	>3.72	$0.27^{+0.32}_{-0.30}$	⋯	$33.29^{+0.33}_{-0.30}$	$40.23^{+0.34}_{-0.31}$	46.51	−0.60
J1214+2803	22.01 ± 0.01	$0.80^{+0.007}_{-0.005}$	0.96 ± 0.01	⋯	35.17 ± 0.01	43.28 ± 0.01	46.54	−0.97
J1235+0132	$21.47^{+0.22}_{-0.25}$	$0.82^{+0.09}_{-0.11}$	$-0.09^{+0.23}_{-0.31}$	$-1.45^{+0.29}_{-0.37}$	$33.82^{+0.23}_{-0.31}$	$41.66^{+0.25}_{-0.31}$	46.56	−0.38
J1240+4443	21.33 ± 0.28	>2.92	$1.20^{+0.19}_{-0.23}$	$0.92^{+0.22}_{-0.25}$	$34.56^{+0.23}_{-0.25}$	$41.91^{+0.26}_{-0.28}$	45.86	−0.59
J1321+5617	$22.89^{+0.13}_{-0.12}$	$0.23^{+0.03}_{-0.04}$	$-0.33^{+0.16}_{-0.14}$	$-0.74^{+0.11}_{-0.15}$	$32.86^{+0.16}_{-0.14}$	$39.96^{+0.15}_{-0.14}$	45.60	−1.20
J1324+0320a	$20.01^{+0.16}_{-0.06}$	>2.71	$0.44^{+0.15}_{-0.18}$	⋯	$34.42^{+0.16}_{-0.18}$	$42.37^{+0.15}_{-0.17}$	46.37	−0.61
J1336+0830	20.57 ± 0.02	>2.66	1.02 ± 0.02	⋯	34.91 ± 0.02	$42.75^{+0.02}_{-0.03}$	46.22	−0.97
J1355+5753	$20.74^{+0.33}_{-0.51}$	>3.20	$1.62^{+0.15}_{-0.27}$	⋯	$35.45^{+0.15}_{-0.26}$	$43.20^{+0.15}_{-0.26}$	45.73	−0.73
J1356+4527	$21.21^{+0.16}_{-0.18}$	>3.12	$2.22^{+0.12}_{-0.14}$	⋯	36.42 ± 0.16	44.62 ± 0.18	46.08	0.08
J1427+2709a	$20.85^{+0.15}_{-0.53}$	>3.35	$2.49^{+0.08}_{-0.81}$	⋯	$36.81^{+0.08}_{-0.81}$	$45.03^{+0.08}_{-0.80}$	46.72	−0.68
J1427+2709b	19.88 ± 0.04	>4.35	1.83 ± 0.02	⋯	35.55 ± 0.02	$43.18^{+0.02}_{-0.03}$	46.72	−0.68
J1448+4043a	22.37 ± 0.01	$0.84^{+0.005}_{-0.006}$	$1.60^{+0.01}_{-0.02}$	⋯	$36.07^{+0.01}_{-0.02}$	$44.47^{+0.01}_{-0.02}$	46.83	−0.28
J1448+4043b	21.41 ± 0.01	2.05 ± 0.01	1.47 ± 0.01	⋯	35.64 ± 0.02	43.82 ± 0.02	46.83	−0.28
J1448+4043c	20.66 ± 0.02	>3.11	1.31 ± 0.02	⋯	34.89 ± 0.02	42.37 ± 0.02	46.83	−0.28
J1517+2328	$21.12^{+0.17}_{-0.12}$	>2.66	$1.25^{+0.18}_{-0.17}$	$<-1.80^{+1.49}$	34.94 ± 0.22	$42.60^{+0.26}_{-0.28}$	46.04	0.19
J1527+5912	$21.44^{+0.09}_{-0.10}$	>3.28	$2.53^{+0.06}_{-0.07}$	⋯	$36.50^{+0.06}_{-0.08}$	$44.43^{+0.07}_{-0.08}$	46.65	−0.44
J1531+4852b	$18.98^{+1.23}_{-0.64}$	>3.74	$-0.30^{+0.73}_{-1.89}$	⋯	$32.69^{+0.74}_{-1.95}$	$39.57^{+0.75}_{-2.01}$	46.02	−1.00
J1556+3517a	23.34 ± 0.02	$0.69^{+0.02}_{-0.03}$	2.64 ± 0.03	⋯	37.31 ± 0.03	45.89 ± 0.03	47.51	−0.11
J1556+3517b	21.69 ± 0.03	$2.22^{+0.04}_{-0.06}$	$2.15^{+0.06}_{-0.08}$	⋯	$36.49^{+0.06}_{-0.08}$	$44.76^{+0.06}_{-0.08}$	47.51	−0.11
J1644+5307a	$22.91^{+0.12}_{-0.10}$	0.36 ± 0.03	$1.24^{+0.10}_{-0.09}$	⋯	$35.26^{+0.10}_{-0.09}$	$43.19^{+0.10}_{-0.09}$	46.47	−0.95
J2107+0054	$20.36^{+0.64}_{-0.40}$	>3.42	$1.79^{+0.34}_{-0.28}$	⋯	$35.86^{+0.35}_{-0.29}$	$43.86^{+0.36}_{-0.30}$	45.87	0.51
J2135−0320	$21.17^{+0.10}_{-0.11}$	3.37 ± 0.06	$2.00^{+0.09}_{-0.10}$	⋯	$35.63^{+0.09}_{-0.10}$	$43.20^{+0.09}_{-0.11}$	46.47	−0.42
J2307+1119	$20.78^{+0.23}_{-0.36}$	$2.27^{+0.21}_{-0.16}$	$0.80^{+0.18}_{-0.20}$	⋯	$34.75^{+0.18}_{-0.20}$	$42.65^{+0.18}_{-0.20}$	46.33	−0.27

(This table is available in machine-readable form.)

Appendix C
Notes on Individual Objects

011117.36+142653.6 This object is included in the Farrah et al. (2012) sample, and has been observed twice by SDSS. It was originally classified as an FeLoBAL quasar by Trump et al. (2006). It was reported have been detected by ROSAT (Anderson et al. 2007), and was detected in the near-UV by Galaxy Evolution Explorer (GALEX; Trammell et al. 2007). It was observed using *SCUBA-2* but was not detected (Violino et al. 2016). Two Gaussian absorption profiles were used to model the absorption features. They were constrained to have the same ionization parameter and density while other parameters were allowed to vary. However, we combined the two Gaussians together for the analysis as a single BAL outflow component for determining the outflow mass rates and the hydrogen column densities. The break in the continuum near 3000 Å required the use of a general reddening curve (Choi et al. 2020).

015813.56–004635.5 This object was observed once by SDSS and is included in the DR14 SDSS quasar catalog (Pâris et al. 2018). A four-bin tophat model (single ionization parameter and single density) was used.

024254.66–072205.6 This object is included in the Farrah et al. (2012) sample, and has been observed once by SDSS. It was originally classified as an FeLoBAL quasar by Trump et al. (2006). It was observed using *SCUBA-2* but was not detected (Violino et al. 2016). A six-bin tophat with two-covering model was used. All bins were constrained to have a single-density parameter while other parameters, including the ionization parameter, were allowed to vary. The SMC reddening for this object was fixed to a value of $E(B-V)=0.075$ obtained from a fit to the photometry.

025858.17–002827.0 This object has been observed three times using SDSS, and is included in the DR14 SDSS quasar catalog (Pâris et al. 2018). It was identified as a BALQ in the DR10 SDSS quasar catalog (Pâris et al. 2014). A combination of an eight-bin tophat (single ionization parameter and single density) and a Gaussian opacity profile was used to model the two BAL components found in the spectrum. The general reddening law was used in the continuum model.

030000.57+004828.0 This bright overlapping-trough BALQ has been observed three times using SDSS, and is included in the Farrah et al. (2012) sample. It was first classified as an FeLoBAL quasar by Hall et al. (2002), and Hall et al. (2003) presented an analysis of the spectacular narrow Ca II absorption lines. Despite the heavy absorption, near-UV emission was detected by GALEX (Trammell et al. 2007). DiPompeo et al. (2011) reported spectropolarimetry observations; the continuum is modestly polarized (2%), but the emission and absorption lines do not show any different polarization. Vivek et al. (2012) obtained two additional spectra; they found no variability in the optically thickest portions of the outflow, but reported variability that may be associated with the optically thinner portion or the underlying continuum or line emission. McGraw et al. (2015) also investigated the variability in this object; they concluded that there is no variability in the BALs but tentative variability in the associated absorption lines. It was observed using *SCUBA-2* but was not detected (Violino et al. 2016). Villforth et al. (2019) presented near-IR imaging observations obtained using HST; the image was dominated by the PSF. Lawther et al. (2018) used HST to image the object in the UV, within the BAL troughs, and in the near-IR. They found that the host-galaxy properties are consistent with those of non-BAL quasars. Rogerson et al. (2011) observed this object with Chandra to study the X-ray absorption and constrained the lower limit for the column density of the X-ray absorbing gas to be $\log N_H \geqslant 24.3$ [cm^{-2}] with density $\log n \sim 6$ [cm^{-3}]. A twelve-bin tophat (single ionization parameter and single density) model with two-covering factors was used. We only fit the main Fe II trough and ignored the much narrower Ca II absorption lines that were observed at the lower-velocity end of the main overlapping trough. The physical constraints on the main Fe II trough from the best-fitting model are unaffected by this exclusion. Hall et al. (2003) concluded that the Ca II must have formed in a different region within the same BAL outflow gas with a significant temperature difference.

033810.84+005617.6 This object is included in the Farrah et al. (2012) sample, and has been observed five times by SDSS. It was first classified as an FeLoBAL quasar by Hall et al. (2002). It was detected in the near-UV by GALEX (Trammell et al. 2007). Spectropolarimetry observations (DiPompeo et al. 2011) revealed that it is unpolarized. A model with the nine-bin tophat bins (single ionization parameter and single density) and the general reddening law was used. The best-fitting *SimBAL* model found a Mg II trough spanning from $-43{,}300$ km s^{-1} to $-26{,}400$ km s^{-1}, exceeding that discovered in GQ 1309+2904, the previously discovered fastest LoBAL (Fynbo et al. 2020). We excluded this object from the analysis because we could not constrain the physical properties of the outflow gas since no other absorption line was found in the spectrum (also makes this object a LoBALQ instead of FeLoBALQ), and the BAL identification was uncertain due to the location of the trough in the region where strong Fe II emission is generally found.

080248.18+551328.8 This object was observed twice by SDSS, and was first classified as a BALQ by Gibson et al. (2009). Liu et al. (2015) reported He I* absorption in the SDSS spectrum. Yi et al. (2019) reported variability in the Mg II absorption line equivalent width with 3.4σ confidence. A five-bin tophat model (single ionization parameter and single density) was used.

080957.39+181804.4 This object was observed twice by SDSS, and is included in the DR14 SDSS quasar catalog (Pâris et al. 2018). Liu et al. (2015) reported He I* absorption in the SDSS spectrum. Villforth et al. (2019) presented near-IR imaging observations obtained using HST; the image is dominated by the PSF. A nine-bin tophat (single ionization parameter and single density) with two-covering model was used.

081312.61+432640.1 This object is included in the Farrah et al. (2012) sample, and has been observed three times by SDSS. It was first classified as an FeLoBAL quasar by Trump et al. (2006). Two Gaussian profiles were used to model the absorption feature, mainly following the shapes of the Mg II$\lambda\lambda$2796,2803 doublet lines. They were combined and analyzed as a single BAL outflow.

083522.77+424258.3 This object was discovered in the First Bright Quasar Survey (FBQS J083522.7+424258; White et al. 2000), and is included in the Farrah et al. (2012) sample. It has been observed three times by SDSS. The He I* absorption lines were noted by Liu et al. (2015). Vivek et al. (2012) reported no BAL variability over 5 years in the object's rest frame. Two Gaussian profiles were used based on the shape of the Mg II doublet lines. Only the lower-velocity Gaussian component of the two was used in the analysis because the other Gaussian component presented no Fe II lines. The Fe II and Mg II absorption lines as well as the He I*λ 3188 and He I*λ 3889 transitions in this object were well modeled with *SimBAL*. However, the model underpredicts the opacity for Ca II$\lambda\lambda$3934,3969 doublet lines as well as the Mg Iλ 2853 line.

084044.41+363327.8 This object was identified as a radio-loud BALQ in the FIRST Survey (FBQS J0840+3633; Becker et al. 1997), and is included in the Farrah et al. (2012) sample. It was observed by SDSS three times. It is highly polarized, with a complex polarization structure across the troughs (Brotherton et al. 1997). It was detected by Chandra, with inferred $\alpha_{ox} = 2.11$ (Green et al. 2001). de Kool et al. (2002a) performed a heroic, in-depth analysis of a Keck echelle spectrum. They found evidence for two absorption systems, with the higher-excitation one located ∼230 pc from the nucleus. Lewis et al. (2003) reported no detection in the submillimeter band from a *SCUBA* observation. Both Vivek et al. (2014) and McGraw et al. (2015) found that the broad absorption lines were not variable. A nine-bin tophat (single ionization parameter and single density) model with two-covering factors was used. Even though the absorber-velocity profile from our model encompasses both of the BAL components analyzed in de Kool et al. (2002a), we do not find compelling evidence for the two separate outflows from our low-resolution data.

091658.43+453441.1 This object was observed once using SDSS, and is included in the DR14 SDSS quasar catalog (Pâris et al. 2018). Two Gaussian profiles were used based on the shape of the Mg II doublet lines. One of the Gaussian profile components was added to model the weak absorption feature seen only in Mg II lines; thus this component was not included in the analysis.

091854.48+583339.6 This object is included in the Farrah et al. (2012) sample, and has been observed once by SDSS. It was first classified as an FeLoBAL quasar by Trump et al. (2006). It was detected in the near-UV by GALEX (Trammell et al. 2007). A single Gaussian model was used.

094404.25+500050.3 This object was observed once using SDSS, and is included in the DR14 SDSS quasar catalog (Pâris et al. 2018). It was identified as an FeLoBALQ using the convolutional neural network FeLoNET (C. Dabbieri et al. 2022, in preparation). The model included an eleven-bin tophat, the general reddening law, and a template spectrum for the long-wavelength region (∼4700 Å).

100605.66+051349.0 This object is included in the Farrah et al. (2012) sample, and has been observed once by SDSS. It was first classified as an FeLoBAL quasar by Trump et al. (2006). It was detected in the FIRST survey and has an unresolved core morphology (Kimball et al. 2011). An eight-bin tophat model (single ionization parameter and single density) was used.

101927.37+022521.4 This object is included in the Farrah et al. (2012) sample, and has been observed once by SDSS. It was first classified as an FeLoBAL quasar by Trump et al. (2006). It was detected in the FIRST survey and has a resolved core morphology (Kimball et al. 2011). Schulze et al. (2017) presented near-infrared observations of this object, determining that the rest-frame optical-band-based redshift is 1.364. The spectrum also shows substantial Balmer absorption from the BAL outflow (Schulze et al. 2018). A four-bin tophat model (single ionization parameter and single density) with a modified partial-covering was used. This object showed significant nonzero offset flux at the bottoms of the troughs, and we used a modified partial-covering model in which the emission lines and a fraction of continuum emission were not absorbed by the outflow. The width of absorption lines is not significantly larger than other objects (∼3000 km s^{-1}); nonetheless J1019+0225 may be classified as an overlapping trough FeLoBALQ as we see no continuum recovery around $\lambda \sim 2500$ Å due to the large opacity from the rare excited-state Fe II produced in the high-ionization and high-density gas. The kinematic properties (narrow width and small $v_{\rm off}$) combined with the compactness of the outflow ($\log R < 1$ [pc]) classify the BAL found in this object as a loitering outflow.

102036.10+602339.0 This object is included in the Farrah et al. (2012) sample, and has been observed twice by SDSS. It was first classified as an FeLoBAL quasar by Trump et al. (2006). Despite the heavy absorption, near-UV emission was detected by GALEX (Trammell et al. 2007). Liu et al. (2015) reported He I* absorption in the SDSS spectrum. Yi et al. (2019) found that the Mg II absorption line equivalent width did not vary between the two observations. Villforth et al. (2019) found that the host galaxy showed signs of disturbance in an HST near-IR image. A two-covering model with two sets of tophat bins with each group having a single ionization parameter and density was used. The higher-velocity group ($v_{\rm off} \sim -3900$ km s^{-1}) with 3 tophat bins produced most of the Fe II opacity needed to create the iron troughs found in the spectrum with $\log U \sim -1.9$ and $\log n \sim 7.6$ [cm^{-3}]. A lower-velocity group ($v_{\rm off} \sim -3100$ km s^{-1}) with 5 bins was needed to model the wide Mg II trough and deep Ca H+K and Mg I lines that were not sufficiently modeled with the higher-velocity group. Also, some of the deeper dips in the troughs (∼2300–2600 Å) required the opacity from the bins from the lower-velocity group. The lower-velocity group shows substantially lower-ionization parameter and density compared to the higher-velocity group ($\log U \sim -2.9$ and $\log n \sim 4.4$ [cm^{-3}]). From the above values, one can come to a conclusion that the two outflow components are separated by more than 2 dex in distance ($R \propto (1/nU)^{1/2}$). The FWHM of the emission model was fixed to a value determined from the long-wavelength part of the spectrum where the absorption is not severe ($\lambda \gtrsim 3000$ Å, FWHM ∼ 11000 km s^{-1}).

102226.70+354234.8 This object was observed twice by SDSS and is included in the DR14 SDSS quasar catalog (Pâris et al. 2018). A nine-bin tophat model (single ionization parameter and single density) was used.

102358.97+015255.8 This object is included in the Farrah et al. (2012) sample, and has been observed once by SDSS. It was first classified as an FeLoBAL quasar by Trump et al. (2006). A single Gaussian model was used.

103036.92+312028.8 This object was observed four times by SDSS and is included in the DR14 SDSS quasar catalog (Pâris et al. 2018). A model with a six-bin tophat (single ionization parameter and single density) and the general reddening law was used. We used a long-wavelength template spectrum to model this object to ∼4000 Å.

103903.03+395445.8 This object was observed once by SDSS and is included in the DR14 SDSS quasar catalog (Pâris et al. 2018). It was identified as an FeLoBALQ using the convolutional neural network FeLoNET (C. Dabbieri et al. 2022, in preparation). The model included two Gaussian opacity profiles, the general reddening law and a template spectrum for the long-wavelength region (∼4700 Å). Each Gaussian profile modeled one of the two BAL components that had a large velocity separation.

104459.60+365605.1 This object was discovered in the First Bright Quasar Survey (FBQS J104459.5+365605; Becker et al. 2000; White et al. 2000); Kimball et al. (2011) reported that the radio emission is unresolved. It has been observed three times by SDSS. A Keck High Resolution Echelle Spectrometer (HIRES) spectrum was analyzed in detail by de Kool et al. (2001); they found that the absorber is located ∼700 pc from the continuum source. DiPompeo et al. (2010) reported the detection of significant polarization that increases toward shorter wavelengths. Runnoe et al. (2013) observed the rest-frame optical spectrum; they report that for a Hβ FWHM of 3615 km s^{-1} and a log bolometric luminosity of 46.57 [erg s^{-1}], the log black hole mass is 8.87 [M$_\odot$], and the Eddington ratio is 0.33. While the Hβ FWHM and bolometric luminosity are similar, the other values are different than those obtained by Leighly et al. (2022) from the BOSS spectrum ($\log M_{BH} = 7.82$ [M$_\odot$] and $\log L_{\rm Bol}/L_{Edd} = 0.8$). McGraw et al. (2015) reported a tentative detection of absorption variability in the high-velocity LoBAL feature, but not in the FeLoBAL troughs modeled in this paper. Yi et al. (2019) also found evidence for variability. A thirteen-bin tophat was divided into two groups with each group having a single ionization parameter and single density. The model also included a long-wavelength template spectrum to model this object to ∼4000 Å. The higher-velocity group (−5500 to −4000 km s^{-1}) was composed of 6 tophat bins, and the lower-velocity group (−2600 to −640 km s^{-1}) used the remaining 7 tophat bins. de Kool et al. (2001) also found two velocity structures in this object; however, they did not treat them as two separate outflow components. Although not included in the best-fitting *SimBAL* model, the shallow absorption feature observed at $\lambda \sim 2650$ Å may be the Mg II absorption lines from a high-velocity LoBAL outflow.

105748.63+610910.8 This object was observed once using SDSS and is included in the Farrah et al. (2012) sample. It was first identified as an FeLoBALQ by Trump et al. (2006). This object was modeled with a single Gaussian opacity profile. The narrow absorption lines (FWHM ∼150 km s^{-1}) show full covering of the emission source, which is uncommon for quasar outflows, and an unusually high outflow velocity $v_{Off} \sim -9500$ km s^{-1}. The key spectral signatures of BAL outflows include the broad width of the absorption lines and partial coverage (e.g., Ganguly & Brotherton 2008). The absorption lines in this object, on the other hand, closely resemble the properties of an associated quasar absorber originating from a gas that is potentially located within the quasar host galaxy or its surrounding medium (Appendix D). In addition, this absorption system has been previously classified as an associated absorber in several catalogs (e.g., Quider et al. 2011; Chen et al. 2018); however, it is difficult to strictly differentiate between an outflow signature and an associated absorber; therefore we proceed with caution in analyzing this outflow. Although this object was included in Farrah et al. (2012), we excluded this BAL from the sample due to its ambiguous nature.

112526.12+002901.3 This object was featured in Hall et al. (2002) where they commented on the He I$^*\lambda$ 3889 and Ca II H&K absorption lines, as well as the low covering fraction and high-excitation Fe II lines. Hall et al. (2013) discussed the redshifted absorption found in this object and a handful of other BAL outflows. Shi et al. (2016) compared the SDSS and BOSS spectra, and determined that variability between the two arises from a change in broad line emission, which is not absorbed by the compact outflow in this object. Zhang et al. (2017) reported the X-ray detection in a 3.8 ks Chandra observation; the object is 34.1 times X-ray weaker than an unabsorbed quasar. Near-IR observations obtained using HST revealed that the image is dominated by the PSF (Villforth et al. 2019). A four-bin tophat (single ionization parameter and single density) and a Gaussian opacity profile model were used. We also used a modified partial-covering model in which the emission lines and a fraction of continuum emission were not absorbed by the outflow. The principal Fe II opacity was modeled by the tophat component, and the Gaussian component provided the extra opacity needed to create the deep Mg II absorption trough. This additional Gaussian component was allowed to freely absorb the emission lines and the continuum emission, unlike the main tophat component.

112828.31+011337.9 This object is identified as an FeLoBALQ by Hall et al. (2002). Hall et al. (2013) discussed the redshifted absorption also found in this object. Yi et al. (2019) found evidence for variability among the three SDSS observations. Zhang et al. (2017) reported the results of a 5.4 ks Chandra observation; the object was not detected, implying that it is more than 50 times weaker than a comparable unabsorbed object. Near-IR observations obtained using HST revealed a resolved target with a somewhat disturbed morphology (Villforth et al. 2019). An eight-bin tophat (single ionization parameter and single density) model was used. The line emission is unabsorbed by the BAL in this model, and we used a long-wavelength template spectrum to model this object to ∼4000 Å.

112901.71+050617.0 This object was first classified as an FeLoBALQ by Trump et al. (2006). It was detected by the FIRST survey and has an unresolved core morphology (Kimball et al. 2011). No variability was detected between two SDSS observations (Yi et al. 2019). An eight-bin tophat (single ionization parameter and single density) model with two-covering factors was used.

114556.25+110018.4 This object is included in the Farrah et al. (2012) sample, and was observed once by SDSS. It was first classified as an FeLoBALQ by Trump et al. (2006). A single Gaussian opacity model was used. The line emission is unabsorbed by the BAL, and no reddening component was included in the model.

115436.60+030006.3 This spectacular overlapping-trough FeLoBALQ was first identified by Hall et al. (2002). It has been observed twice by SDSS and was included in the Farrah et al. (2012) sample. McGraw et al. (2015) did not observe variability among three observations, including one taken at MDM observatory. A model with a seven-bin tophat and the general reddening law was used. All bins were constrained to have a single-density parameter but the three highest-velocity bins were group together and allowed to have a different ionization parameter than the rest of the four lower-velocity bins. It has one of the highest outflow velocities ($v_{\rm off} \sim -15{,}400$ km s^{-1}; $v_{max} \sim -17{,}000$ km s^{-1}) in the sample and also shows anomalous reddening.

115852.86–004301.9 This object was first classified as an FeLoBAL quasar by Trump et al. (2006). It has been observed twice by SDSS. It was detected in the FIRST Survey; Kimball et al. (2011) reported a jet with a recognizable morphology with a 21 cm flux density of 87 mJy. A five-bin tophat (single ionization parameter and single density) model was used.

120049.54+632211.8 This object was first classified as an FeLoBAL quasar by Trump et al. (2006), and it is included in the Farrah et al. (2012) sample. It has been observed four times by SDSS, but no variability was found (Yi et al. 2019). A twelve-bin tophat (single ionization parameter and single density) model with two-covering factors was used.

120627.62+002335.4 This object was first classified as an FeLoBAL quasar by Trump et al. (2006), and is included in the Farrah et al. (2012) sample. It has been observed once by SDSS. Hutsemékers et al. (2017) reported that the object is significantly polarized at 1.7% ± 0.36%. The model included an eight-bin tophat that is divided into two groups (single ionization parameter and single density per group), the general reddening law and a template spectrum for the long-wavelength region (∼4400 Å). The principal Fe II opacity was modeled by the higher-velocity group (-6800 to -1900 km s^{-1}) with 4 tophat bins, and the lower-velocity group (-5600 to -300 km s^{-1}) used the remaining 4 tophat bins.

120815.03+624046.4 This object has been observed once by SDSS, and is included in the DR14 SDSS quasar catalog (Pâris et al. 2018). It was identified as an FeLoBALQ using the convolutional neural network FeLoNET (C. Dabbieri et al. 2022, in preparation). A single Gaussian opacity model was used. A long-wavelength template spectrum was included to model this object to ∼4400 Å.

121231.47+251429.1 This object has been observed once by SDSS, and is included in the DR14 SDSS quasar catalog (Pâris et al. 2018). It was identified as an FeLoBALQ using the convolutional neural network FeLoNET (C. Dabbieri et al. 2022, in preparation). A single Gaussian opacity model was used. A long-wavelength template spectrum was included to model this object to ∼4700 Å.

121441.42−000137.8 A nine-bin tophat (single ionization parameter and single density) and a Gaussian opacity profile model were used. A long-wavelength template spectrum was included to model this object to ∼4500 Å. The extremely broad tophat component seen in the Mg II trough that extends from -18000 to -6200 km s^{-1} was excluded in the analysis. No substantial Fe II opacity or other absorption lines were observed from this component, and we could not extract robust physical constraints from only the Mg II trough. Moreover, the continuum placement near the assumed wavelength region where the troughs from the Fe II are expected was highly uncertain due to the Fe II emission lines. Pitchford et al. (2019) observed this object in the mid-infrared to study the star formation property of the quasar and found that this object has the highest star formation rate among FeLoBALQs ($\sim 2000\, M_{\odot} yr^{-1}$).

121442.30+280329.1 This object was discovered in the First Bright Quasar Survey (FBQS J1214+2803; Becker et al. 2000; White et al. 2000). It has been observed twice by SDSS. A Keck HIRES spectrum was analyzed in detail by de Kool et al. (2002b). They found that the absorber is located between 1 and 30 parsecs from the continuum source. Branch et al. (2002) and Casebeer et al. (2008) presented an alternative resonance-scattering interpretation of the spectrum. DiPompeo et al. (2010) found a low continuum polarization (0.4% ± 0.13%). Zhang et al. (2017) found no evidence for variability between the two SDSS spectra, but McGraw et al. (2015) found significant variability among several MDM observations. An eight-bin tophat (single ionization parameter and single density) model with two-covering factors was used. The outflow properties measured by de Kool et al. (2002b) ($-2.0 < \log U < -0.7$, $7.5 < \log n < 9.5$ [cm^{-3}], and $21.4 < \log N_H < 22.2$ [cm^{-2}]) were consistent with the values that we got from our best-fitting *SimBAL* model ($\log U = -1.7^{+0.002}_{-0.001}$, $\log n = 7.8^{+0.005}_{-0.006}$ [cm^{-3}] $\log N_H = 22.0 \pm 0.003$ [cm^{-2}]).

123549.95+013252.6 This object was first classified as an FeLoBAL quasar by Trump et al. (2006), and is included in the Farrah et al. (2012) sample. It has been observed once by SDSS. It was observed using *SCUBA-2* but was not detected (Violino et al. 2016). An eight-bin tophat (single ionization parameter and single density) model was used. A long-wavelength template spectrum was included to model this object to ∼4000 Å.

124014.04+444353.4 This object was originally classified as a type 2 quasar (Yuan et al. 2016). It is actually a Seyfert 1.8, as a faint and broad Hβ line can be seen in the sole SDSS spectrum (Leighly et al. 2022). It was identified as an FeLoBALQ using the convolutional neural network FeLoNET (C. Dabbieri et al. 2022, in preparation). A six-bin tophat (single ionization parameter and single density) model was used. A long-wavelength template spectrum was included to model this object to ∼4700 Å.

132117.24+561724.5 This object was observed once by SDSS and is included in the DR14 SDSS quasar catalog (Pâris et al. 2018). It was identified as an FeLoBALQ using the convolutional neural network FeLoNET (C. Dabbieri et al. 2022, in preparation). A two-bin tophat (single ionization parameter and single density) model was used. The line emission is unabsorbed by the BAL in this model, and we used a long-wavelength template spectrum to model this object to ∼4400 Å.

132401.53+032020.5 This object was first classified as an FeLoBAL quasar by Trump et al. (2006), and is included in the Farrah et al. (2012) sample. Liu et al. (2015) observed He I* absorption in the SDSS spectrum. Young et al. (2009) reported a serendipitous X-ray detection with signal-to-noise ratio of 5.8 that yields an $\alpha_{ox} = -1.85$. Yi et al. (2019) found no variability between the two SDSS observations. An eight-bin tophat (single ionization parameter and single density) and a Gaussian opacity profile model were used. A long-wavelength template spectrum was included to model this object to ∼4400 Å. An additional Gaussian component was included to model the narrow intervening absorber at $-21{,}000$ km s^{-1} relative to the quasar rest frame; this component was excluded from the analysis.

133632.45+083059.9 This object was observed twice by SDSS and is included in the DR14 SDSS quasar catalog (Pâris et al. 2018). This object was classified as an unusual BAL quasar by Meusinger et al. (2012). It was identified as an FeLoBALQ using the convolutional neural network FeLoNET (C. Dabbieri et al. 2022, in preparation). A nine-bin tophat (single ionization parameter and single density) model was used. A long-wavelength template spectrum was included to model this object to ∼4700 Å. A strong degeneracy between the power-law slope and the reddening was observed in the *SimBAL* model, so we used the composite SED from Richards et al. (2006) with a normalization parameter in place of the power-law continuum model to eliminate the slope parameter.

135525.24+575312.7 This object was observed once by SDSS and is included in the DR14 SDSS quasar catalog (Pâris et al. 2018). This object was identified as an FeLoBALQ by visual examination. An eight-bin tophat (single ionization parameter and single density) model was used. A long-wavelength template spectrum was included to model this object to ∼4400 Å.

135640.34+452727.2 This object was observed once by SDSS and is included in the DR14 SDSS quasar catalog (Pâris et al. 2018). A nine-bin tophat and a Gaussian opacity profile model were used. The tophat bins and the Gaussian component were modeling a single BAL component together, so they were given a single ionization parameter and single density. A long-wavelength template spectrum was included to model this object to ∼4700 Å.

142703.62+270940.4 This object was discovered in the First Bright Quasar Survey (FBQS J142703.6+270940; Becker et al. 2000; White et al. 2000). DiPompeo et al. (2010) found significant continuum polarization of about 2% that rises toward short wavelengths. The model included a nine-bin tophat that is divided into two groups (single ionization parameter and single density per group), the general reddening law and a template spectrum for the long-wavelength region (∼4700 Å). The higher-velocity group (-3700 to $-2800\,\mathrm{km\,s^{-1}}$) was composed of 3 tophat bins, and the lower-velocity group (-1100 to $90\,\mathrm{km\,s^{-1}}$) used the remaining 6 tophat bins. The FWHM of the emission model was fixed to a value determined from the long-wavelength part of the spectrum where the absorption is not severe ($\lambda \gtrsim 3000$ Å, FWHM $\sim 5000\,\mathrm{km\,s^{-1}}$).

144800.15+404311.7 This spectacular overlapping-trough object was first classified as a BALQ by Gibson et al. (2009). Villforth et al. (2019) presented near-IR imaging observations obtained using HST; the image was dominated by the PSF. It has been observed three times by SDSS. The model included an eight-bin tophat that is divided into two groups (single ionization parameter and single density per group) and an extra Gaussian component with both using two-covering factors, the general reddening law and a template spectrum for the long-wavelength region (∼4700 Å). The higher-velocity group (-6900 to $-2400\,\mathrm{km\,s^{-1}}$) was composed of 4 tophat bins, and the lower-velocity group (-5000 to $-710\,\mathrm{km\,s^{-1}}$) used the remaining 4 tophat bins. The additional Gaussian component at $\sim -600\,\mathrm{km\,s^{-1}}$ was required for the narrow outflow component that was identified by the narrow Mg I and Ca II H and K absorption lines.

151708.94+232857.5 This object was observed once by SDSS and is included in the DR14 SDSS quasar catalog (Pâris et al. 2018). It was identified as an FeLoBALQ using the convolutional neural network FeLoNET (C. Dabbieri et al. 2022, in preparation). A seven-bin tophat (single ionization parameter and single density) with two-covering model was used. A long-wavelength template spectrum was included to model this object to ∼4700 Å.

152737.17+591210.1 This object was observed once by SDSS and is included in the DR14 SDSS quasar catalog (Pâris et al. 2018). The model included a seven-bin tophat, the general reddening law and a template spectrum for the long-wavelength region (∼4700 Å).

153145.01+485257.2 It was identified as an FeLoBALQ using the convolutional neural network FeLoNET (C. Dabbieri et al. 2022, in preparation). Three Gaussian profiles were used in the model. Only one of the Gaussian components was included in the analysis because the other two Gaussian components were included to model a narrow intervening system at $\sim -23000\,\mathrm{km\,s^{-1}}$ relative to the quasar rest frame and for a weak Mg II opacity structure near rest velocity.

155633.77+351757.3 This object was identified as a radio-loud BALQ in the FIRST Survey (FIRST J155633.8+351758; Becker et al. 1997), and is included in the Farrah et al. (2012) sample. It was observed by SDSS three times. It is highly polarized, up to ∼10% at short wavelengths, with lower polarization and complex structure across the deepest troughs (Brotherton et al. 1997). Najita et al. (2000) presented a near-infrared spectrum; they found strong Balmer lines and Fe II emission, and a Balmer-line-based redshift of $z = 1.5008 \pm 0.0007$. Lewis et al. (2003) found that the object was not detected in the submillimeter band using *SCUBA*. Brotherton et al. (2005) reported results of a Chandra observation; 40 photons were detected, and they suggest that the X-ray emission was suppressed by a absorption by a factor of 49. A second longer Chandra observation netted 531 photons (Berrington et al. 2013); a heavily absorbed spectrum could be ruled out, and a partial-covering model was favored. Jiang & Wang (2003) performed European VLBI Network observations at 1.6 GHz; they found that the object is unresolved at 20 mas, and inferred a flat spectrum. Yi et al. (2019) reported no variability between the first two SDSS observations. The model included a nine-bin tophat that is divided into two groups (single ionization parameter and single density per group) with two-covering, the general reddening law and a template spectrum for the long-wavelength region (∼4100 Å). The higher-velocity group (-9000 to $-5600\,\mathrm{km\,s^{-1}}$) was composed of 4 tophat bins, and the lower-velocity group (-5500 to $-1400\,\mathrm{km\,s^{-1}}$) used the remaining 5 tophat bins.

164419.75+530750.4 This object was first categorized as a QSO by Popescu et al. (1996). It was observed once by SDSS and is included in the DR14 SDSS quasar catalog (Pâris et al. 2018). It was identified as an FeLoBAL quasar by visual inspection. A six-bin tophat (single ionization parameter and single density) and a Gaussian opacity profile model were used. We also used a modified partial-covering model in which the emission lines and a fraction of continuum emission were not absorbed by the outflow. The Gaussian component was excluded from the sample because it only produced Mg II opacity, and thus we could not constrain the physical properties of that outflow component.

173753.97+553604.9 This object was first identified as an FeLoBALQ by Trump et al. (2006), and it is included in the Farrah et al. (2012) sample. It was observed once by SDSS. We did not find any absorption features in this object, and therefore we excluded this object from the analysis.

210712.77+005439.4 This object was first identified as an FeLoBALQ by Trump et al. (2006), and it is included in the Farrah et al. (2012) sample. It was observed once by SDSS. It was observed using *SCUBA-2* but was not detected (Violino et al. 2016). An eight-bin tophat (single ionization parameter and single density) model was used. A long-wavelength template spectrum was included to model this object to ∼4700 Å.

213537.44–032054.8 This object was observed once by SDSS and is included in the DR14 SDSS quasar catalog (Pâris et al. 2018). It was identified as a BALQ in the DR10 SDSS quasar catalog (Pâris et al. 2014). A six-bin tophat (single ionization parameter and single density) model was used. A long-wavelength template spectrum was included to model this object to ~4400 Å.

230730.69+111908.5 This object was observed once by SDSS and is included in the DR14 SDSS quasar catalog (Pâris et al. 2018). A five-bin tophat and a Gaussian opacity profile model were used. The tophat bins and the Gaussian component were modeling a single BAL component together, so they were given a single ionization parameter and single density. A long-wavelength template spectrum was included to model this object to ~4100 Å.

Appendix D
Intervening Absorbers

The intrinsic quasar absorption lines (e.g., BAL) have five main spectroscopic characteristic that are not seen in intervening absorbers: (1) wider absorption lines, (2) partial coverage of the emission source, (3) time variability of the troughs, (4) higher ionization parameter, and (5) higher metallicity (e.g., Barlow & Sargent 1997; Ganguly & Brotherton 2008). Therefore, BALs that show narrow and deep features could easily be confused with intervening absorbers. In order to systematically check whether we could differentiate the intervening absorbers from BALs using *SimBAL*, we fit 20 quasar spectra that were identified to have intervening absorption features. The objects were drawn from the intervening Mg II quasar absorption line catalog by Quider et al. (2011), and we chose objects that have the similar redshift range ($1 < z < 1.5$). We then selected the ones that have Mg II absorbers located close to the background quasar ($z_{qso} \sim z_{abs}$) because these objects have the spectral features that most closely resemble BAL spectra. The spectra of these objects show Mg II absorption lines near $\lambda_{rest} \sim 2750$ Å that could be confused with quasar-driven BAL or associated absorption-line (AAL; e.g., Hamann et al. 2011).

Figure 25 shows the distributions of physical and kinematic parameters of the intervening absorption lines and the FeLoBALs, both obtained from *SimBAL* modeling. The distributions of physical parameters (e.g., ionization parameter and density) do not show a clear distinction between the intervening absorbers and FeLoBALs. However, most of the intervening absorbers were constrained to have an extremely low density ($\log n \lesssim 3$ [cm^{-3}]). The kinematic properties of the absorption line systems showed the clearest difference between the intervening Mg II absorbers and FeLoBALs. The intervening absorption lines have narrower widths and higher offset velocities than the majority of FeLoBALs in the sample. We note that accurate modeling of intervening absorbers requires photoionization calculations using the correct photoionzing SED. For this experiment, we used the same ionic column density grid used with FeLoBALQs that was generated with quasar SED, which may have a different shape than the photoionizing SEDs required for the intervening absorption line gas. Nevertheless, we conclude that the intervening absorption systems could be identified by examining the kinematic properties of the absorption lines, in particular the width of the lines. This result implies that intervening absorbers will be easily excluded in data from the upcoming missions that will provide better spectral resolution, such as 4MOST (de Jong et al. 2019).

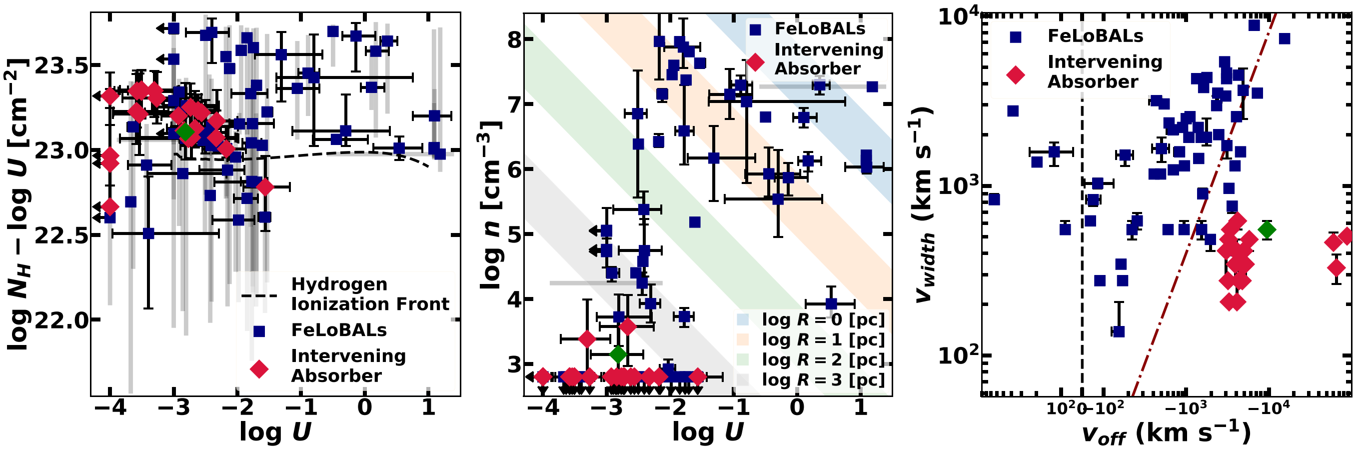

Figure 25. *Left panel*: the physical parameter distribution of intervening absorbers cannot be easily differentiated from that of FeLoBAL. *Middle panel*: intervening absorbers have low densities, and we were able to constrain only the density upper limits ($\log n \lesssim 2.8$ [cm^{-3}]) for the majority of them. Based on the ionization parameter and the density, we found the inferred distances from the central engine to the intervening absorber gas to be $\log R \gtrsim 3$ [pc], if we assume the radiation from AGN as the ionizing source for these absorbers. *Right panel*: the kinematic properties show the clearest distinction between the intervening absorbers and FeLoBALs. The intervening absorbers have very narrow width ($v_{\rm width} \lesssim 200$ km s^{-1}) and disproportionately large offset velocities ($v_{\rm off} \ll -3,000$ km s^{-1}), relative to the quasar rest frame, compared to FeLoBALs. The brown dotted–dashed line shows a one-to-one ratio. We rejected SDSS J1057+6109 (green diamonds) from the analysis because the properties of the absorption feature seen in the spectra better resembled the intervening absorbers than the quasar-driven outflows (Section 3.3.1). A linear scale was used in the region $|v_{\rm off}| < 100$ km s^{-1}, and log scale was used elsewhere in the x-axis. The error bars show 95% uncertainties, and the gray shaded bars represent the range of the values among the tophat model bins for each BAL.

ORCID iDs

Hyunseop Choi (최현섭) https://orcid.org/0000-0002-3173-1098
Karen M. Leighly https://orcid.org/0000-0002-3809-0051
Donald M. Terndrup https://orcid.org/0000-0002-0431-1645
Sarah C. Gallagher https://orcid.org/0000-0001-6217-8101
Gordon T. Richards https://orcid.org/0000-0002-1061-1804

References

Anderson, S. F., Margon, B., Voges, W., et al. 2007, AJ, 133, 313
Aoki, K., Oyabu, S., Dunn, J. P., et al. 2011, PASJ, 63, 457
Arav, N., Borguet, B., Chamberlain, C., Edmonds, D., & Danforth, C. 2013, MNRAS, 436, 3286
Arav, N., Brotherton, M. S., Becker, R. H., et al. 2001, ApJ, 546, 140
Arav, N., Kaastra, J., Kriss, G. A., et al. 2005, ApJ, 620, 665
Arav, N., & Li, Z.-Y. 1994, ApJ, 427, 700
Arav, N., Li, Z.-Y., & Begelman, M. C. 1994, ApJ, 432, 62
Arav, N., Liu, G., Xu, X., et al. 2018, ApJ, 857, 60
Arav, N., Moe, M., Costantini, E., et al. 2008, ApJ, 681, 954
Bailey, S. 2012, PASP, 124, 1015
Barlow, T. A., & Sargent, W. L. W. 1997, AJ, 113, 136
Bautista, M. A., Dunn, J. P., Arav, N., et al. 2010, ApJ, 713, 25
Becker, R. H., Gregg, M. D., Hook, I. M., et al. 1997, ApJL, 479, L93
Becker, R. H., White, R. L., Gregg, M. D., et al. 2000, ApJ, 538, 72
Berrington, R. C., Brotherton, M. S., Gallagher, S. C., et al. 2013, MNRAS, 436, 3321
Blanton, M. R., Bershady, M. A., Abolfathi, B., et al. 2017, AJ, 154, 28
Boksenberg, A., Carswell, R. F., Allen, D. A., et al. 1977, MNRAS, 178, 451
Borguet, B., & Hutsemékers, D. 2010, A&A, 515, A22
Branch, D., Leighly, K. M., Thomas, R. C., & Baron, E. 2002, ApJL, 578, L37
Brotherton, M. S., Laurent-Muehleisen, S. A., Becker, R. H., et al. 2005, AJ, 130, 2006
Brotherton, M. S., Tran, H. D., van Breugel, W., Dey, A., & Antonucci, R. 1997, ApJL, 487, L113
Bruni, G., Piconcelli, E., Misawa, T., et al. 2019, A&A, 630, A111
Calistro Rivera, G., Alexander, D. M., Rosario, D. J., et al. 2021, A&A, 649, A102
Capellupo, D. M., Hamann, F., Shields, J. C., Halpern, J. P., & Barlow, T. A. 2013, MNRAS, 429, 1872
Capellupo, D. M., Hamann, F., Shields, J. C., Rodríguez Hidalgo, P., & Barlow, T. A. 2011, MNRAS, 413, 908
Casebeer, D., Baron, E., Leighly, K., Jevremovic, D., & Branch, D. 2008, ApJ, 676, 857
Castor, J. I., Abbott, D. C., & Klein, R. I. 1975, ApJ, 195, 157
Chan, C.-H., & Krolik, J. H. 2016, ApJ, 825, 67
Chan, C.-H., & Krolik, J. H. 2017, ApJ, 843, 58
Chen, Z.-F., Huang, W.-R., Pang, T.-T., et al. 2018, ApJS, 235, 11
Choi, E., Ostriker, J. P., Naab, T., & Johansson, P. H. 2012, ApJ, 754, 125
Choi, H., Leighly, K. M., Terndrup, D. M., et al. 2022, ApJ, 936, 110
Choi, H., Leighly, K. M., Terndrup, D. M., Gallagher, S. C., & Richards, G. T. 2020, ApJ, 891, 53
Cicone, C., Maiolino, R., Sturm, E., et al. 2014, A&A, 562, A21
Dabbieri, C., Leighly, K., & Richards, G. 2020, AAS Meeting, 236, 238.03
Dai, X., Shankar, F., & Sivakoff, G. R. 2008, ApJ, 672, 108
Dai, X., Shankar, F., & Sivakoff, G. R. 2012, ApJ, 757, 180
Dawson, K. S., Kneib, J.-P., Percival, W. J., et al. 2016, AJ, 151, 44
Dawson, K. S., Schlegel, D. J., Ahn, C. P., et al. 2013, AJ, 145, 10
de Jong, R. S., Agertz, O., Berbel, A. A., et al. 2019, Msngr, 175, 3
de Kool, M., Arav, N., Becker, R. H., et al. 2001, ApJ, 548, 609
de Kool, M., Becker, R. H., Arav, N., Gregg, M. D., & White, R. L. 2002a, ApJ, 570, 514
de Kool, M., Becker, R. H., Gregg, M. D., White, R. L., & Arav, N. 2002b, ApJ, 567, 58
de Kool, M., Korista, K. T., & Arav, N. 2002c, ApJ, 580, 54
Di Matteo, T., Springel, V., & Hernquist, L. 2005, Natur, 433, 604
DiPompeo, M. A., Brotherton, M. S., Becker, R. H., et al. 2010, ApJS, 189, 83
DiPompeo, M. A., Brotherton, M. S., & De Breuck, C. 2011, ApJS, 193, 9
Dunn, J. P., Bautista, M., Arav, N., et al. 2010, ApJ, 709, 611
Dunn, J. P., Wasik, B., Holtzclaw, C. L., et al. 2015, ApJ, 808, 94
Elitzur, M., & Shlosman, I. 2006, ApJL, 648, L101
Elvis, M., Marengo, M., & Karovska, M. 2002, ApJL, 567, L107
Everett, J., Königl, A., & Arav, N. 2002, ApJ, 569, 671
Fabian, A., Ricci, C., & Ishibashi, W. 2018, COSPAR Scientific Assembly, 42, E1.13–29–18
Fabian, A. C. 2012, ARA&A, 50, 455
Fabian, A. C., Vasudevan, R. V., & Gandhi, P. 2008, MNRAS, 385, L43
Farrah, D., Urrutia, T., Lacy, M., et al. 2012, ApJ, 745, 178
Faucher-Giguère, C.-A., Quataert, E., & Murray, N. 2012, MNRAS, 420, 1347
Ferland, G. J., Chatzikos, M., Guzmán, F., et al. 2017, RMxAA, 53, 385
Ferland, G. J., Porter, R. L., van Hoof, P. A. M., et al. 2013, RMxAA, 49, 137
Finn, C. W., Morris, S. L., Crighton, N. H. M., et al. 2014, MNRAS, 440, 3317
Fiore, F., Feruglio, C., Shankar, F., et al. 2017, A&A, 601, A143
Foltz, C. B., Weymann, R. J., Morris, S. L., & Turnshek, D. A. 1987, ApJ, 317, 450
Foreman, G., Volonteri, M., & Dotti, M. 2009, ApJ, 693, 1554
Foreman-Mackey, D., Hogg, D. W., Lang, D., & Goodman, J. 2013, PASP, 125, 306
Francis, P. J., Hewett, P. C., Foltz, C. B., & Chaffee, F. H. 1992, ApJ, 398, 476
Freeman, P., Doe, S., & Siemiginowska, A. 2001, Proc. SPIE, 4477, 76
Fynbo, J. P. U., Krogager, J. K., Venemans, B., et al. 2013, ApJS, 204, 6
Fynbo, J. P. U., Møller, P., Heintz, K. E., et al. 2020, A&A, 634, A111
Gallagher, S. C., Brandt, W. N., Chartas, G., et al. 2006, ApJ, 644, 709
Gallagher, S. C., Brandt, W. N., Chartas, G., & Garmire, G. P. 2002, ApJ, 567, 37
Gallagher, S. C., Everett, J. E., Abado, M. M., & Keating, S. K. 2015, MNRAS, 451, 2991
Gallagher, S. C., Hines, D. C., Blaylock, M., et al. 2007a, ApJ, 665, 157
Gallagher, S. C., Richards, G. T., Lacy, M., et al. 2007b, ApJ, 661, 30
Ganguly, R., & Brotherton, M. S. 2008, ApJ, 672, 102
Ganguly, R., Brotherton, M. S., Cales, S., et al. 2007, ApJ, 665, 990
Gibson, R. R., Jiang, L., Brandt, W. N., et al. 2009, ApJ, 692, 758
Giustini, M., & Proga, D. 2019, A&A, 630, A94
Glikman, E. 2017, RNAAS, 1, 48
Glikman, E., Lacy, M., LaMassa, S., et al. 2018, ApJ, 861, 37
Green, P. J., Aldcroft, T. L., Mathur, S., Wilkes, B. J., & Elvis, M. 2001, ApJ, 558, 109
Green, R. F., Schmidt, M., & Liebert, J. 1986, ApJS, 61, 305
Hall, P. B. 2007, AJ, 133, 1271
Hall, P. B., Anderson, S. F., Strauss, M. A., et al. 2002, ApJS, 141, 267
Hall, P. B., Anosov, K., White, R. L., et al. 2011, MNRAS, 411, 2653
Hall, P. B., Brandt, W. N., Petitjean, P., et al. 2013, MNRAS, 434, 222
Hall, P. B., Hutsemékers, D., Anderson, S. F., et al. 2003, ApJ, 593, 189
Hamann, F. 1998, ApJ, 500, 798
Hamann, F., Chartas, G., McGraw, S., et al. 2013, MNRAS, 435, 133
Hamann, F., Herbst, H., Paris, I., & Capellupo, D. 2019a, MNRAS, 483, 1808
Hamann, F., Kanekar, N., Prochaska, J. X., et al. 2011, MNRAS, 410, 1957
Hamann, F., Tripp, T. M., Rupke, D., & Veilleux, S. 2019b, MNRAS, 487, 5041
Hamann, F., Zakamska, N. L., Ross, N., et al. 2017, MNRAS, 464, 3431
Hamann, F. W., Barlow, T. A., Chaffee, F. C., Foltz, C. B., & Weymann, R. J. 2001, ApJ, 550, 142
Harrison, C. M., Alexander, D. M., Mullaney, J. R., & Swinbank, A. M. 2014, MNRAS, 441, 3306
Hewett, P. C., & Foltz, C. B. 2003, AJ, 125, 1784
Hewett, P. C., & Wild, V. 2010, MNRAS, 405, 2302
Hönig, S. F., & Kishimoto, M. 2017, ApJL, 838, L20
Hönig, S. F., Kishimoto, M., Tristram, K. R. W., et al. 2013, ApJ, 771, 87
Hopkins, P. F., & Elvis, M. 2010, MNRAS, 401, 7
Hopkins, P. F., Hernquist, L., Cox, T. J., et al. 2005, ApJ, 630, 705
Hutsemékers, D., Hall, P., & Sluse, D. 2017, A&A, 606, A101
Ishibashi, W., Banerji, M., & Fabian, A. C. 2017, MNRAS, 469, 1496
Ishibashi, W., & Fabian, A. C. 2018, MNRAS, 481, 4522
Isobe, T., Feigelson, E. D., & Nelson, P. I. 1986, ApJ, 306, 490
Jiang, D. R., & Wang, T. G. 2003, A&A, 397, L13
Keating, S. K., Everett, J. E., Gallagher, S. C., & Deo, R. P. 2012, ApJ, 749, 32
Kelly, B. C. 2007, ApJ, 665, 1489
Kimball, A. E., Ivezić, Ž., Wiita, P. J., & Schneider, D. P. 2011, AJ, 141, 182
King, A. 2003, ApJL, 596, L27
King, A., & Pounds, K. 2015, ARA&A, 53, 115
King, A. R., & Pounds, K. A. 2003, MNRAS, 345, 657
King, A. R., Zubovas, K., & Power, C. 2011, MNRAS, 415, L6
Klindt, L., Alexander, D. M., Rosario, D. J., Lusso, E., & Fotopoulou, S. 2019, MNRAS, 488, 3109
Knigge, C., Scaringi, S., Goad, M. R., & Cottis, C. E. 2008, MNRAS, 386, 1426
Korista, K. T., Bautista, M. A., Arav, N., et al. 2008, ApJ, 688, 108
Krawczyk, C. M., Richards, G. T., Gallagher, S. C., et al. 2015, AJ, 149, 203

Krogager, J. K., Fynbo, J. P. U., Heintz, K. E., et al. 2016, ApJ, 832, 49
Krogager, J. K., Geier, S., Fynbo, J. P. U., et al. 2015, ApJS, 217, 5
Krolik, J. H., & Voit, G. M. 1998, ApJL, 497, L5
Laor, A., & Brandt, W. N. 2002, ApJ, 569, 641
Laor, A., & Draine, B. T. 1993, ApJ, 402, 441
Lawther, D., Vestergaard, M., & Fan, X. 2018, MNRAS, 475, 3213
Leighly, K., Marrs, A., Wagner, C., & Macinnis, F. 2017, AAS Meeting, 229, 250.16
Leighly, K. M., Choi, H., DeFrancesco, C., et al. 2022, ApJ, 935, 92
Leighly, K. M., Cooper, E., Grupe, D., Terndrup, D. M., & Komossa, S. 2015, ApJL, 809, L13
Leighly, K. M., Dietrich, M., & Barber, S. 2011, ApJ, 728, 94
Leighly, K. M., Hamann, F., Casebeer, D. A., & Grupe, D. 2009, ApJ, 701, 176
Leighly, K. M., & Moore, J. R. 2006, ApJ, 644, 748
Leighly, K. M., Terndrup, D. M., Baron, E., et al. 2014, ApJ, 788, 123
Leighly, K. M., Terndrup, D. M., Gallagher, S. C., Richards, G. T., & Dietrich, M. 2018, ApJ, 866, 7
Leighly, K. M., Terndrup, D. M., Lucy, A. B., et al. 2019, ApJ, 879, 27
Lewis, G. F., Chapman, S. C., & Kuncic, Z. 2003, ApJL, 596, L35
Liu, W.-J., Zhou, H., Ji, T., et al. 2015, ApJS, 217, 11
Lucy, A. B., Leighly, K. M., Terndrup, D. M., Dietrich, M., & Gallagher, S. C. 2014, ApJ, 783, 58
MacInnis, F. 2018, Master's thesis, Univ. Oklahoma
Maiolino, R., Oliva, E., Ghinassi, F., et al. 2004, A&A, 420, 889
Marrs, A., Leighly, K., Wagner, C., & Macinnis, F. 2017, AAS Meeting, 229, 250.14
McGraw, S. M., Shields, J. C., Hamann, F. W., et al. 2015, MNRAS, 453, 1379
McLeod, C., Leighly, K., & Kerr, A. 2020, AAS Meeting, 236, 334.01
Meusinger, H., Schalldach, P., Mirhosseini, A., & Pertermann, F. 2016, A&A, 587, A83
Meusinger, H., Schalldach, P., Scholz, R. D., et al. 2012, A&A, 541, A77
Miller, T. R., Arav, N., Xu, X., & Kriss, G. A. 2020, MNRAS, 499, 1522
Moe, M., Arav, N., Bautista, M. A., & Korista, K. T. 2009, ApJ, 706, 525
Morabito, L. K., Matthews, J. H., Best, P. N., et al. 2019, A&A, 622, A15
Morris, S. L., Weymann, R. J., Anderson, S. F., et al. 1991, AJ, 102, 1627
Murray, N., Quataert, E., & Thompson, T. A. 2005, ApJ, 618, 569
Najita, J., Dey, A., & Brotherton, M. 2000, AJ, 120, 2859
Nenkova, M., Sirocky, M. M., Nikutta, R., Ivezić, Ž., & Elitzur, M. 2008, ApJ, 685, 160
Pâris, I., Petitjean, P., Aubourg, É., et al. 2014, A&A, 563, A54
Pâris, I., Petitjean, P., Aubourg, É., et al. 2018, A&A, 613, A51
Pâris, I., Petitjean, P., Rollinde, E., et al. 2011, A&A, 530, A50
Perrotta, S., Hamann, F., Zakamska, N. L., et al. 2019, MNRAS, 488, 4126
Pitchford, L. K., Farrah, D., Alatalo, K., et al. 2019, MNRAS, 487, 3130
Popescu, C. C., Hopp, U., Hagen, H. J., & Elsaesser, H. 1996, A&AS, 116, 43
Prevot, M. L., Lequeux, J., Maurice, E., Prevot, L., & Rocca-Volmerange, B. 1984, A&A, 132, 389
Privon, G. C., Ricci, C., Aalto, S., et al. 2020, ApJ, 893, 149
Proga, D., & Kallman, T. R. 2004, ApJ, 616, 688
Proga, D., Stone, J. M., & Kallman, T. R. 2000, ApJ, 543, 686
Quider, A. M., Nestor, D. B., Turnshek, D. A., et al. 2011, AJ, 141, 137
Rafiee, A., Pirkola, P., Hall, P. B., et al. 2016, MNRAS, 459, 2472
Rankine, A. L., Hewett, P. C., Banerji, M., & Richards, G. T. 2020, MNRAS, 492, 4553
Reichard, T. A., Richards, G. T., Hall, P. B., et al. 2003, AJ, 126, 2594
Richards, G. T., Lacy, M., Storrie-Lombardi, L. J., et al. 2006, ApJS, 166, 470
Rogerson, J. A., Hall, P. B., Snedden, S. A., Brotherton, M. S., & Anderson, S. F. 2011, NewA, 16, 128
Runnoe, J. C., Ganguly, R., Brotherton, M. S., & DiPompeo, M. A. 2013, MNRAS, 433, 1778
Sabra, B. M., & Hamann, F. 2005, arXiv:astro-ph/0509421
Scannapieco, E., & Oh, S. P. 2004, ApJ, 608, 62
Schaye, J. 2001, ApJ, 559, 507
Schulze, A., Misawa, T., Zuo, W., & Wu, X.-B. 2018, ApJ, 853, 167
Schulze, A., Schramm, M., Zuo, W., et al. 2017, ApJ, 848, 104
Shang, Z., Wills, B. J., Robinson, E. L., et al. 2003, ApJ, 586, 52
Shi, X.-H., Jiang, P., Wang, H.-Y., et al. 2016, ApJ, 829, 96
Spoon, H. W. W., Farrah, D., Lebouteiller, V., et al. 2013, ApJ, 775, 127
Stalevski, M., Tristram, K. R. W., & Asmus, D. 2019, MNRAS, 484, 3334
Suzuki, N. 2006, ApJS, 163, 110
Thompson, T. A., Fabian, A. C., Quataert, E., & Murray, N. 2015, MNRAS, 449, 147
Tombesi, F., Cappi, M., Reeves, J. N., et al. 2010, A&A, 521, A57
Trammell, G. B., Vanden Berk, D. E., Schneider, D. P., et al. 2007, AJ, 133, 1780
Trump, J. R., Hall, P. B., Reichard, T. A., et al. 2006, ApJS, 165, 1
Urrutia, T., Becker, R. H., White, R. L., et al. 2009, ApJ, 698, 1095
Urrutia, T., Lacy, M., & Becker, R. H. 2008, ApJ, 674, 80
Vayner, A., Zakamska, N. L., Riffel, R. A., et al. 2021, MNRAS, 504, 4445
Veilleux, S., Meléndez, M., Sturm, E., et al. 2013, ApJ, 776, 27
Vestergaard, M., & Wilkes, B. J. 2001, ApJS, 134, 1
Villforth, C., Herbst, H., Hamann, F., et al. 2019, MNRAS, 483, 2441
Violino, G., Coppin, K. E. K., Stevens, J. A., et al. 2016, MNRAS, 457, 1371
Vivek, M., Srianand, R., Petitjean, P., et al. 2012, MNRAS, 423, 2879
Vivek, M., Srianand, R., Petitjean, P., et al. 2014, MNRAS, 440, 799
Voelker, J., Choi, H., Leighly, K., DeFrancesco, C., & Dabbieri, C. 2021, AAS Meeting, 237, 337.10
Voit, G. M., Weymann, R. J., & Korista, K. T. 1993, ApJ, 413, 95
Vollmer, B., Schartmann, M., Burtscher, L., et al. 2018, A&A, 615, A164
Wagner, C., Leighly, K., Macinnis, F., Marrs, A., & Richards, G. T. 2017, AAS Meeting, 229, 250.15
Wampler, E. J., Chugai, N. N., & Petitjean, P. 1995, ApJ, 443, 586
Wang, T., Ferland, G. J., Yang, C., Wang, H., & Zhang, S. 2016, ApJ, 824, 106
West, A. A., Morgan, D. P., Bochanski, J. J., et al. 2011, AJ, 141, 97
Weymann, R. J., Morris, S. L., Foltz, C. B., & Hewett, P. C. 1991, ApJ, 373, 23
White, R. L., Becker, R. H., Gregg, M. D., et al. 2000, ApJS, 126, 133
Yi, W., Brandt, W. N., Hall, P. B., et al. 2019, ApJS, 242, 28
Yip, C. W., Connolly, A. J., Vanden Berk, D. E., et al. 2004, AJ, 128, 2603
Young, M., Elvis, M., & Risaliti, G. 2009, ApJS, 185, 250
Yuan, S., Strauss, M. A., & Zakamska, N. L. 2016, MNRAS, 462, 1603
Zakamska, N. L., Hamann, F., Pâris, I., et al. 2016, MNRAS, 459, 3144
Zhang, N.-X., Brandt, W. N., Ahmed, N. S., et al. 2017, ApJ, 839, 101
Zhang, S., Zhou, H., Wang, T., et al. 2015, ApJ, 803, 58
Zubovas, K. 2018, MNRAS, 473, 3525